

The Pennsylvania State University  
The Graduate School  
Eberly College of Science

THE ANGULAR DISTRIBUTION OF ELECTRON-POSITRON PAIRS  
FROM EXCLUSIVE CHARMONIUM DECAYS  
IN ANTIPROTON-PROTON ANNIHILATIONS

A Thesis in

Physics

by

Robert J. McTaggart II

Submitted in Partial Fulfillment  
of the Requirements  
for the Degree of

Doctor of Philosophy

May 1999

We approve the thesis of Robert J. McTaggart II.

Date of Signature

---

Gerald A. Smith  
Professor of Physics  
Thesis Advisor  
Chair of Committee

---

---

Ben Y. Oh  
Professor of Physics

---

---

Abul Hasan  
Associate Professor of Physics

---

---

Mark Strikman  
Professor of Physics

---

---

Gordon P. Garmire  
Evan Pugh Professor of  
Astronomy and Astrophysics

---

---

Jayanth R. Banavar  
Professor of Physics and Materials Research  
Head of the Department of Physics

---

# Abstract

The angular distributions of the charmonium resonances  $J/\Psi(3097)$  and  $\Psi(3686)$  in their exclusive decay to an electron-positron pair are studied.

Experiment 835 at the Fermi National Accelerator Laboratory produced charmonium resonances by annihilating protons with antiprotons in the Fixed Target Mode of the Antiproton Accumulator: A stochastically cooled antiproton beam collides with a hydrogen gas jet, which forms clusters under the right pressure and low temperature. The charmonium decay products are detected out of a large hadronic background with the help of a segmented lead glass sampling calorimeter, which is sensitive to the high mass electron-positron charmonium decay, and a set of Cerenkov threshold detectors that provide good electron/pion separation. Several factors influence the angular distribution parameter  $\lambda$  taken from the angular distribution, including the energy scale of the resonance, the coupling strength of the charmonium atom, and how quarks and gluons interact in the dissolution of the proton and antiproton. The angular distribution parameter is determined to be  $0.63 \pm 0.18$  (statistical)  $\pm 0.05$  (systematic) at the  $J/\Psi(3097)$ , and  $0.66 \pm 0.27$  (statistical)  $\pm 0.03$  (systematic) at the  $\Psi(3686)$ .

# Table of Contents

List of Figures	vii
List of Tables	x
Acknowledgements	xii
1. Charmonium	1
1.1 History	1
1.2 Spectroscopy	7
1.3 Potential Theory	10
2. Production of Charmonium	18
2.1 History	18
2.2 Production and Storage of Antiprotons	19
2.3 Beam Energy Measurement	22
2.4 Hydrogen Gas Jet	26
3. The e835 Spectrometer	29
3.1 Luminosity Monitor	29
3.2 Inner Detectors	30
3.3 Central Calorimeter	34
3.4 Forward Calorimeter	39

4. Data Acquisition	42
4.1 The Trigger	43
4.2 DART Hardware	45
4.3 DART Software	49
4.4 Dead Time	53
4.5 Operations	54
5. Theory of Angular Distributions	57
5.1 Helicity Formalism	57
5.2 The Angular Distribution Parameter	65
5.3 Comparison of Theoretical Predictions	71
6. Analysis	78
6.1 Electron-positron pair determination	78
6.2 Polar angle from Fibers and CCAL	81
6.3 Thesis Sample Selection	88
6.4 Background to the Thesis Sample	106
6.5 Dependence of the Electron Trigger on the Polar Angle	111
7. Results	114
8. Conclusions	121
Appendix A: Efficiencies of Cuts, $J/\psi$	128

Appendix B: Efficiencies of Cuts, • ’	132
Bibliography	136

# List of Figures

Figure 1.1: Quark -lepton doublets prior to 1974	1
Figure 1.2: Ratio R of $e^+e^-$ annihilation into hadrons from 0 to 40 GeV	2
Figure 1.3: Discovery of the $J/\psi$ at Brookhaven and at SLAC	4
Figure 1.4: OZI-suppressed charmonium decay	5
Figure 1.5: OZI-allowed charmonium decay	6
Figure 1.6: The spectrum of charmonium bound states below the threshold to open charm	8
Figure 2.1: The E835 Antiproton Accumulator	20
Figure 2.2: The E835 Hydrogen Gas Jet	27
Figure 3.1: The Spectrometer for Fermilab Experiment 760	29
Figure 3.2: Side View of the E835 Inner Detectors	31
Figure 3.3: Cross section of the Cerenkov detector	33
Figure 3.4: One wedge of the Central Calorimeter	34
Figure 3.5: One ring of the Central Calorimeter	36
Figure 3.6: Front view of the Forward Calorimeter	39
Figure 3.7: Forward Calorimeter Module	40
Figure 4.1: The CCAL Trigger Logic	43
Figure 4.2: Hardware of the E835 Data Acquisition System	47
Figure 4.3: Active DART software processes for the DAQ	50
Figure 4.4: The filter PRUDE and the logger	51

Figure 5.1: Decay of the $J/\psi$ or $\psi'$ in the helicity formalism	61
Figure 5.2: Lowest order Feynman graph for the strong contribution to the angular distribution parameter	67
Figure 6.1: Data Analysis Flow Chart	78
Figure 6.2: Behavior of the CCAL Clusterizer	84
Figure 6.3: Detection efficiency of the scintillating fiber tracker	87
Figure 6.4: Number of fibers hit as a function of polar lab angle	87
Figure 6.5: $J/\psi$ On-time Cluster Number	92
Figure 6.6: $\psi$ (3686) On-time Cluster Number	93
Figure 6.7: $J/\psi$ Invariant Mass	96
Figure 6.8: $\psi$ (3686) Invariant Mass	97
Figure 6.9: $J/\psi$ Acoplanarity	99
Figure 6.10: $J/\psi$ Akinematics	100
Figure 6.11: $\psi$ (3686) Acoplanarity	101
Figure 6.12: $\psi$ (3686) Akinematics	102
Figure 6.13: $J/\psi$ Total Energy	104
Figure 6.14: $\psi$ (3686) Total Energy	105
Figure 6.15: Invariant mass for Background Runs 1180-1184	108
Figure 6.16: Invariant mass for Background Runs 1283-1289	109
Figure 6.17: Angular Distributions for Background Candidates	110

Figure 7.1: $J/\psi \rightarrow e^+e^-$ Angular Distribution	116
Figure 7.2: $\psi' \rightarrow e^+e^-$ Angular Distribution	117
Figure 8.1: Comparison of thesis value with the theoretical predictions for the angular distribution parameter at the $J/\psi$	123
Figure 8.2: Comparison of thesis value with the theoretical predictions for the angular distribution parameter at the $\psi'$	124
Figure 8.3: Comparison of thesis value with previous experimental data for the angular distribution parameter at the $J/\psi$	125

# List of Tables

Table 5.1 : Theoretical Predictions of the angular distribution parameter and partial width to $p\bar{p}$ at the $J/\psi$	76
Table 5.2 : Theoretical Predictions of the angular distribution parameter and partial width to $p\bar{p}$ at the $\psi'$	77
Table 6.1 : Number of entries in final angular distributions.	88
Table 6.2 : Summary of analysis cuts.	89
Table 6.3 : Background estimate from off-resonance data.	111
Table 6.4 : Definitions for the E835 $e^+e^-$ trigger	113
Table 7.1 : Final Fit Parameters	115
Table 7.2 : Angular Distribution Parameters	115
Table 7.3 : Sachs form factor ratio and helicity one production derived from the angular distribution parameter	119
Table 7.4 : Previous experimental results for the angular distribution parameter	120
Table A.1: Efficiency of one cut on the $J/\psi$ n-tuple	128
Table A.2: Efficiency of two cuts on the $J/\psi$ n-tuple	129
Table A.3: Efficiency of three cuts on the $J/\psi$ n-tuple	130

Table A.4: Efficiency of four cuts on the $J/\psi$ n-tuple	131
Table B.1: Efficiency of one cut on the $\psi'$ n-tuple	132
Table B.2: Efficiency of two cuts on the $\psi'$ n-tuple	133
Table B.3: Efficiency of three cuts on the $\psi'$ n-tuple	134
Table B.4: Efficiency of four cuts on the $\psi'$ n-tuple	135

# Acknowledgements

I would like to take this occasion to thank my thesis advisor Dr. Gerald A. Smith and Raymond Lewis for their guidance and criticism during the production of this document. Furthermore, I would like to express my gratitude to the many members of the E835 collaboration at Fermilab, both past and present, for their friendship and assistance. And finally I would like express my sincere appreciation to all of my friends at Fermilab and Penn State.

This thesis is dedicated to my parents, Bob and Bonny McTaggart, and my brother Dan, without whose love and support this thesis would not have been possible.

# 1. Charmonium

## 1.1. History

Prior to 1974, the existence of a fourth quark was a matter of conjecture based on theoretical debate and circumstantial evidence. Three different quarks were known to exist (up, down, strange) along with four leptons (electron, muon, e-neutrino,  $\mu$ -neutrino). Based upon symmetry, an additional quark was required in order to complete the quark-lepton doublets shown in Figure 1.1.

$$\begin{array}{cc} \left( \begin{array}{c} e \\ \nu_e \end{array} \right) & \left( \begin{array}{c} \nu_\mu \\ \mu \end{array} \right) & \begin{array}{l} -1 \\ 0 \end{array} \\ \\ \left( \begin{array}{c} u \\ d \end{array} \right) & \left( \begin{array}{c} s \\ c \end{array} \right) & \begin{array}{l} + 2/3 \\ - 1/3 \end{array} \end{array}$$

Figure 1.1 : Quark-lepton doublets prior to 1974.

The ratio of electron-positron annihilation rates into hadrons versus that for muons depends to first order on (a) the number of colors each quark has, and (b) the number of quark flavors. Note the increase in Figure 1.2 with the addition of each quark. This ratio was shown to increase past a center of mass energy around 3 GeV, and an additional quark flavor with a +2/3 charge could help account for the difference.<sup>1</sup>

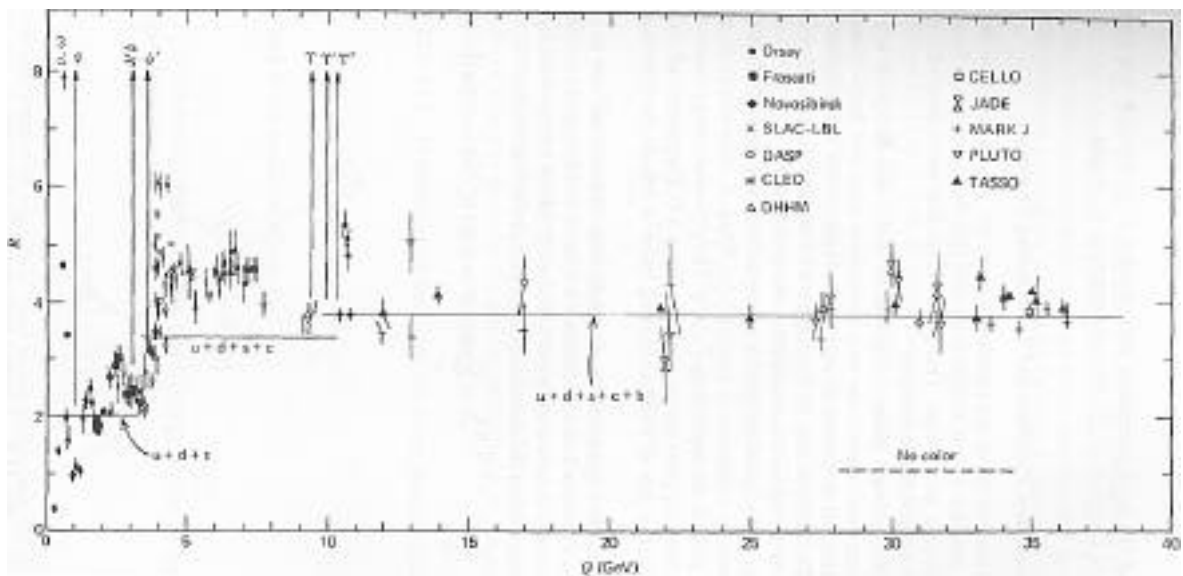


Figure 1.2: Ratio R of  $e^+e^-$  annihilation into hadrons from 0 to 40 GeV.<sup>2</sup>

Charm was shown in 1970 under the GIM mechanism to explain the absence of strangeness-changing neutral currents in weak interactions. The suppression of such decays is explained by the different masses of the up and charm quarks.<sup>3</sup> In 1974, Appelquist and Politzer predicted that charmonium would form a set of bound states much like those seen in positronium.<sup>4</sup>

Hence, there were experimental and theoretical indications of the existence of a charmed quark. However, the existence of a fourth quark would mean that there should be more hadronic states. Evidently, if there were a fourth quark, it was heavy enough for these other hadronic states to lie at energies not exceeded by any experiment at that time.

In November, 1974, two experiments independently discovered a resonance with a strikingly narrow total width at around a center-of-mass energy of 3.1 GeV. Brookhaven National Laboratory (BNL) saw this feature in the invariant  $e^+e^-$  mass plot produced by collisions of a proton beam on a Beryllium target. They called this new resonance ' $J$ '.<sup>5</sup> The Stanford Linear Accelerator Center (SLAC) saw this resonance in a plot of cross-section vs. energy for multi-hadron final states resulting from  $e^+e^-$  annihilations.<sup>6</sup> SLAC called this resonance  $\psi$ , and today it is called the  $J/\psi$ .

The radial excitation of the  $J/\psi$ , the  $\psi'$ , was soon discovered afterwards.<sup>7</sup> However, these two resonances could not be confidently attributed to the bound state of a charm-anticharm quark pair until the so-called "charmed" mesons (i.e. mesons with a constituent charm quark) were found and the unique behavior of its decays were verified by experiment.<sup>2,8</sup>

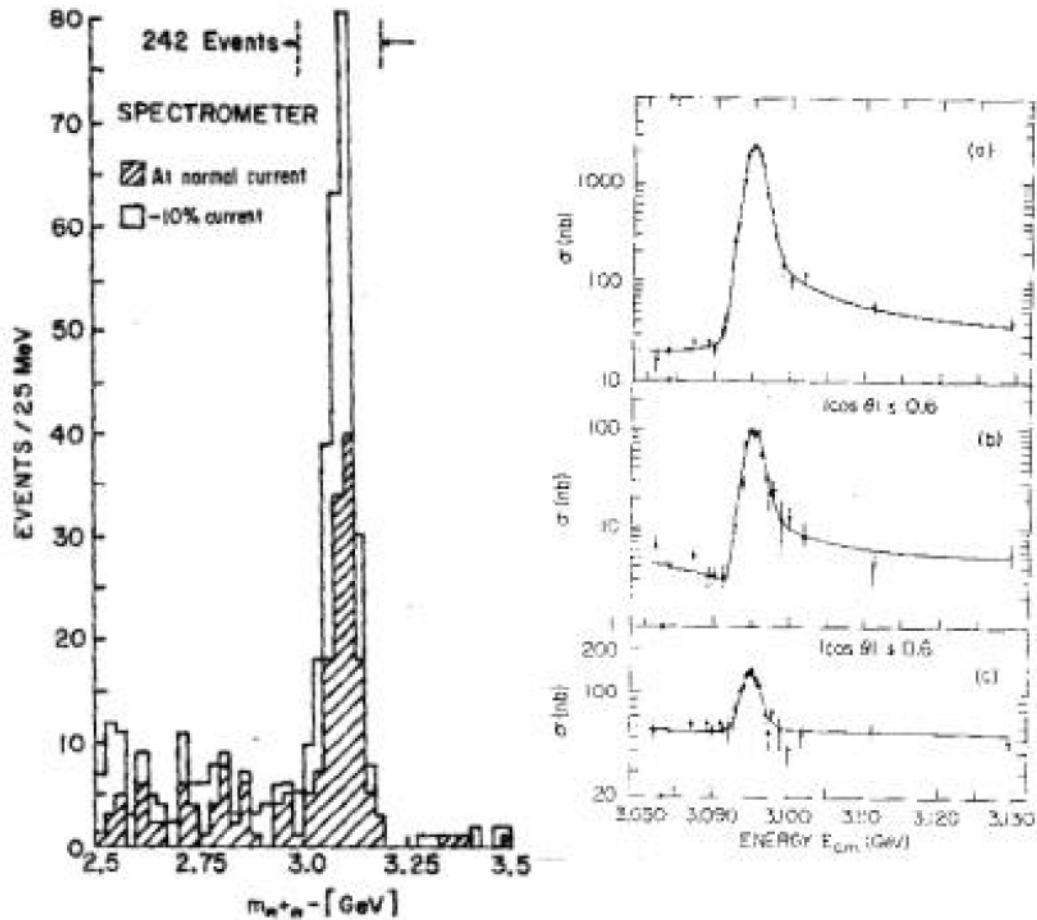


Figure 1.3: Discovery of the  $J/\psi$  at Brookhaven (left)<sup>5</sup>, and at SLAC (right).<sup>6</sup>

One may rightfully ask how one can assign these two new resonances to a family called charmonium. The first clue is the extremely narrow widths of these two resonances. This may be explained by the OZI-Rule (Okubo-Zweig-lizuka), which has been applied to the  $\psi$  meson. Although the Q-value of the decay (the Q-value is the maximum kinetic energy released in the decay of the resonance to the lowest mass state containing the constituent quarks of the parent resonance) into two K mesons is quite small and the Q-value of the decay into  $3\pi$  is much larger, the decay of the  $\psi$  meson into kaons dominates.<sup>1</sup>

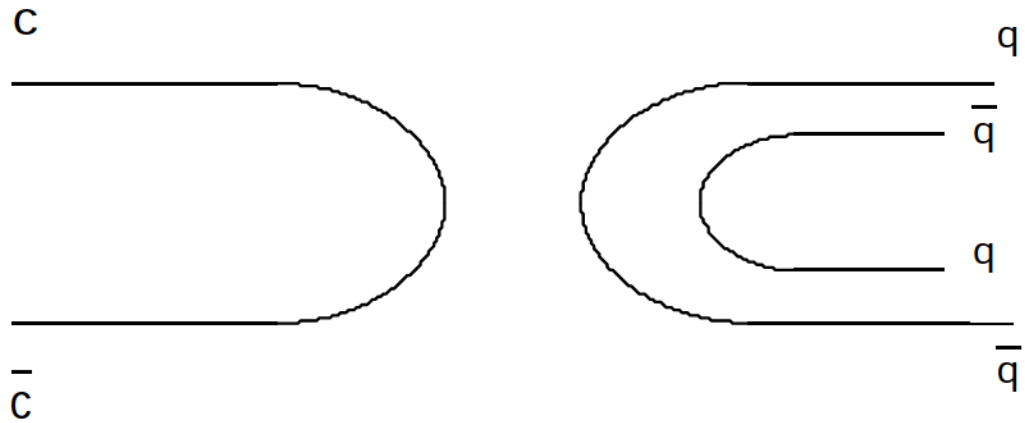


Figure 1.4: OZI-suppressed charmonium decay.

The OZI rule states that the disconnected quark diagrams of Figure 1.4 (where one or more quark lines are not continuous from the initial to the final state) are suppressed relative to the connected quark diagrams of Figure 1.5. In the case of the  $\psi$  meson, the decay to K mesons is connected and the decay to 3 pions, while open to more phase space, is disconnected (no strange quarks appear in the final state). While the  $\psi$  meson sits just above the threshold to decay into the two lowest-mass strange mesons, several charmonium resonances are below the threshold for the decay into the two lowest charmed mesons. Decays with connected diagrams are thus not kinematically allowed for charmonium resonances with masses less than twice the mass of the smallest charmed meson,  $D(c\bar{u})$ . Widths are smaller beneath this threshold because decays are forced to proceed through the suppressed channels.

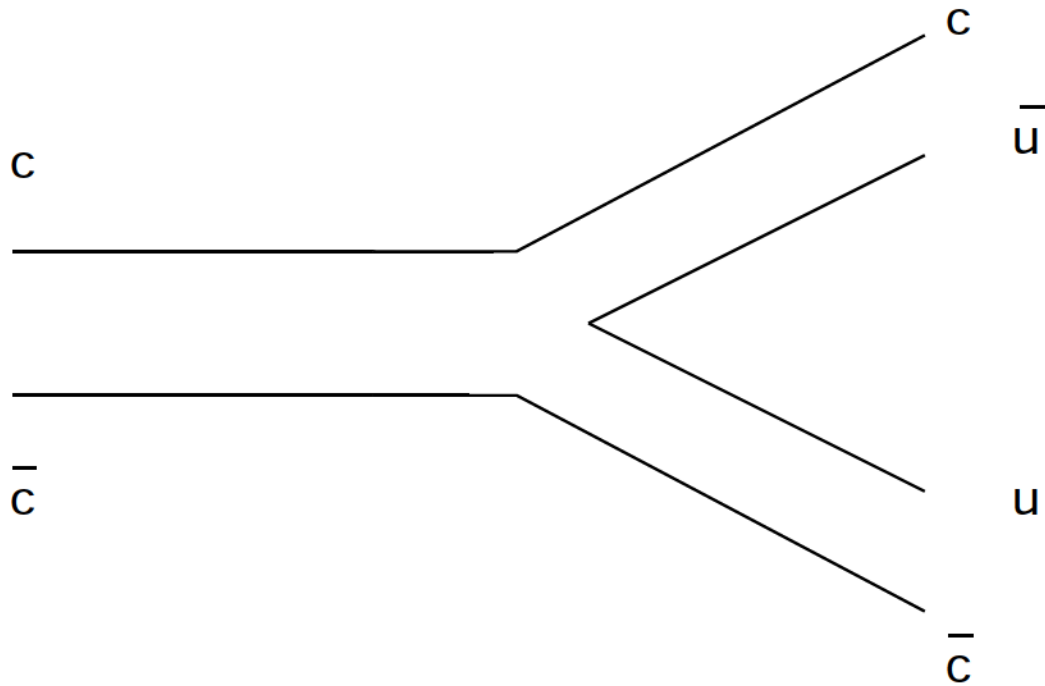


Figure 1.5: OZI-allowed charmonium decay.

The D-meson was discovered at SLAC in 1976 with a mass of 1863 MeV.<sup>9</sup> With the exception of D-wave states that cannot decay into D-mesons due to parity, all charmonium states above twice this mass have broad widths. Since charm is conserved in strong and electromagnetic decays, D-mesons and their charmed cousins must decay via weak interactions, which were subsequently found at SLAC and DESY (Deutsches Elektronen-Synchrotron). Observation of the excited  $D^*$  and F mesons, the intermediate P-level states, and the increase in the ratio R mentioned previously near the region of 3.1 GeV all lead one to believe that the  $\psi$  family is built from a charmed quark-antiquark pair.<sup>9</sup>

## 1.2. Spectroscopy

States in the charmonium spectrum (see Figure 1.6) are labelled either by quantum numbers  $J^{PC}$ , where  $\mathbf{J}$  is the total spin of the system ( $\mathbf{J} = \mathbf{L} + \mathbf{S}$ ), or by the notation  $n^{2S+1}L_J$ , where  $n$  is the radial quantum number. For any fermion-antifermion system, the parity quantum number is

$$P = (-1)^{L+1}, \quad (1.1)$$

and the charge-conjugation parity is

$$C = (-1)^{L+S}. \quad (1.2)$$

The quantum numbers for the  $J/\psi$  (3097),<sup>10</sup>  $\psi'$  (3686),<sup>11</sup> and the  $\psi(3770)$ <sup>12</sup> have been found to be the same as those of the photon,  $1^-$ . Thus these states are readily accessible to production via  $e^+e^-$  annihilation, which produces a virtual photon with the same quantum numbers.

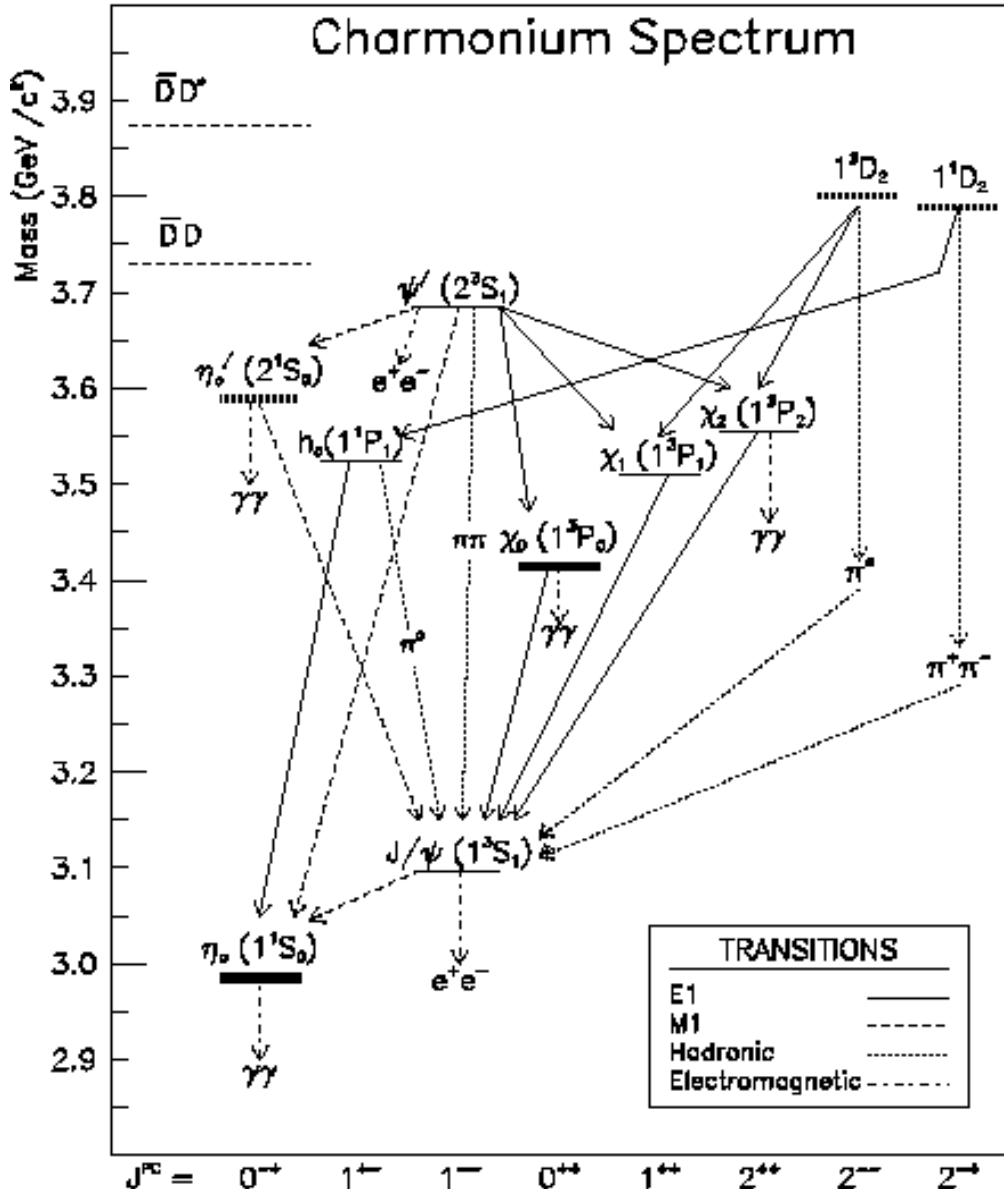


Figure 1.6: The spectrum of charmonium bound states below the threshold to open charm.<sup>13</sup>

The dominating characteristic of the charmonium spectrum is the apparent division between the low-lying states with total widths on the order of 100 keV and higher excitations that have widths on the order of 100 MeV. The

principal reason for this effect is the heavy mass of the charmed quark, which is approximately 1.5 GeV. States with center-of-mass energies less than twice the mass of the lightest charmed meson obey the previously mentioned OZI-Rule: The decay into hadrons with lighter quarks is suppressed while the decay into charmed mesons is not allowed.

The other impact of the mass of the charmed quark is that the quantum mechanics of the hydrogen atom can be applied to the charmonium system. One can roughly evaluate the worthiness of the approach by computing the average kinetic energy of charmonium via the virial theorem. Given that a linear term in the potential dominates at the mean radius of the charmonium atom and the expectation value for the kinetic energy,

$$\langle T \rangle = \frac{1}{2} \langle \vec{r} \cdot \vec{\nabla} V(\vec{r}) \rangle, \quad (1.3)$$

where the binding energy of the system is  $E_b = 3 \langle T \rangle$ . Non-relativistically the kinetic energy of two charmed quarks is expressed as

$$\langle T \rangle = 2 \left( \frac{m_c \langle v^2 \rangle}{2} \right). \quad (1.4)$$

As a result, one expects for the charmed quark the square of the velocity to be

$$\langle v^2 \rangle = \frac{E_b}{3m_c}. \quad (1.5)$$

Assuming for the charmonium system that the binding energy is the difference in masses between the  $J/\psi$  (near the lowest possible bound state) and the  $\psi'$  (close to the threshold to open charm), and the mass of the charm quark is approximately 1.5 GeV, one obtains an estimate for this squared velocity of  $0.15 c^2$ . One sees that although relativistic effects may be important, they do not dominate the charmonium system. In stark contrast, the masses of the lighter quarks (from under 10 MeV to a couple hundred MeV) make any non-relativistic treatment unreliable. Spectroscopy of these lower mass states is also encumbered by the sheer number of the light-quark states and their overlapping widths.

### 1.3. Potential Theory

Since the mass of the charmed quark is so heavy, we attempt to apply a non-relativistic Schrödinger's Equation to the charmonium system with a QCD-inspired potential. Although many different potentials exist, the one most often referred to and the simplest one is the Cornell potential, which addresses the two main concepts in QCD: asymptotic freedom and quark confinement. It consists of a Coulomb-like term representing one-gluon exchange at small distances and a linear term, most likely due to multi-gluon exchanges, that will force quarks to be confined in hadrons and mesons:

$$V(r) = -\frac{4}{3} \frac{\alpha_s(r)}{r} + kr. \quad (1.6)$$

Asymptotic freedom does not exist in QED: The charge of an electron is determined by its long distance behavior. Vacuum fluctuations of electron-positron pairs tend to screen the bare charge, so that the closer you get to the electron, the greater the charge. Whereas photons (the carriers of the electromagnetic interaction) do not carry a charge (and thus do not interact with each other), gluons (the carriers of the strong interaction) carry a *color* charge. As the distance scale becomes larger however,  $\alpha_s$  increases as well as the contributions of higher order terms in a perturbative approach.

Hence there is no corresponding long-distance QCD limit for the color charge. In QCD the color charge leads to antiscreening: The closer you get to the particle in question, the less intense the effective force becomes, and the more the particle acts like it were free. The constant  $\alpha_s$  and its decrease with increasing energy may be parameterized in terms of its Fourier transform<sup>14</sup>

$$\alpha_s(Q^2) = \frac{12 \pi}{(33 - 2n_f) \ln \left[ \frac{Q^2}{\Lambda^2} \right]}, \quad (1.7)$$

where  $n_f$  is the number of flavors with mass below  $Q$  and  $\Lambda$  is a characteristic

scale of about 200 MeV.

Applying such potentials depends in part on the strength of the strong coupling constant  $\alpha_s$ . The corresponding coupling constant for QED (Quantum Electrodynamics) is much smaller,  $1/137$ , than the average value of  $\alpha_s$  in the charmonium system (typically calculated between 0.2 and 0.3). If  $\alpha_s$  is too large, then perturbative techniques, such as describing processes via first-order Feynman graphs, are no longer valid.

The behavior of  $\alpha_s$  at large distances is related to the reason why only colorless combinations of subatomic particles occur in nature and quarks are confined to mesons or hadrons. Before a particle with a single color can escape, enough energy exists to manifest new colorless combinations of particles out of the vacuum due to the considerable value of  $\alpha_s$  in the QCD potential.

Due in part to the complexities brought about by confinement, a simple non-relativistic potential by itself may not be satisfactory to model the charmonium bound states. Spin dependence of the QCD potential may be accomplished by dividing the above potential into vector and scalar parts, and then using these terms to build a Hamiltonian with spin-spin, tensor, and spin-

orbit contributions. The necessity of including spin dependence can be demonstrated by observing the splitting of the S and P state, which would not occur without the relativistic effects inherent in the concept of spin.

In principle, one takes the Bethe-Salpeter equation for a relativistic bound state system and expands everything up to order  $(v^2/c^2)$ . A non-relativistic reduction of this equation yields the generalized Breit-Fermi Hamiltonian<sup>15</sup>:

$$H = m_1 + m_2 + \frac{\vec{p}^2}{2\mu} - \frac{1}{8} \left( \frac{1}{m_1^3} + \frac{1}{m_2^3} \right) \vec{p}^4 + V(r) + H_{SI} + H_{LS} + H_{SS} + H_T, \quad (1.8)$$

where the potential is a sum of a vector and a scalar contribution,

$$V(r) = V_V(r) + V_S(r). \quad (1.9)$$

The spin-orbit ( $H_{LS}$ ), spin-spin ( $H_{SS}$ ), and tensor ( $H_T$ ) terms may be written as:

$$H_{LS} = \frac{1}{2m^2 r} \left( 3 \frac{d}{dr} V_V(r) - \frac{d}{dr} V_S(r) \right) \vec{L} \cdot \vec{S}; \quad (1.10)$$

$$H_{SS} = \frac{2}{3m^2} \vec{S}_1 \cdot \vec{S}_2 \cdot \nabla_V(r); \text{ and} \quad (1.11)$$

$$H_T = \frac{1}{12m^2} \left( \frac{1}{r} \frac{d}{dr} V_V(r) - \frac{d^2}{dr^2} V_V(r) \right) S_{12}, \quad (1.12)$$

where

$$S_{12} = 12 \left( \frac{(\vec{S}_1 \cdot \vec{r})(\vec{S}_2 \cdot \vec{r})}{r^2} - \frac{1}{3} \vec{S}_1 \cdot \vec{S}_2 \right). \quad (1.13)$$

The existence of these spin-dependent potentials has a direct impact on the spacing in the charmonium spectrum. Specifically the hyperfine interaction,  $H_{SS}$ , introduces a splitting between the singlet ( $^1S_0$ ) and triplet ( $^3S_1$ ) S-wave resonances (respectively the  $\psi_c$  and the  $J/\psi$  for example). The spin-orbit and tensor interactions also lead to different energy levels for the triplet P-wave states ( $^3P_J$  or  $\psi_J$ ,  $J=0, 1, 2$ ).

Another concept that is sometimes incorporated into the study of the charmonium spectrum is quantum mechanical mixing, in which every charmonium state is a linear combination of all other charmonium states above and below threshold with the same set of quantum numbers  $J^{PC}$  via a “coupled channel” formalism.<sup>16</sup> The bound charmonium states are not the pure states given by the potential models, but usually the amount of mixing is negligible or small.

In fact, the  $\psi(3770)$  (above threshold) and the  $\psi(3686)$  (below threshold) are probably quantum mechanically mixed.<sup>17</sup> This explains why the decay

width of the  $\rho(3770)$  into  $e^+e^-$  is too large for a pure D-wave, and the decay width of the  $\rho(3686)$  is slightly too small for a pure S-wave. The amount of S-D wave mixing in each resonance is defined by a mixing angle<sup>18</sup>

$$|\rho(3686)\rangle = |2^3S_1\rangle \cos\theta + |1^3D_1\rangle \sin\theta \quad (1.14)$$

and 
$$|\rho(3770)\rangle = -|2^3S_1\rangle \sin\theta + |1^3D_1\rangle \cos\theta, \quad (1.15)$$

brought about by a tensor interaction<sup>19</sup>

$$\sin\theta \approx 2\sqrt{2} \frac{\langle 2^3S_1 | V_{\text{tensor}} | 1^3D_1 \rangle}{E_{1^3D_1} - E_{2^3S_1}}. \quad (1.16)$$

Expectations for this mixing angle range from anywhere between 0 to 30 degrees,<sup>20,21</sup> but it is most likely small enough to regard the  $\rho'$  as a pure S-wave resonance.

Of course the true test of all the different potentials in a Schrödinger equation, or any other formalism describing this system, is their ability to replicate and/or predict the behavior of the bound states as found by experiment. This behavior includes such things as the mass of the resonance, its total width, branching fractions, quantum numbers, energy splittings in the system, and the angular distribution of its decay products.

Charmonium serves as an important testing ground for many different aspects of QCD theory and experiment. The angular distributions of  $J/\psi \rightarrow e^+e^-$  and  $\psi' \rightarrow e^+e^-$  are proportional to  $1 + \alpha \cos^2(\theta)$ , where  $\theta$  is the center-of-mass polar angle and  $\alpha$  is the angular distribution parameter. The parameter  $\alpha$  is sensitive to issues such as the wavefunction of the charmonium atom (and therefore the QCD potential), how charmonium couples to  $p\bar{p}$ , and the structure of the proton at charmonium energies.

Experimentally, the charmonium family has a rich history at several  $e^+e^-$  colliders across the globe such as the European Laboratory for Particle Physics (CERN), the Stanford Linear Accelerator (SLAC), the Deutsches Elektronen-Synchrotron (DESY), and the Beijing Electron Positron Collider (BEPC). Recently charmonium experiments have been performed by colliding protons with antiprotons instead of electrons with positrons, first at CERN and then at Fermilab. In the future, heavier bound state systems such as bottomonium and toponium may one day be created by colliding protons and antiprotons based upon the experience gained by examining charmonium.

In summary, the analysis of angular distributions probe different aspects of the QCD potential, and since the  $J/\psi$  (3097) and  $\psi'$  (3686) may be produced directly by either  $e^+e^-$  annihilation or  $p\bar{p}$  annihilation, the study of these

resonances in particular serve as an important link in the comparison between the two methods. This thesis is a study of the angular distributions in the exclusive decays of  $J/\psi$  (3097) and  $\psi'$  (3686) into  $e^+e^-$  via the proton-antiproton annihilation method.

## 2. Production of Charmonium

### 2.1. History

For the first decade after the discovery of charmonium, it was produced solely by  $e^+e^-$  annihilation. Although the masses resulting from such an experiment are very precise, the widths of the resonances are not. This is a result of the large energy spread in the electron beams and the radiative corrections that must be made. Furthermore, only states with quantum numbers  $J^{PC}=1^-$  can be produced directly in large quantities, since these are the quantum numbers of the virtual photon from the  $e^+e^-$  annihilation.<sup>22</sup>

Resonances without these quantum numbers do not couple to  $e^+e^-$  to first order, and must be studied in the decay from the  $1^-$  states. The ability to see charmonium states at  $e^+e^-$  colliders depends greatly on the resolution of the detector in the experiment and the reconstruction of the final state.<sup>23</sup>

Due to the pioneering efforts of experiment R704 at the CERN Intersecting Storage Rings,<sup>24</sup> it became possible to study charmonium via  $p\bar{p}$  annihilation. R704 implemented a two-arm non-magnetic spectrometer, consisting of an upstream section for tracking charged particles followed by a segmented electromagnetic calorimeter, to optimize the separation between neutral  $\pi^0$ 's and coalesced  $\pi^0$ 's and between charged  $e^-$ 's and  $\mu^-$ 's.<sup>25</sup> Despite the

presence of a larger hadronic background, charmonium's characteristic decays into a high mass  $e^+e^-$  pair allowed detection of these states. Stochastic cooling of an antiproton beam focused onto a hydrogen gas target and precise control of the energy of this beam in an antiproton storage ring permitted the measurement of masses and widths for these narrow resonances to great accuracy. Furthermore, one was no longer limited to studying only the  $1^-$  channel: The full spectrum of charmonium could now be produced directly.

Experiment E760 at Fermilab improved the techniques of a  $p\bar{p}$  annihilation experiment during the 1990-1991 Fixed Target Run. Among its most notable achievements are the discovery of the singlet P-wave<sup>26</sup> ( $^1P_1$ ), examination of the triplet P-wave states ( $\chi$ ), and improvements on the mass and width of the  $\chi_c(2980)$ . E835's goals are to find the missing  $\chi_c'$ , the radial excitation to the  $\chi_c$ , and to complete the spectrum below the threshold to open charm.<sup>27</sup>

## 2.2. Production and Storage of Antiprotons

The Fermilab Antiproton Accumulator (Figure 2.1) was designed to accumulate and cool antiprotons for use of the Tevatron colliding beam program. Protons with an energy of 120 GeV from the main ring collide with a

tungsten target, and the resulting negatively charged particles are collected with a 15 cm X 1cm lithium lens.

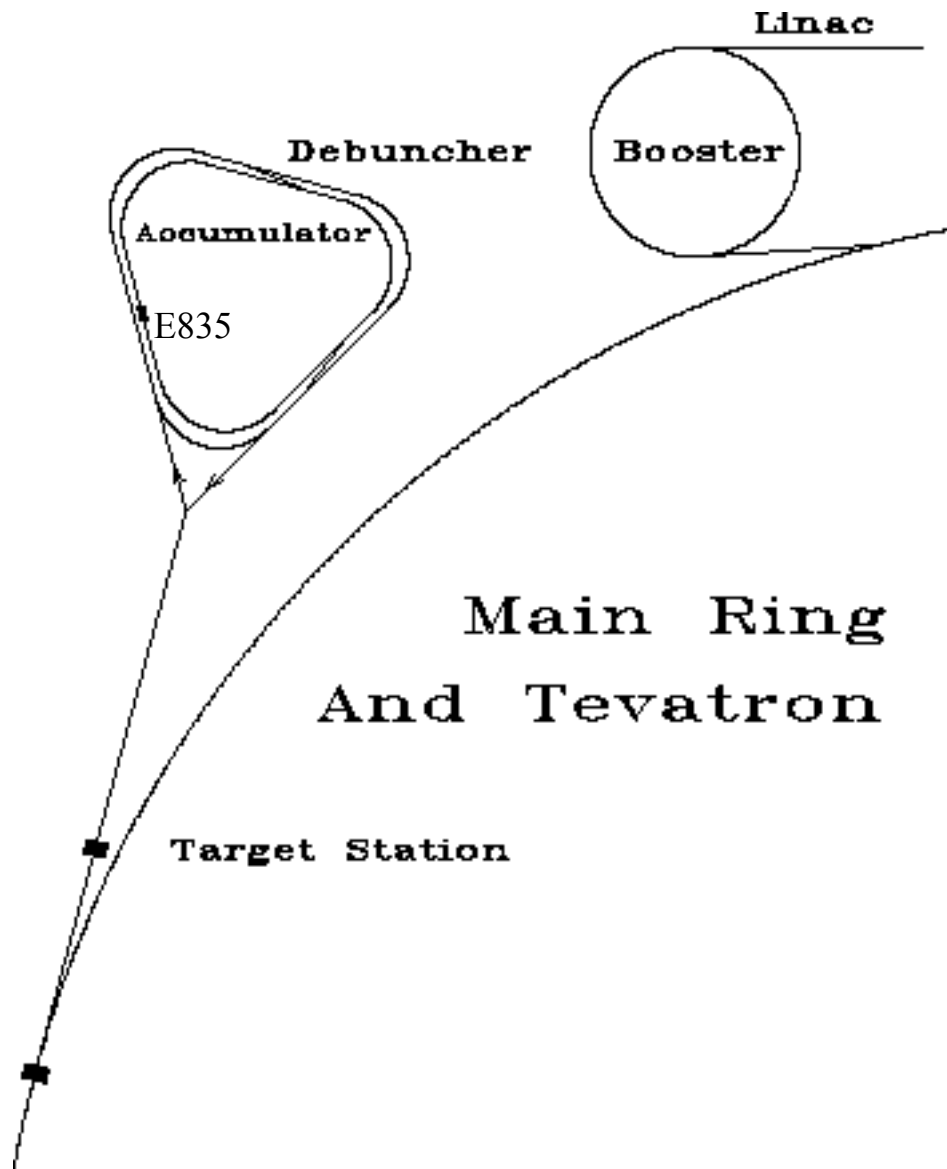


Figure 2.1 : The E835 Antiproton Accumulator.<sup>28</sup>

A debuncher ring then accepts this particle bunch with a momentum of 8.9 GeV/c and stochastically cools the antiprotons, or debunches the antiprotons, into a beam. Stochastic cooling is a process of moving antiprotons

with a kicker magnet away from an unintended orbit to keep the beam transversely small and to keep the momentum spread small. The momentum spread  $\Delta p/p$  drops from about 4 % to 0.2 % at this stage. During this transition any pions or muons have time to decay, and any electrons in the beam are lost due to synchrotron radiation losses.<sup>29,30</sup>

Next, the antiproton beam travels to the Accumulator, where it is stochastically cooled again to a spread of  $\Delta p/p$  of  $2 \times 10^{-4}$  by a series of dipole and quadrupole magnets, and then decelerated to the desired momentum. Stochastic cooling is the primary reason why a  $p\bar{p}$  annihilation experiment can be done. It counteracts the growth of beam emittance due to the many traversals through the hydrogen gas jet target and interactions with residual gas in the accumulator ring. As a result, the beam energy spread can be narrowed to about 0.5 MeV.

When the Accumulator is in the Fixed Target mode, antiprotons are collected until the beam current is anywhere from 50 to 100 mA. The beam is then decelerated until the center of mass energy of the antiproton-proton system reaches the mass of the desired resonance. The antiproton stack size decreases as it interacts with the hydrogen gas jet target. The energy of the beam is decelerated from above the desired value in small steps in order to scan the mass and width of the resonance. Even though the width of the

resonance may be less than the width of the antiproton beam (~500 keV for the beam and ~100 keV for the  $J/\psi$ ), the total width for the resonance can be extracted if the ratio of the peak cross-section to the area under the curve is determined and the width of the beam is known.<sup>22</sup>

### 2.3. Beam Energy Measurement

The success of producing charmonium in  $p\bar{p}$  annihilations depends in large part on the precise determination of the average beam energy and its width. We describe here the procedure to determine these quantities.<sup>22,31</sup>

The beam velocity is given by

$$c\beta = fL, \quad (2.1)$$

where  $f$  is the average revolution frequency of the antiprotons, and  $L$  is the orbit length. Usually  $L$  is defined with respect to some reference orbit length:

$$L = L_0 + \Delta L. \quad (2.2)$$

From equation (2.1) we can derive the following relation:

$$\frac{df}{f} = \frac{d\gamma}{\gamma} - \frac{dL}{L} \quad (2.3)$$

The fractional momentum spread is defined via

$$\frac{d\gamma}{\gamma} = \frac{1}{\gamma^2} \frac{dp}{p} \quad (2.4)$$

Furthermore, a transition gamma factor  $\gamma_t$  is given by

$$\frac{dL}{L} = \frac{1}{\gamma_t^2} \frac{dp}{p} \quad (2.5)$$

Combining equations (2.3) , (2.4) , and (2.5) , the relation between the fractional momentum spread and the fractional frequency spread becomes:

$$\frac{dp}{p} = \frac{1}{\gamma} \frac{df}{f} , \quad (2.6)$$

with the slip factor  $\eta$  defined as:

$$\eta = \frac{1}{\gamma^2} - \frac{1}{\gamma_t^2} \quad (2.7)$$

The transition gamma factor  $\gamma_t$  corresponds to the beam transition energy at which the slip factor  $\eta$  is zero and is completely determined by the nature of the accumulator lattice. Since antiprotons are charged particles, they interact with the other antiprotons in the beam and with the external magnetic fields that bend their path, resulting in both longitudinal oscillations and oscillations transverse to the beam. For beam energies above the transition energy ( $\eta < 0$ ) a higher-energy particle takes a longer time to complete one orbit than a lower energy particle. For beam energies below this threshold ( $\eta > 0$ ) a lower energy particle takes longer to complete one orbit.

Once  $\eta$  is known, the central frequency of the beam is found by analyzing the power spectrum within a given longitudinal Schottky noise band,

$$P(f) \propto e^2 f_{ave}^2 \frac{dN}{df} \eta f . \quad (2.8)$$

The signal is detected by a coaxial quarter wavelength resonant pickup whose bandwidth is much greater than the beam frequency width, 79.323 MHz.

The energy of the beam can then be found from

$$E = \frac{m_p}{\sqrt{1 - (fL)^2}} \quad (2.9)$$

The error on the energy measurement is thus

$$\frac{\delta E}{E} = \delta \left( \frac{\delta L}{L} + \frac{\delta f}{f} \right) \quad (2.10)$$

Because survey measurements of the central orbit are not accurate enough, the known value of the electron mass is used to calculate the reference orbit length and its error. With the center of mass energy

$$s = 2 m_p^2 + 2 m_p E \quad (2.11)$$

and its respective error

$$\delta \sqrt{s} = \frac{m_p}{\sqrt{s}} \delta E \quad (2.12)$$

expressed in terms of the beam energy, and noting that the fractional frequency error is very small, i.e.  $\delta f/f \sim 10^{-7}$ , the fractional error in the orbit length is:

$$\frac{\Delta L}{L} = \frac{\sqrt{s}}{2m_p^2} \Delta \sqrt{s} \quad (2.13)$$

Using the best available measurement for the  $\Delta \sqrt{s}$  mass,<sup>32</sup>  $3686.00 \pm 0.10$  MeV, one attains a reference orbit length of  $474.0457 \text{ m} \pm 0.67$  mm. However, the quoted error of 0.67 mm is not the only error involved in the determination of the beam energy, since the beam cannot precisely be kept on the reference orbit at all energies. Normally the true orbit deviates from the reference orbit by  $\pm 2$  mm, as measured by 48 BPM's (Beam Position Monitors) distributed throughout the Accumulator. Furthermore, there was a random error in measuring the orbit length of  $\pm 1$ mm. The final mass errors for the  $J/\psi$  and the  $\psi'$  were found to be  $0.05 \text{ MeV}/c^2$  and  $0.15 \text{ MeV}/c^2$  respectively in E760.<sup>31</sup>

## 2.4. Hydrogen Gas Jet

During the 1990-91 Fixed Target Run at Fermilab, E760 utilized a hydrogen gas jet (Figure 2.2) cooled down to 80 K with liquid nitrogen to form the target for the beam of antiprotons.<sup>33</sup> At low temperatures and high pressures, hydrogen gas may form clusters of large numbers of hydrogen molecules in an expansion process from a nozzle. Hence instead of trying to hit a single hydrogen molecule, the antiproton beam has a much larger target, and the probability of an interaction thus increases. This jet has been upgraded to

increase the interaction rate with the antiproton beam for E835, whose intensity has also been increased. There are primarily three reasons why the upgrade on the gas jet was needed.

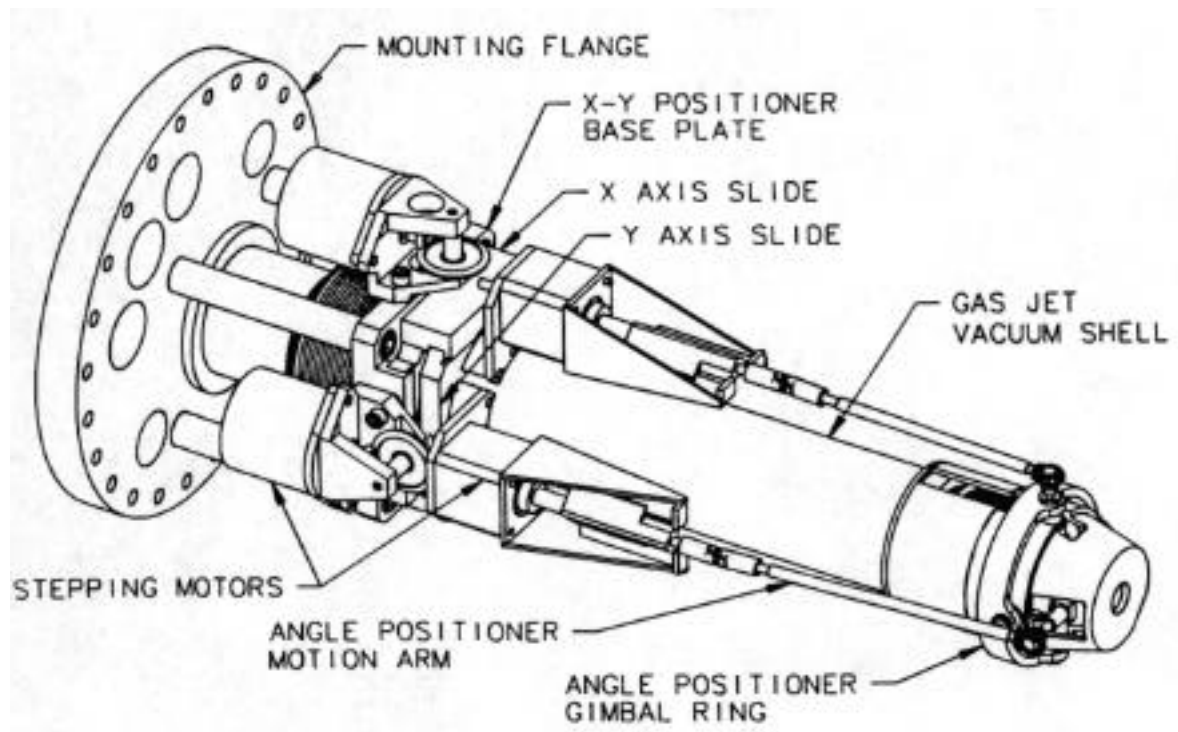


Figure 2.2 : The E835 Hydrogen Gas Jet.<sup>33</sup>

First, larger clusters yield a higher interaction rate with the antiproton beam. The temperature of the hydrogen gas jet has been decreased from 80K to 27K to enhance the clustering of the hydrogen gas, which happens as the gas expands from the nozzle, to at least  $10^4$  atoms per cluster. During testing it was shown that the cryocooler was capable of cooling the jet nozzle to at least 10K, and the density of the gas jet could be as much as 5 times as large as that in E760.

Second, less background gas escaping into the ring improves stochastic cooling and limits unwanted secondary interactions. The pumping speed for the vacuum chamber in which the gas jet sits has been improved. The chamber pressure can be maintained below 1 Pa, and this reduces the interaction of the background gas with the jet stream.

Third, adjusting the position of the jet nozzle can optimize the interaction rate with the antiproton beam. The nozzle may now be moved in the plane perpendicular to the gas stream produced by the nozzle, and the angular direction of the nozzle may be altered as well.

The end result is that an interaction rate of approximately 5 MHz yields a beam lifetime of about 30 hours for a 100 mA antiproton stack.<sup>33</sup>

### 3. The E835 Spectrometer

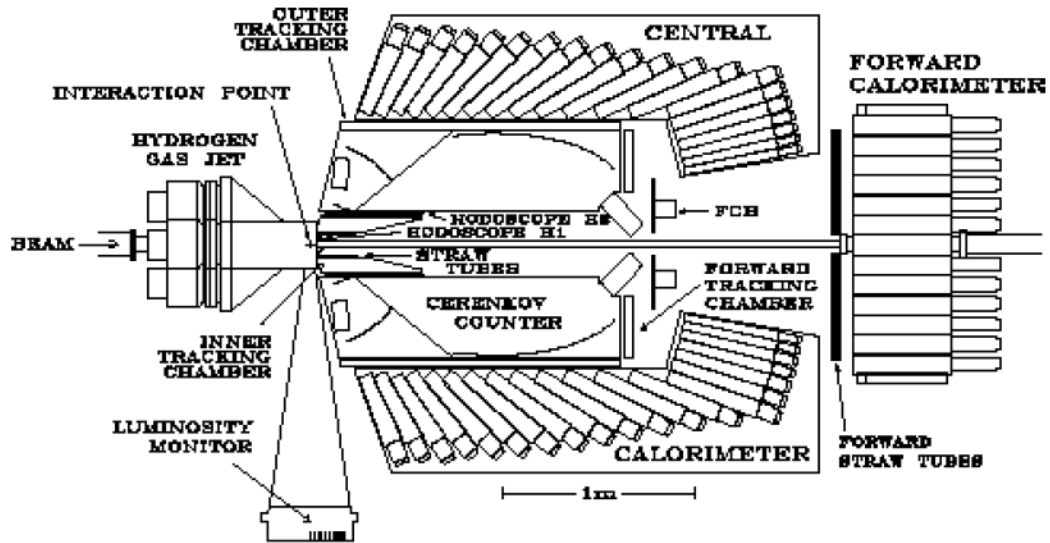


Figure 3.1 : The Spectrometer for Fermilab Experiment 760.<sup>34</sup>

#### 3.1. Luminosity monitor

The luminosity monitor,<sup>35</sup> located in the bottom left corner of Figure 3.1, is a set of solid state detectors that is located directly below the beam pipe. Its purpose is to measure the  $p\bar{p}$  differential cross section near 90 degrees. The  $p\bar{p}$  differential cross section is a sum of nuclear, elastic Coulomb scattering, and interference contributions:

$$\frac{d\sigma}{dt} = \frac{4\pi\alpha^2}{t^2} (\hbar c)^2 G^4(t); \quad (3.1)$$

$$\frac{d\sigma_N}{dt} = \frac{\sigma_T^2 (1 + \sigma^2) e^{-b|t|}}{16\sigma (\hbar c)^2}; \quad (3.2)$$

$$(3.3)$$

and

$$\frac{d\sigma_i}{dt} = \frac{\sigma_T \sigma_T}{|t|} G^2(t) e^{-b|t|} (\sigma \cos(\sigma) + \sin(\sigma)).$$

Knowing the acceptance of the fixed and movable solid-state detectors one can normalize the number of recoiled protons with a certain kinetic energy of the  $p \bar{p}$  differential cross section. Furthermore, if one measures the amount of time that this measurement is taken, the integrated luminosity can be found. For a calculation of a cross-section, one must use the integrated luminosity, not the instantaneous luminosity. Typically in E835 the instantaneous luminosity was  $2.5 \times 10^{31} \text{ cm}^{-2}\text{s}^{-1}$ .

### 3.2. Inner Detectors

Fermilab Experiment 835 uses several layers of detectors which cover the entire azimuthal range and part of the polar angle range. These are responsible for determining the polar and azimuthal angles, tracking, and helping to identify electrons.

Cut Through E835 Inner Tracking System

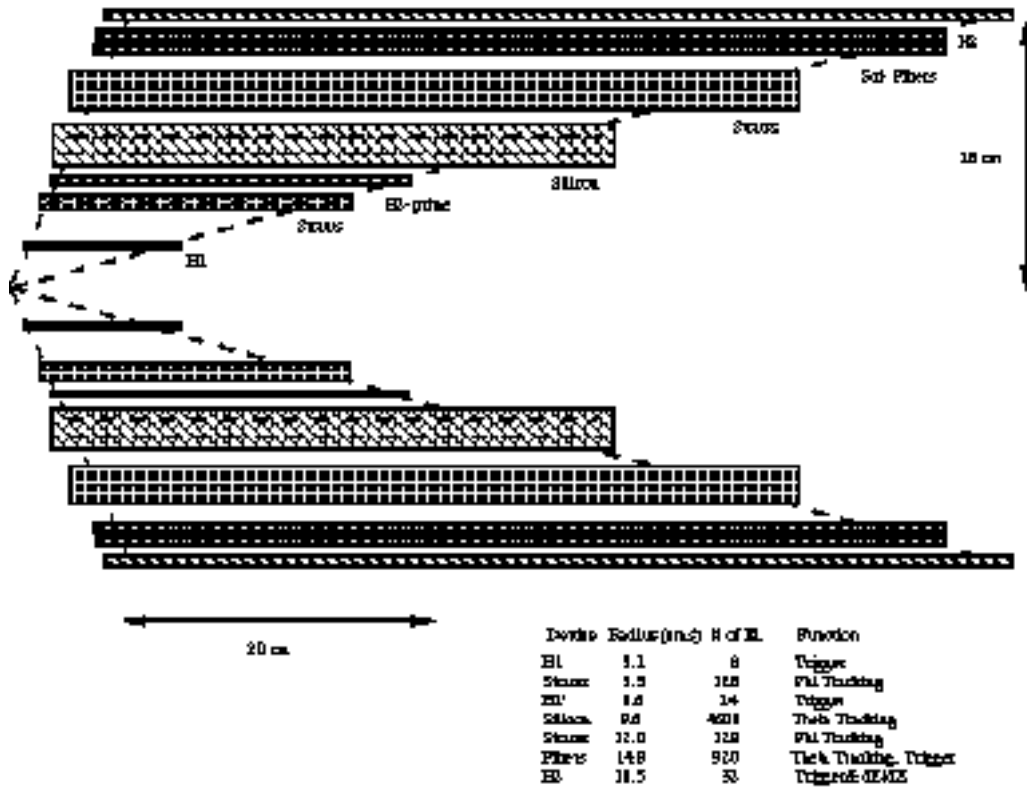


Figure 3.2 : Side View of the E835 Inner Detectors.<sup>36</sup>

There are 4 sets of hodoscopes: H1, H2, H2', and the Forward Charged Veto (FCV). Pulse heights from the first three hodoscopes (see Figure 3.2) help define charged tracks in the hardware trigger logic. The FCV is used to detect charged particles in the forward direction, and with H1 helps to form a veto on charged particles for the neutral trigger logic. E835 also implements two layers of straw tubes, a silicon pad detector, and a scintillating fiber tracker.

The straws, or more properly the aluminized mylar drift tubes, offer a

simple, reliable, and accurate way to determine the longitudinal position and azimuthal angle for the tracking.<sup>37</sup> The z-coordinate of the track is determined by charge division via the amount of charge collected at both ends. The anode wire in the drift chamber best balances the competing factors of reducing thermal noise and keeping rise times for charge collection at the ends small. Typically with a gas mixture of 87.5% argon and 12.5% carbon dioxide it takes only a few nanoseconds to collect the charge created by a particle track.

The silicon pad detector<sup>38</sup> for E835 was designed to search for the  $\chi_{c0}$  decay of the pseudoscalar states, whose primary decay channel of 2 photons is contaminated by feed-down from  $\chi_{c0}$  and  $\chi_{c1}$  events, and the eventual decay of each  $\chi_{c0}$  into charged kaons. Its spatial resolution of 2 mrad in azimuth and 3 mrad in the lab polar angle and fast readout also serve to correlate spatial measurements from the other inner detectors. This cylindrical detector covers 360 degrees in azimuth and 15 to 65 degrees in the lab polar angle.

Another measurement of the lab polar angle was given by the scintillating fiber tracker.<sup>39</sup> The two-layer tracker (radii of 14.4 cm and 15.06 cm) can accommodate the increased luminosity of E835 over E760 by delivering an efficiency of more than 99% during peak luminosity runs. Light coming from each of the 860 fibers (core radius of 370  $\mu$ m) is read out by solid state devices

called VLPC's (Visible Light Photon Counters) with a high quantum efficiency (i.e. a very high signal-to-noise ratio). Like the silicon pad detector, the fiber tracker covers 15 to 65 degrees in lab polar angle and 360 degrees in azimuth.

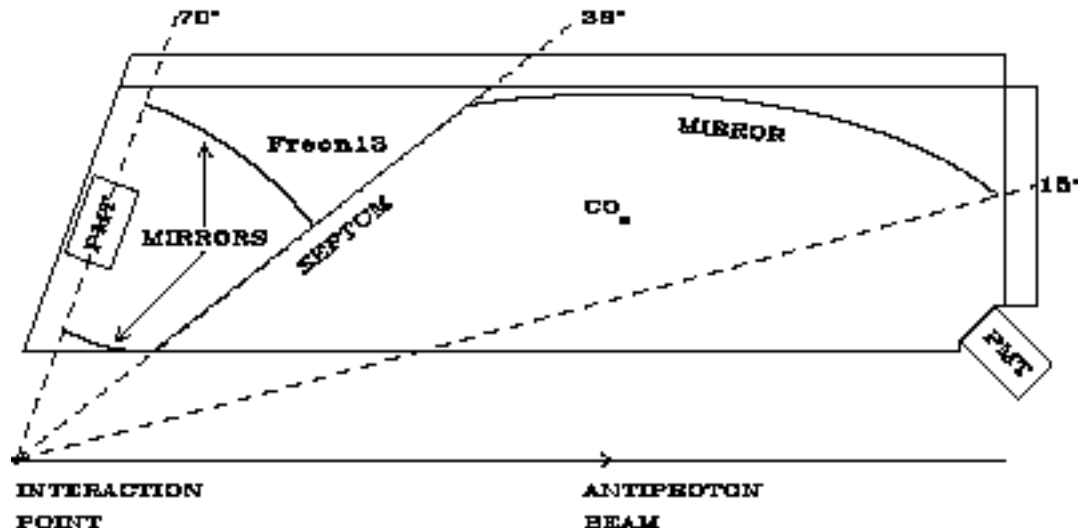


Figure 3.3 : Cross section of the Cerenkov detector.<sup>40</sup>

A threshold gas Cerenkov detector<sup>41</sup> (Figure 3.3) serves to reject charged pions from electrons, and thus help one pick out an electromagnetic signal from the huge hadronic background. It is divided into 8 azimuthal sections (45 degrees each), with each of these divided into 2 polar regions with 2 different gases. Each of the polar regions are operated at atmospheric pressure and room temperature.

On one hand, the gas chosen had to have an index of refraction small

enough so that the threshold velocity at which Cerenkov light was produced ( $\beta_{th} = 1/n$ ) was higher than the velocity of either pion from the direct production of 2 charged pions. On the other hand, it had to be large enough to maximize the yield of Cerenkov light. Furthermore, both gases had to be low light-absorbing and non-explosive. As a result, CO<sub>2</sub> was chosen for the forward region and Freon 13 for the backward region. Cerenkov light was then reflected by mirrors onto photomultiplier tubes, and then read out by analog to digital converters (FERA).

### 3.3. Central Calorimeter

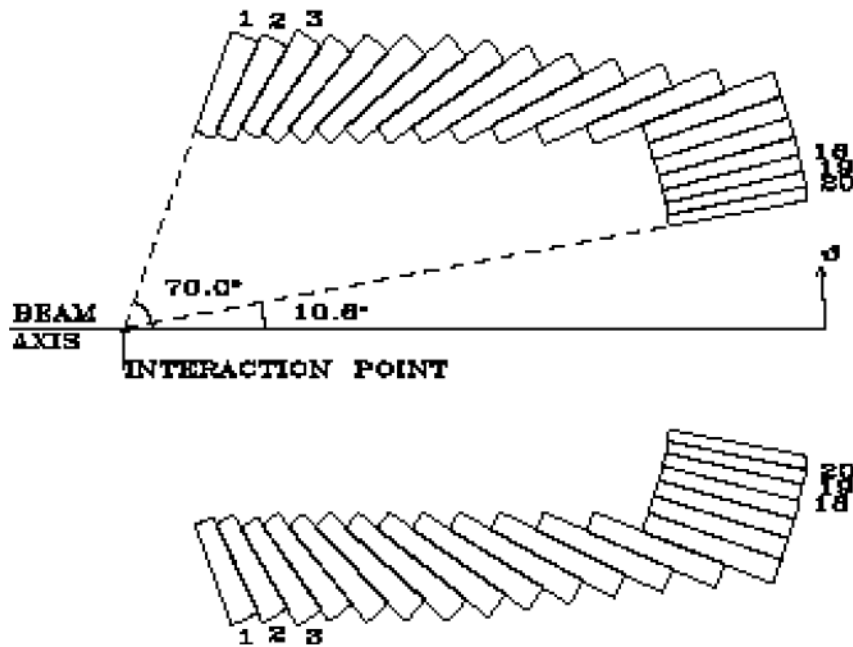


Figure 3.4 : One wedge of the Central Calorimeter.<sup>42</sup>

The heart of the experiment is the central calorimeter (CCAL). The CCAL consists of 1280 lead-glass blocks arranged so that there are 20 'rings' (Figure 3.5) and 64 'wedges' (Figure 3.4). Each of the 64 blocks in a particular ring shares the same polar angle (20 rings X 64 wedges/ring = 1280 blocks), and each of the 20 blocks in a wedge shares the same azimuthal angle (64 wedges X 20 blocks/wedge= 1280 blocks). The CCAL covers the entire azimuthal range and all polar angles between 11 and 70 degrees, where the z-axis is defined by the direction of the antiproton beam. The faces of all 1280 blocks point towards the center of the interaction region where the antiproton beam intersects with the hydrogen gas jet.

Each lead glass block responds to photons and electrons by creating electromagnetic showers. When these shower particles travel faster than the speed of light within the lead glass, they produce Cerenkov light, which is collected by Hamamatsu photomultiplier tubes.

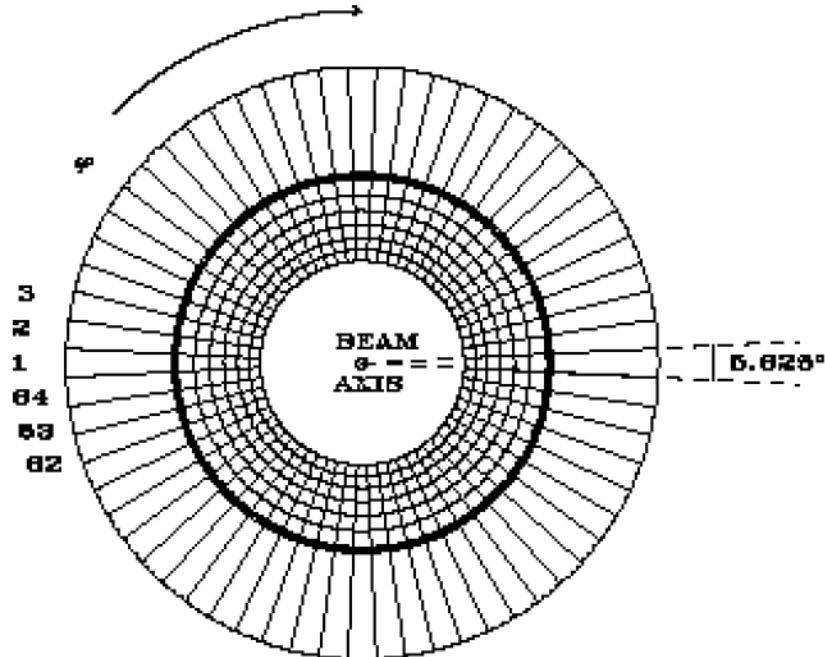


Figure 3.5 : One ring of the Central Calorimeter.<sup>43</sup>

The CCAL was designed to identify the charmonium signal from a large background, which primarily comes from the process  $p\bar{p} \rightarrow 2\gamma$ . If one or both of the  $\gamma$ 's decay asymmetrically and the low energy photon is not detected, then this event may mimic a  $2\gamma$  or a  $3\gamma$  event. As a result, photons with an energy of greater than 50 MeV must be detected with an efficiency of greater than 95 %. On the other hand, it has to resolve both photons from a symmetric  $\gamma$  decay, where the opening angle can be quite small.

The granularity of this calorimeter was found via a Monte Carlo simulation, which required that a symmetrical  $\gamma$  would produce two resolvable

clusters in the CCAL at the highest formation energy intended for the experiment. Each of the lead-glass blocks subtends different polar angles as a result: 1.1 degrees in the forward direction to 5.2 degrees in the backward direction. Using the same Monte Carlo, it was shown that in order to reject background events, it is more critical to contain as much of the shower as possible for low energy photon detection than it is to optimize the energy resolution. Thus block lengths were chosen to contain 90-95 % of the shower's energy.<sup>44</sup>

The CCAL is calibrated by looking at  $\pi^0\pi^0$  events.<sup>45</sup> During data taking, an event is selected to be written to a calibration tape. A DST (Data Summary Tape) is produced to include  $\pi^0\pi^0$ ,  $\pi^0\pi^+$ , and  $\pi^+\pi^+$  events that have an acoplanarity  $< 0.1$  and  $\Delta\phi < 0.05$ . Acoplanarity measures how different the two mesons come out in their azimuthal angles, and  $\Delta\phi$  measures how different the two mesons are produced in their center-of-mass polar angles. If the event is an exclusive 2-meson event, the mesons are produced back-to-back in the center-of-mass, and both these quantities are zero.

The CCAL cluster thresholds are set at 25 and 50 MeV (at least 25 MeV for the seed block, and at least 50 MeV minimum for an entire cluster). The offline clusterizer routines reconstruct events from the energy deposits in the central calorimeter by searching for "seed" blocks around which to build a

cluster of energy deposits representing a particle track through the CCAL. No timing cuts are incorporated for the clusters via the TDC's (time to digital converters), but only events with 4 clusters get written to the DST, which is used to determine the location of the interaction vertex in the subsequent analysis.

Once the DST has been created, a subset of  $\pi^0\pi^0$  events are selected. Here the acoplanarity must be less than 0.032, the  $\pi^0$  kinematics must be less than 0.01, and the mass of each reconstructed  $\pi^0$  must be within 40 MeV of the  $\pi^0$  mass quoted by the Particle Data Group, 135 MeV. Gain constants are evaluated by iterating over this subset using the pedestal subtracted adc count (analog to digital conversion produced by the FERA's) for each block. These new gain constants are used to find  $\pi^0\pi^0$  events in this DST, and one scales these gain constants in order to arrive at the proper mass of the  $\pi^0$ , 548 MeV.

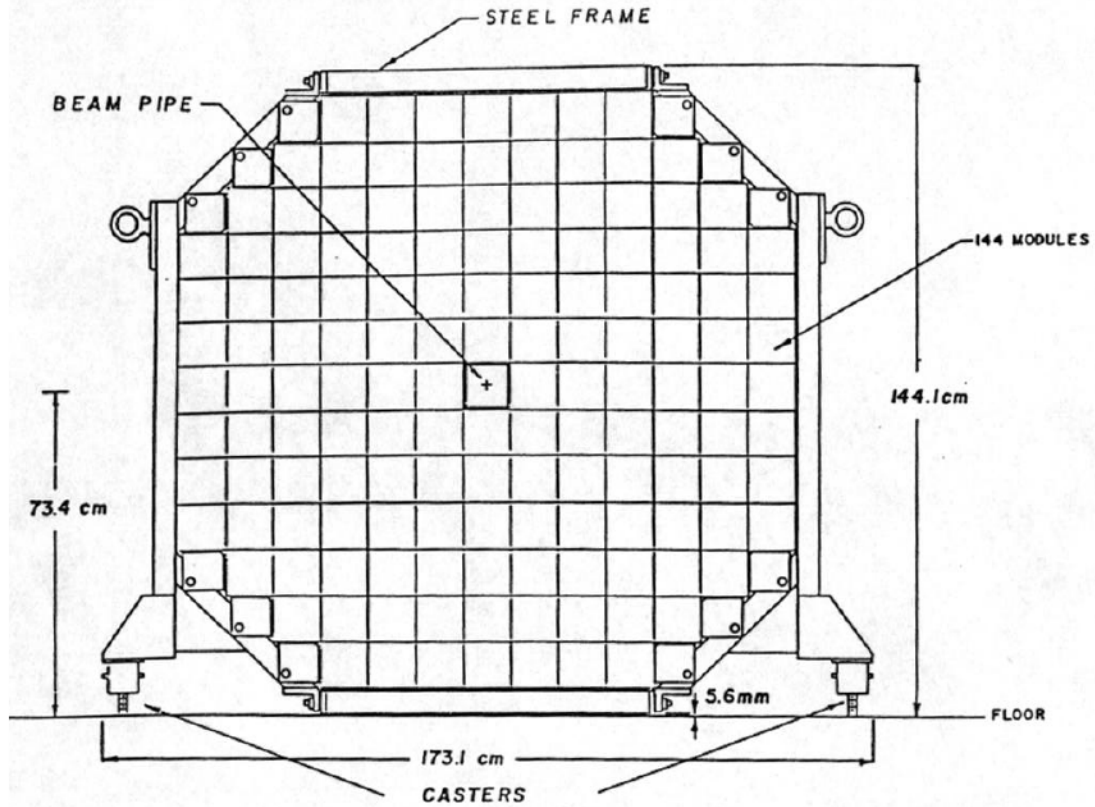


Figure 3.6 : Front view of the Forward Calorimeter.<sup>46</sup>

### 3.4. Forward Calorimeter

A forward endcap calorimeter (Figure 3.6) is also included among the detector elements of the experiment. Since the charmonium signal must be extracted from a huge hadronic background, the forward calorimeter must be able to detect single photons down to about 60 MeV. The largest background to the decay  $\psi \rightarrow \gamma \gamma$  is  $2\pi^0$ , and either both  $\pi^0$ 's decay asymmetrically or one of the soft photons are not detected and thus this channel can contribute to the

background for the  $\bullet_c$ .

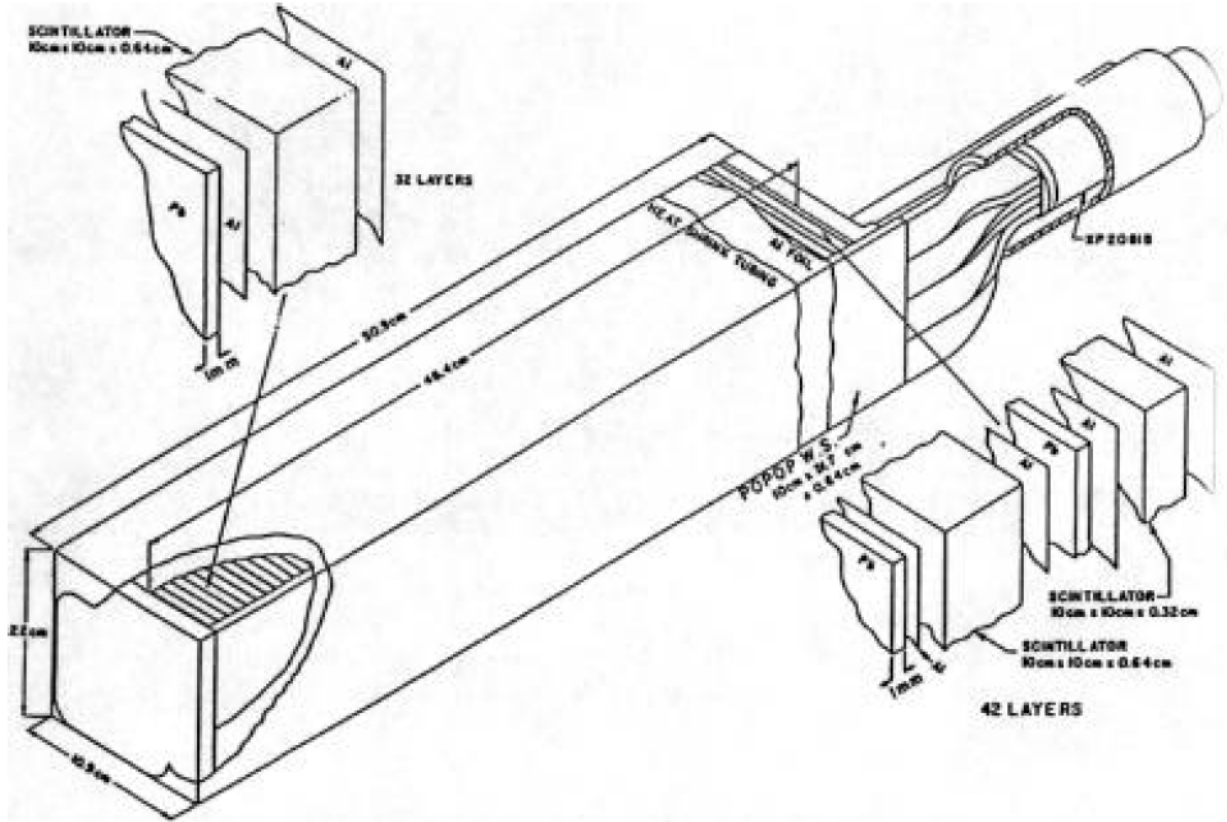


Figure 3.7 : Forward Calorimeter Module.<sup>46</sup>

The forward calorimeter<sup>46</sup> is a sampling electromagnetic calorimeter. Centered upon a 13X13 grid that is 3 meters from the interaction point, with the beam pipe going through the center, 144 modules are stacked at the end of the central calorimeter. Blocks do not exist at the corners of 13X13 grid since this area is blocked by the central calorimeter. Each module is 51 cm long and has transverse dimensions of 10 cm X 10 cm. Within each module are 148 alternating layers of lead and acrylic scintillator that were compressed and

shrink-wrapped together. A POPOP wavelength shifter lies along one side of each FCAL module to transmit light to the PMT's (photomultiplier tubes) and on to the data acquisition system.

## 4. Data Acquisition

Detectors for the experiment are located in the pit of the AP-50 target hall at Fermilab. As events are selected by hardware triggers located near the interaction vertex of the hydrogen gas jet and the antiproton beam (which determine whether the event should be kept or passed over), the respective pulse heights from various detectors are sent upstairs through delay cables to the AP-50 Counting Room. Further decisions are made via software regarding which events are worth keeping and written to tape and/or disk.

The data are often referred to by their run number. Generally a "run" is the running of the data acquisition system and the writing of event information to tape. A new run begins when one of the many tapes becomes full of data and a new set of tapes must be used. Each run has its own set of calibration constants in the E835 database.

The basic philosophy of the E760/E835 trigger is to base decisions on a more manageable number of components than the 1280 elements of the CCAL while at the same time requiring at least two significant deposits of transverse electromagnetic energy (i.e. hopefully a  $e^+e^-$  or  $\mu\mu$  signal). This is achieved by analog summing adjacent calorimeter blocks into 40 super-clusters. The summing process includes overlaps so that most of the energy from the transverse spread of a shower may be contained within a single super-cluster,

and higher trigger rates are avoided by setting proper thresholds.<sup>47</sup>

#### 4.1. The Trigger

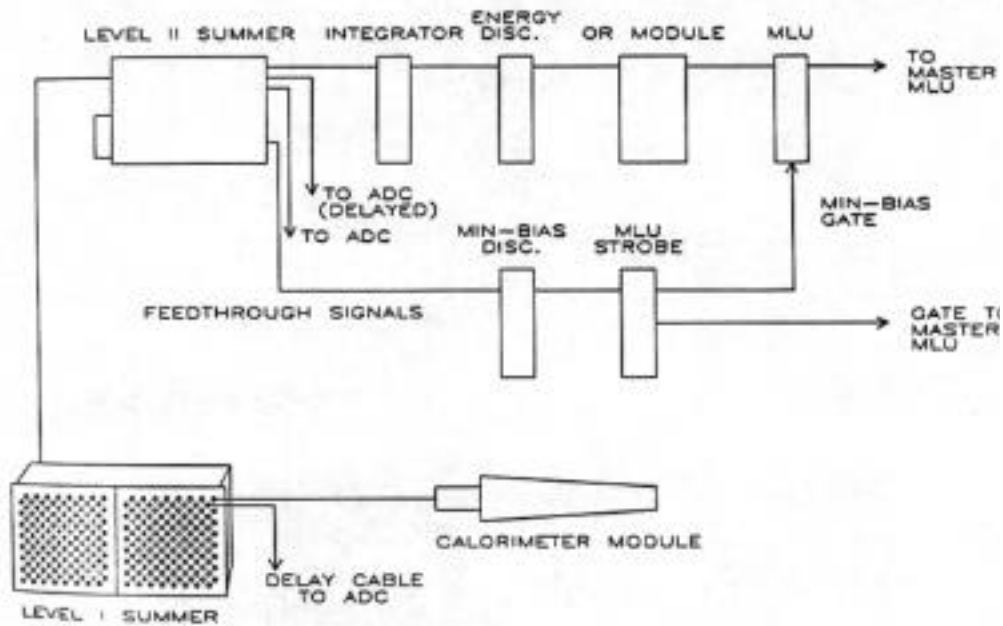


Figure 4.1 : The CCAL Trigger Logic.<sup>47</sup>

Initially, the signal from each of the 1280 blocks is split: 95 % is sent through a delay cable to the ADC's , and 5 % is delivered to the Level I Summer (Figure 4.1). Ultimately if the event passes certain requirements set on these super-clusters and/or the inner detectors, a gate signal will be sent by the Gatemaster (an event must pass the requirements of at least one hard-wired trigger in this logic unit) to the FERA's, allowing them to read in the analog signals from the previously mentioned delay cables. Otherwise the event is rejected.

Signals within each wedge of 64 blocks are summed into one of 8 super-wedges, i.e. a super-wedge is a pure azimuthal sum. Each super-wedge is actually a sum of 9 blocks due to the overlap mentioned earlier. Hence the first and last blocks in a ring are included in two different sums. Since there are 20 such wedges, the Level I Summer produces  $20 \times 8 = 160$  signals.

These 160 Level I signals are sent to the Level II Summer, which sums all Level I signals sharing one of the 8 azimuthal regions into 5 polar regions called super-rings, which overlap with the adjacent super-ring by one calorimeter block. Since there are 8 azimuthal regions and 5 sums performed in each region, there are  $8 \times 5 = 40$  super-clusters.

The requirement of having at least two significant deposits of transverse electromagnetic energy translates into requesting two such deposits to be a) coplanar and b) have an invariant mass of greater than 2.0 GeV. Usually the coplanar requirement means that the super-clusters must be back-to-back in the center-of-mass frame, which means that the other energy deposit must lie in the directly opposite super-cluster (called a "1 vs. 1" geometry). However, this can be softened to a 1 vs. 3 geometry: The other energy deposit is in one of the 3 opposing super-clusters in the center-of-mass.

This constitutes the main body of the trigger. Other requirements, such

as using or vetoing on different detectors or changing the invariant mass threshold, may be added to produce different triggers. Several different hardware triggers are flagged as on or off by the Gatemaster, including a  $e^+e^-$  trigger,  $\mu^+\mu^-$  trigger,  $\mu\mu$  trigger,  $\mu\mu\mu$  trigger, and several calibration triggers.

## 4.2. DART Hardware

To get events flagged by the Gatemaster written to tape, they must pass through the hardware of the E835 data acquisition system (Figure 4.2). The E835 DAQ is based on the architecture of the DART Data Acquisition Project shared among several fixed target experiments at Fermilab. DART provides a common system of hardware and software that can be easily configured across a variety of UNIX and VME platforms.<sup>48</sup>

In regards to hardware, the E835 DAQ uses three Silicon Graphics computers and one Motorola MVME167 processor. One Silicon Graphics Indy runs the programs that perform Run Control, executes the Data Acquisition Monitoring Program (DAMP), and talks to the two CAMAC branches. A Challenge-L takes advantage of four 150-MHz processors to build and filter events, and then log them to tape. An Indigo is used for monitoring the detectors and runs the Event Display, in which signals for all the detector elements for a chosen event may be viewed graphically.<sup>49</sup>

Data from the detectors are read out via TDC (LRS3377)<sup>50</sup> in a common start mode and either by FERA ADC (LRS4300)<sup>51</sup> or PCOS Latches (LRS2731)<sup>52</sup> through the ECL-ports in the controller's front by Damn Yankee Controllers (DYC).<sup>53</sup> The TDC's (time-to-digital converters) help determine if a particular hit in the detector is on-time or not associated with this event. ADC's (analog-to-digital converters) convert the analog signals delivered by the detectors' photomultiplier tubes into digital information for further processing. When properly calibrated, the ADC's yield information about the energy of a hit in the detector for example. A data stream is formed by daisy-chaining DYC's together by a DART ribbon cable form streams, and each stream is read out by two pairs of Access Dynamics DC2/DM115 modules.<sup>54</sup>

The DC2 writes its data to one of the Dual Ported Memories (DPM) using a "ping-pong" algorithm. A process on the Challenge called Gateway reads the "ping" memory while the DC2 writes to the "pong" memory. A third DPM serves as a mailbox which is constantly polled by the processes that write and read to the first two Dual Ported Memories to see when the other is finished.<sup>55</sup>

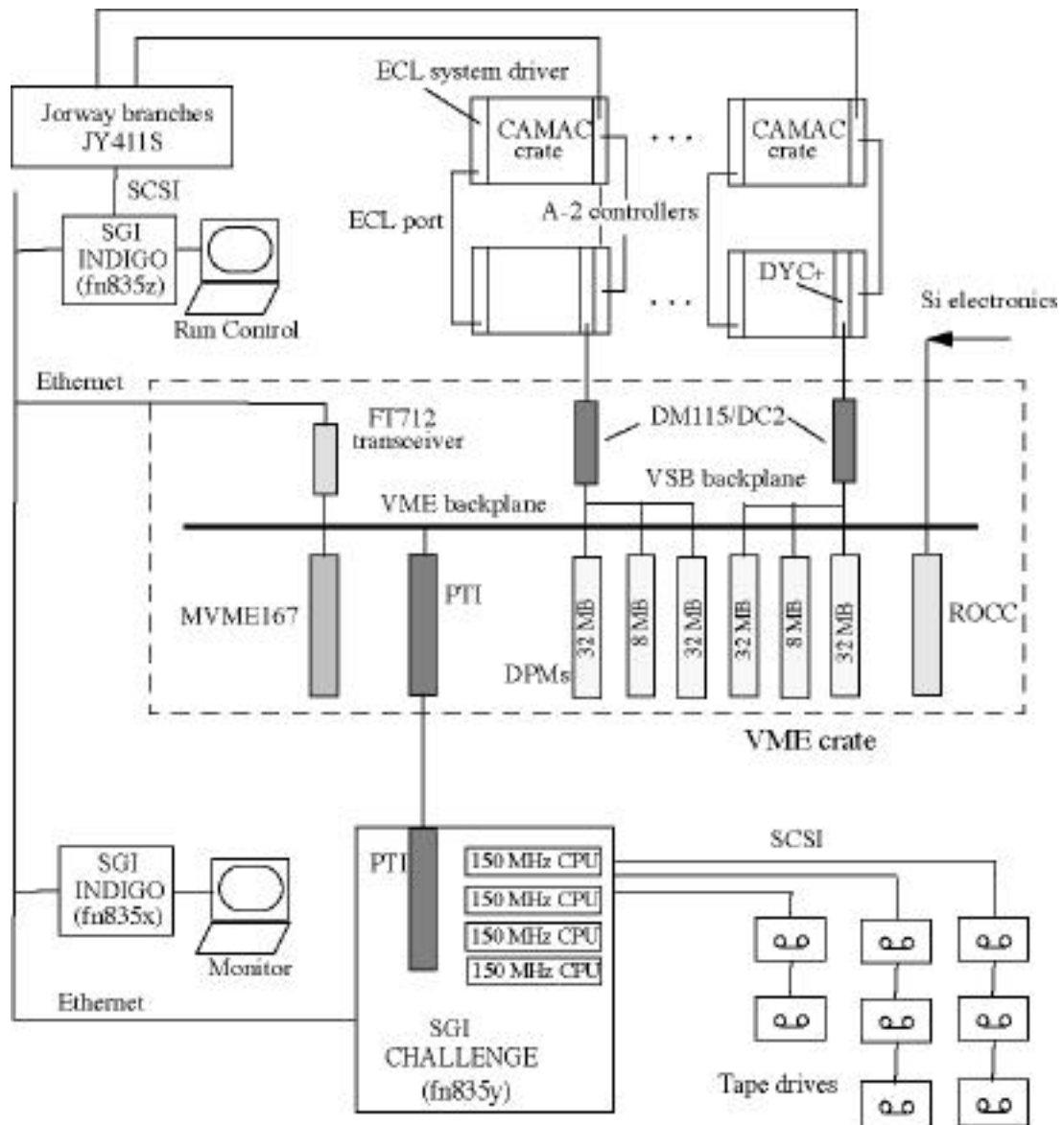


Figure 4.2 : Hardware of the E835 Data Acquisition System.<sup>56</sup>

The event header,<sup>57</sup> which in effect lists the locations of different parts of the event data within the data stream and how much information is within each event, is constructed in the PRUDE filter program, which includes pointers

locating information in the body of the event from individual DYC's, denoting which hardware triggers fired, etc. If the topology of the event matches certain software triggers, it is further analyzed in the PRUDE filter program (Please Remove Unwanted Events), and written to the appropriate buffer, which is most often a tape drive for storage. Just as the number of gates sent out to the FERA's by the triggers are prescaled, so too are the number of events that get written to different buffers of the Challenge. Thus not every event that passes one of the internal software triggers in PRUDE gets written to tape. However, a certain percentage of events are automatically written to buffers for calibration purposes via an autopass trigger regardless of whether it passes any of software triggers included in PRUDE. Rebuilt events from PRUDE may either be sent to a process called DOT (Data On Tape) to write the event to tape or to a process named HOIST, which serves the event display and the E835 Consumer program used for on-line monitoring.

One may change the many variables associated with each software and hardware trigger via a graphical interface built from the Tcl/Tk language.<sup>58</sup> For instance, one may want to activate or deactivate certain triggers before the run starts, change how often data passing a certain trigger gets written to a buffer (prescaling), or assign different buffers to the various triggers. Furthermore, one may want to create a new trigger, rename a trigger, view all the trigger bits making up each software trigger, or change the priorities of all the hardware triggers.

### 4.3. DART Software

The DART software architecture (Figure 4.3), of which the PRUDE filter is the central member, is highly functional and flexible. A client-server protocol over TCP/IP sockets forms the basic structure. Buffers are managed via a service provider/requestor algorithm, and the same application may be a provider in one circumstance and a requestor in another. Applications are registered with one or more groups, and different applications communicate through run control via group multicasting.<sup>59</sup> In other words, Run Control will send messages to all the members of a registered group.

The data acquisition is controlled via a single program called the Operator Control Program (OCP) through a user interface, which may occur via a command line or a graphical user interface (GUI). E835 uses a GUI to update the configuration database and start applications over several different nodes (i.e. several different SGI machines). DART provides a library of functions to allow applications to connect to servers, register to groups, and perform any kind of transaction. OCP is written in Tcl/Tk, which allows one to bind commands to buttons and exchange parameters in the database via entry boxes that one can type in.

## DAQ PROCESSES

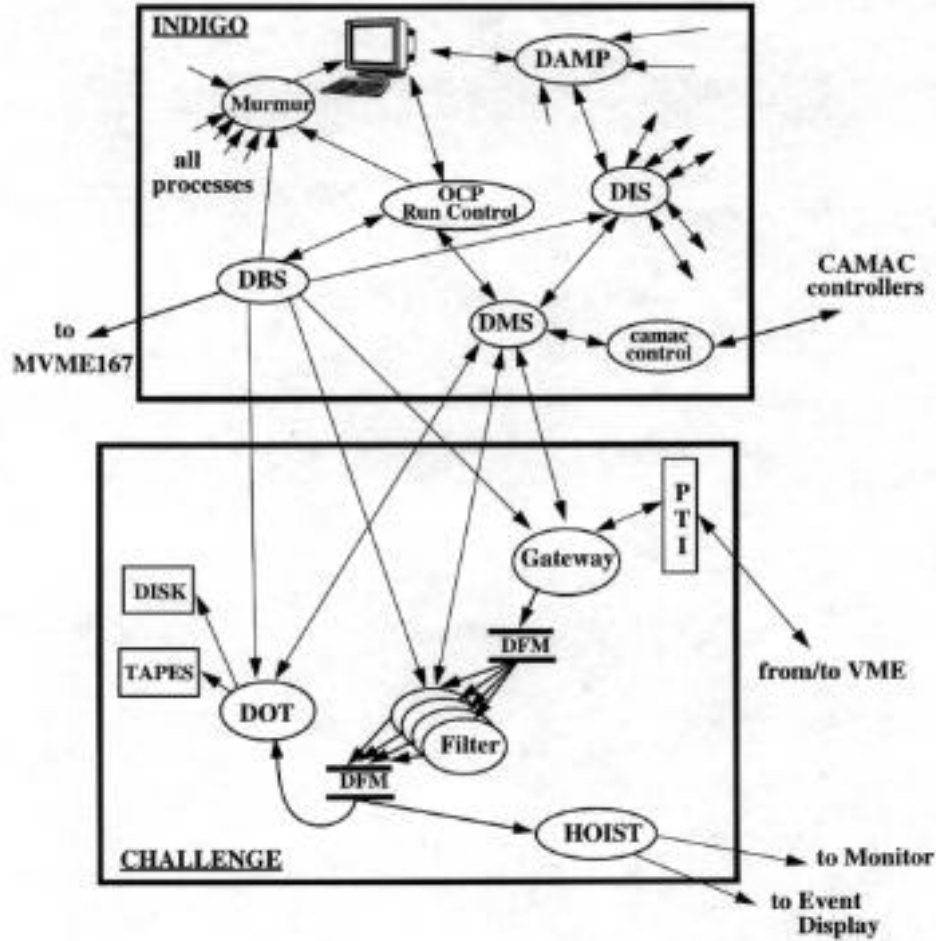


Figure 4.3 : Active DART software processes for the DAQ.<sup>60</sup>

There are several servers that run while data acquisition is taking place. The two primary applications are the filter, which builds events from buffers passed to it via 3 different data streams, and the logger, which writes events that have passed certain hardware or software trigger requirements to tape or disk, as shown in Figure 4.4.

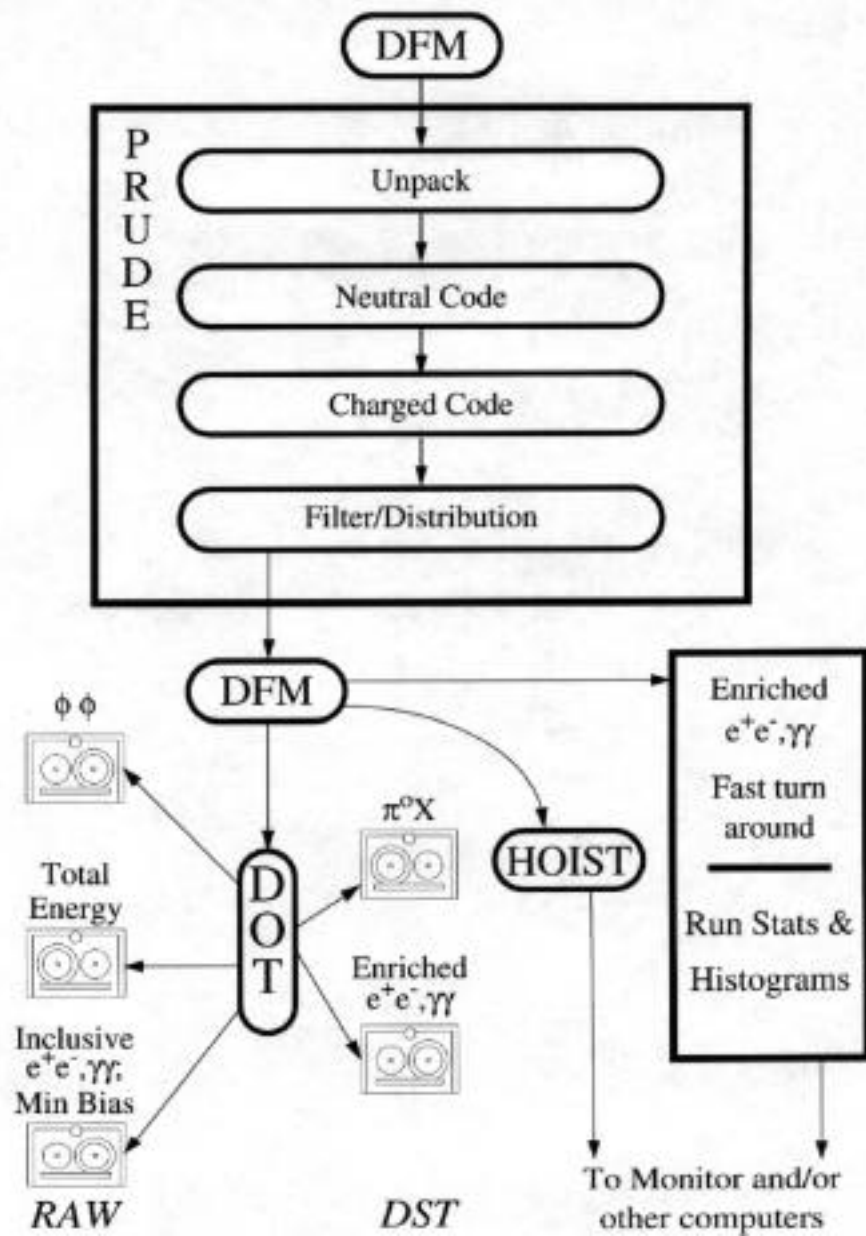


Figure 4.4 : The filter PRUDE and the logger.<sup>58</sup>

However, in such a dynamic environment, buffers must be properly scheduled and organized to rebuild an event successfully, and all applications must be able to report errors and know where to look for buffers and/or messages. Furthermore, one wants to be able to monitor various rates and statistics for different processes. The DIS framework (distributed information services) was designed by DART to perform these functions. A database of parameter values (numbers or strings) for each application is stored for a particular configuration (i.e. pure calibration, the taking of pedestals, and general data acquisition), and these statistics may be accessed during a run for monitoring purposes.

A server called DFM (data flow management) distributes buffers among various processes. Requestors queue buffers to different service providers that will use them. DFM schedules buffers via a list of buffer descriptors, which provide information about the buffer locations.

Messages from one application are multicast to all other processes of the same registered group via DMS (distributed multicasting services). The advantages of DMS are that messages can be distributed to applications on several different nodes as long as they are registered to the same group, commands are executed across the whole group, and members may join or leave groups dynamically. The application sending the message will wait for a reply from all members of the group before continuing.

DAQ (data acquisition) statistics may be monitored via DAMP, the Data Monitoring Program. DAMP provides a GUI builder (Graphical User Interface) to dynamically change the presentation of statistics (logging rates, percentage of tape used, buffer information) using various strip charts, bar graphs, etc. DAMP is closely related to the DIS server in the manner in which it accesses parameters.

A certain percentage of events are “hoisted” to the on-line monitoring program called Consumer. Events are funnelled to various histograms, which may be dynamically viewed on-line by running Histoscope. In Histoscope, one can also dynamically adjust the binning of the histograms by clicking and dragging an axis with the mouse.

#### 4.4. Dead Time

There are two dead times for the experiment.<sup>61</sup> One of these is caused by the Data Acquisition System itself. While the DAQ is processing an event, all triggers are vetoed, and therefore all events occurring during this “dead time” are lost. Run at a constant rate of  $2.5 * 10^{31} \text{ nb}^{-1}$ , the experiment was dead 2% of the time due to the DAQ (i.e. number of triggers lost compared with total number of triggers).

The second type of dead time is caused by the detectors themselves. Due to the high event rate, a veto counter may incur an accidental hit. If a trigger was formed but this veto counter was on, the event was disregarded. A study was done by looking at the veto counters in randomly opened gates during data taking, and it was determined that this contributed a dead time of about 10% to the experiment.

#### 4.5. Operations

During 8-hour shifts around the clock the data acquisition system, various gas bottles used by the inner detectors, the status of the hydrogen gas jet, and the status of the detector elements are monitored. The E835 Monitor program looks after the DAQ and the various detector elements, a MacIntosh serves to monitor the gas jet, and gas levels are periodically examined manually.

Several programs run during each shift are necessary for the proper operation of the experiment. One of the programs critical to the basic operation of the experiment is the High Voltage Program.<sup>62,63</sup> E835 uses six LeCroy 1440 high voltage mainframes to power the photomultiplier tubes used by the hodoscopes, Cerenkov counters, central calorimeter, and forward calorimeter.

The E760 version of the program provided a text-based interface that wrote commands to, and read responses from, the RS232 port of the Controller for each 1440 mainframe. Since E835 does not use any VAX-based computers, the program's I/O routines had to be rewritten in order to communicate with the 1440 via a serial port on an SGI running UNIX. UNIX does not provide a set of easy-to-use I/O routines such as the SYS\$QIOW routine that VAX does.

A High Voltage Monitor Program<sup>64</sup> is also available to alert Run Control of any changes in the status of the LeCroy mainframes during a shift. The program polls the mainframes every so often and reports an error if a mainframe does not respond to a command, the response is abnormal, or the voltage read back is outside a certain window. Both the High Voltage Control Program and the High Voltage Monitor are designed to lock out the SGI serial port so only one user may have access to the high voltage mainframes at any one time.

Pedestals for the experiment may be taken at any time by running the data acquisition system software in the pedestal configuration. Usually 10-20,000 events generated by a pulser are taken, and the pedestal program<sup>65</sup> then evaluates means and widths for every FERA ADC channel in the experiment. One problem that the pedestal program must address is spurious large hits due to large cosmic rays that may pass through the detector at the time the gate is opened. One or two such hits per channel may dramatically impact the pedestal mean. To alleviate this problem, a subset of a couple

hundred events are used to establish a mean plus  $3 \cdot \sigma$  window (If  $\sigma$  is too small, then the default window is mean plus 30 ADC counts). If a pedestal is larger than this threshold, it is not used in the evaluation of the pedestal mean for that channel.

Once the requested number of events have been taken, the pedestal program opens an interface which reports how many and what kind of errors occurred, and logs error information for each channel to a file. The user may view the current pedestals, compare them with a different set of pedestals, or write the pedestals to a file or to the E835 database.

Pedestals and calibration constants for the experiment are stored in the E835 database by the mSQL database package. The package includes routines to write and read entries of the columns (or fields) of tables, which form the structure of the database. A product called DBMSQL has been installed on both offline and online machines, so that run-time DAQ applications may access the database as well as offline analyses.<sup>66</sup>

## 5. Theory of Angular Distributions

### 5.1. Helicity Formalism

Typically when examining collisions, a fixed direction is chosen in order to classify the various polarization states of a particle. In the helicity formalism, states are labelled by the component of the total angular momentum along the direction of the particle motion. This avoids the relativistic complications inherent in breaking up the angular momentum operator into a spin- and an orbital- part.<sup>67</sup>

Another advantage of the helicity formalism pertains to two-particle helicity states. Within the center-of-mass frame, the orbital angular momentum is always perpendicular to the relative motion of the two particles. Defining the helicity of the state as

$$\lambda = \frac{\vec{J} \cdot \vec{p}}{|\vec{p}|}, \quad (5.1)$$

the component of spin along the direction of relative motion will also be the component of the total angular momentum along this direction,<sup>68</sup> since

$$\vec{J} = \vec{L} + \vec{S} \text{ and } \vec{L} \cdot \vec{p} = 0.$$

The helicity quantum number  $\lambda$  is also invariant with respect to ordinary

rotations. In other words performing a rotation on a state will change the direction of the momentum (keeping its magnitude constant), but the helicity quantum number does not change during this operation. However, as seen by the equation above, if the momentum vector is rotated by 180 degrees, the helicity quantum number changes sign.

Given a set of total angular momentum operators ( $J_x, J_y, J_z$ ) and three Euler angles ( $\alpha, \beta, \gamma$ ) it is customary to describe a rotation by

$$R(\alpha, \beta, \gamma) = e^{-i\alpha J_x} e^{-i\beta J_y} e^{-i\gamma J_z}. \quad (5.2)$$

In the helicity formalism, one wants to rotate the momentum vector away from the z-axis to the direction ( $\theta, \phi$ ) in a unique manner, so ( $\alpha, \beta, \gamma$ ) is ( $\phi, \theta, 0$ ).

In the basis formed by angular momentum eigenvectors, the matrix element of this rotation matrix is

$$\langle J' M' | R(\alpha, \beta, \gamma) | J M \rangle = \delta_{JJ'} D_{MM'}^J(\alpha, \beta, \gamma). \quad (5.3)$$

The rotation matrix D for a specific total spin J can thus be found by inserting the expression for a general Euler rotation between two states of the same J. This

rotation matrix is represented as

$$D_{MM'}^J(\alpha, \beta, \gamma) = e^{-i\alpha M} d_{MM'}^J(\beta, \gamma) e^{-i\gamma M'}, \quad (5.4)$$

where

$$d_{MM'}^J(\beta, \gamma) = \langle JM' | e^{-i\beta J_y} | JM \rangle. \quad (5.5)$$

In other words, when we perform a rotation upon a particular angular momentum state, the rotation matrix supplies the coefficients of the new rotated state in terms of all the  $2J+1$  angular momentum states making up the basis for this vector space.<sup>69</sup>

Using the above tools and a knowledge of the S-matrix, one may determine the matrix element for a process  $a + b \rightarrow c + d$  in the center-of-mass, where  $a$  and  $b$  lie along the Z-axis, and the relative momentum of  $c$  and  $d$  is rotated to the direction  $(\alpha, \beta)$  for one given set of helicities.

Suppose that initially we have two particles  $a$  and  $b$  heading toward each other along the z-axis, and the collision produces two other particles  $c$  and  $d$ . In our case,  $a$  and  $b$  might represent the proton and the antiproton. The relative momentum vector of  $c$  and  $d$  is rotated by the angles  $\alpha$  and  $\beta$  away from the z-axis in the center-of-mass frame. Jacob and Wick express this S-matrix



as

$$\frac{1}{4p} \sum_J (2J + 1) \langle \cdot \cdot \cdot_c \cdot \cdot \cdot_d | S^J(E) | \cdot \cdot \cdot_a \cdot \cdot \cdot_b \rangle D_{\cdot \cdot \cdot}^{J \cdot \cdot \cdot}(\cdot \cdot \cdot; \cdot \cdot \cdot) \quad (5.10)$$

Here  $\cdot$  is the difference of the final state helicities (c and d), and  $\cdot$  is the difference of the initial state helicities (a and b). The total amplitude considers all possible values of total angular momentum J. However, we only concern ourselves with J=1 because of the vector nature of the  $J/\cdot$  and  $\cdot \cdot \cdot$ .

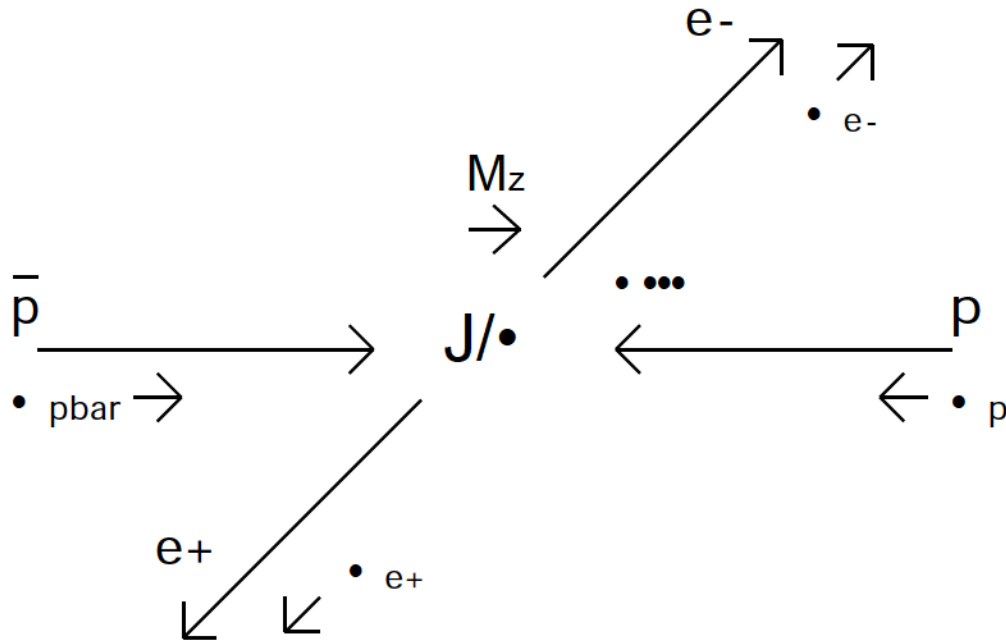


Figure 5.1 : Decay of the  $J/\psi$  or  $\psi'$  in the helicity formalism.

For the decay process  $\bar{p} p \rightarrow J/\psi \rightarrow e^+ e^-$  shown in Figure 5.1, two stages must occur:  $\bar{p} p \rightarrow J/\psi$  and  $J/\psi \rightarrow e^+ e^-$ . To derive the matrix element, one first multiplies an amplitude by a rotation matrix for both the

production and decay stages, and then sums over all possible intermediate states  $M_z$  of the vector state  $J/\psi$  since the  $J/\psi$  is unobserved<sup>70</sup>:

$$M\left(\lambda_{\bar{p}p}, \lambda_{e^+e^-}, J\right) = \sum_{M_z} \left\{ C_{M_z} D^{J^*}_{\lambda_{\bar{p}p}, M_z}(0,0,0) \right\} \left\{ B_{\lambda_{e^+e^-}, M_z} D^{J^*}_{\lambda_{e^+e^-}, M_z}(\lambda_{\bar{p}p}, \lambda_{e^+e^-}) \right\}. \quad (5.11)$$

Here  $\lambda_{\bar{p}p}$  refers to the difference in helicity between the proton and antiproton, and  $\lambda_{e^+e^-}$  refers to the difference in helicity between the electron and the positron. The first rotation matrix above is a delta function, meaning  $\lambda_{\bar{p}p} = M_z$ . The first term in brackets describes the production of a charmonium state at the origin with a polarization given by  $M_z$ , and so only one term contributes from this sum. Hence we have

$$M\left(\lambda_{\bar{p}p}, \lambda_{e^+e^-}, J\right) \propto \left\{ C_{\lambda_{\bar{p}p}} \right\} \left\{ B_{\lambda_{e^+e^-}, \lambda_{\bar{p}p}} D^{J^*}_{\lambda_{e^+e^-}, \lambda_{\bar{p}p}}(\lambda_{\bar{p}p}, \lambda_{e^+e^-}) \right\}. \quad (5.12)$$

After this matrix element is squared, it must be averaged over the initial  $\bar{p}p$  states and summed over the final  $e^+e^-$  states to get the differential cross section. This means summing over all possible helicity combinations of the



antiproton, and then sum over all possible combinations for the electron and positron:

$$\langle M^2 \rangle \propto \sum_{\substack{\bullet \bullet \\ p p}, \substack{\bullet \bullet \\ e^+ e^-}} B^2 \cdot \substack{\bullet \bullet \\ e^+ e^-} C^2 \cdot \substack{\bullet \bullet \\ p p} \left( d^1_{\substack{\bullet \bullet \\ p p}, \substack{\bullet \bullet \\ e^+ e^-}}(\bullet \bullet) \right)^2. \quad (5.15)$$

In the process of squaring the rotation matrix, the exponential factors have canceled with their complex conjugates, so the angular distribution does not depend upon the azimuthal angle of the electrons in the center of mass frame. The sum is now performed over  $\bullet \bullet_{p p} = -1, 0, 0, 1$  and  $\bullet \bullet_{e^+ e^-} = -1, 1$ . Since

we are only interested in the shape of the angular distribution, and  $B_1^2$  is common to every term in this sum due to parity, we may safely factor it out.

Using the following  $d$  functions for  $J=1$ ,

$$d^1_{11}(\bullet \bullet) = d^1_{-1-1}(\bullet \bullet) = \cos^2\left(\frac{\bullet \bullet}{2}\right); \quad (5.16)$$

$$d^1_{1-1}(\bullet \bullet) = d^1_{-11}(\bullet \bullet) = \sin^2\left(\frac{\bullet \bullet}{2}\right); \quad (5.17)$$

and 
$$d^1_{01}(\bullet \bullet) = d^1_{0-1}(\bullet \bullet) = \sqrt{2} \sin\left(\frac{\bullet \bullet}{2}\right) \cos\left(\frac{\bullet \bullet}{2}\right); \quad (5.18)$$

one arrives at the final form of the angular distribution of the electrons in the center-of-mass for this exclusive process:

$$\langle M^2 \rangle \propto 1 + \alpha \cos^2(\theta) , \quad (5.19)$$

where

$$\alpha = \frac{C_1^2 - 2 C_0^2}{C_1^2 + 2 C_0^2} . \quad (5.20)$$

Since we have taken the electrons to be massless, the angular distribution parameter for our exclusive processes is solely dependent upon the manner in which the  $J=1$  charmonium state was produced. If we had produced charmonium by colliding electron beams instead of annihilating protons and antiprotons, the sum over the initial  $e^+e^-$  helicity states would have excluded any production of helicity zero charmonium, and  $\alpha$  would become unity. This has already been confirmed by previous  $e^+e^-$  experiments for both the  $J/\psi$  and  $\psi'$ .<sup>71,72</sup> This parameter is less than one for the case of antiproton-proton annihilation in general because the mass of the proton is much greater than the mass of the electron.

## 5.2. The Angular Distribution Parameter

In exclusive decays, one cannot distinguish whether the electrons came from a charmonium decay, or directly from the continuum channel  $\bar{p} p \rightarrow e^+e^-$ .

Thus the angular distribution parameter  $\alpha$  has a strong contribution resulting from the 3-gluon exchange in the production of charmonium (i.e. the lowest order Feynman graph shown in Figure 5.2), and an electromagnetic contribution resulting from the annihilation of the proton and antiproton into a virtual photon, which may or may not include an intermediate vector charmonium state. Furthermore, another electromagnetic contribution stems from the replacement of one of those 3 gluons by a photon.

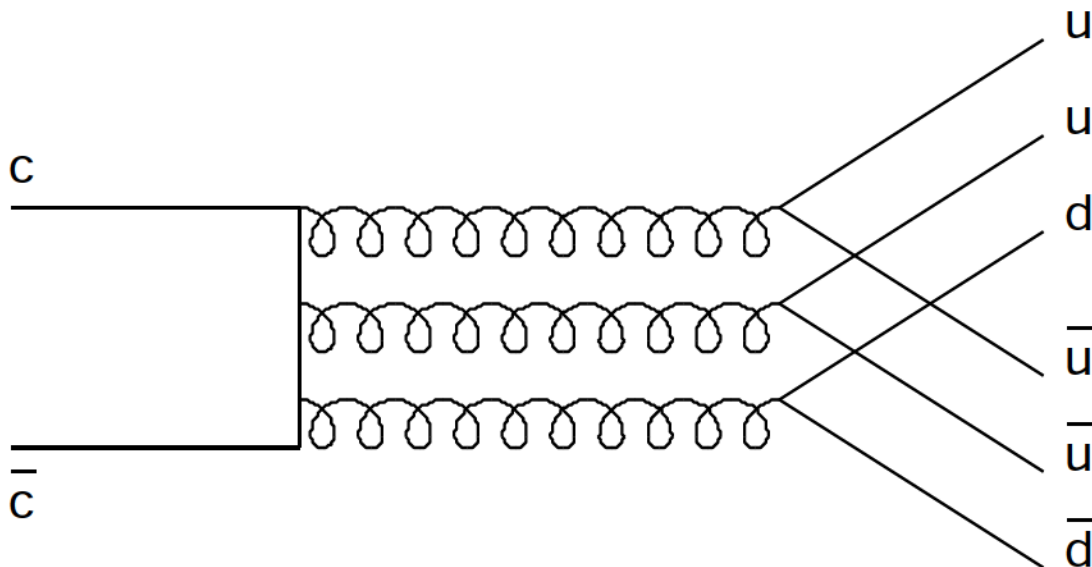


Figure 5.2 : Lowest order Feynman graph for the strong contribution to the angular distribution parameter.

However, measurements of the time-like electromagnetic form factors away from the charmonium region reveal that the cross-section for the continuum channel is negligible at the  $J/\psi$  and  $\psi'$ , on the order of a picobarn.<sup>73</sup>

Furthermore, calculations show that the electromagnetic contributions to the angular distribution parameter are on the order of 5%.

One may also question whether these exclusive decays also receive a contribution from the  $c \bar{c} g$  Fock state (charm quark + anti-charm quark + glue) in addition to the diagram in Figure 5.2. In general, the Fock state representation includes all quantum fluctuations of the hadron wavefunction.<sup>74</sup> In the case of P-wave states, the valence  $c \bar{c}$  state is suppressed in exclusive decays and the  $c \bar{c} g$  Fock state contributes. Fortunately in S-wave exclusive decays like ours the situation is reversed. Higher-order Fock states like  $c \bar{c} g$  are suppressed by factors of the charmed quark mass and velocity.<sup>75</sup>

Usually when one discusses the angular distribution of the continuum channel, one talks about extracting a pair of electromagnetic form factors of the proton. Due to the vector-like nature of the intermediate photon, Lorentz invariance allows the proton-antiproton-photon vertex to be written in the following manner:

$$\bar{v}(p') \gamma^\mu u(p) = e \bar{v}(p') \left[ F_1(Q^2) \gamma^\mu - \frac{(p + p')^\mu}{2M} F_2(Q^2) \right] u(p), \quad (5.21)$$

where  $F_1$  and  $F_2$  refer to the helicity-conserving and helicity-flip parts of this

vertex and are referred to as Dirac form factors. From this one can derive the form of the angular distribution for this process<sup>76</sup>

(5.22)

$$\frac{d\Omega}{d(\cos\theta^*)} = \frac{\Omega^2}{8EP} \left[ |G_M|^2 (1 + \cos^2\theta^*) + \frac{4m_p^2}{s} |G_E|^2 \sin^2\theta^* \right],$$

where E and P are the center-of-mass energy and momentum of the antiproton,  $\theta^*$  is the polar decay angle of the antiproton in the center-of-mass frame, and the Sachs electromagnetic form factors are defined as

$$G_M = F_1 + F_2, \quad (5.23)$$

and

$$G_E = F_1 + \frac{q^2}{4m_p^2} F_2. \quad (5.24)$$

As a result, the angular distribution parameter may be written as

$$\Omega^2 = \frac{E_{CM}^2 - 4 \left| \frac{G_E}{G_M} \right|^2 m_p^2}{E_{CM}^2 + 4 \left| \frac{G_E}{G_M} \right|^2 m_p^2}. \quad (5.25)$$

In the case of charmonium, one can also extract form factors like these from the angular distribution of charmonium decays since both the virtual photon and the spin 1 charmonium state are vector states. However, one cannot call these form factors electromagnetic. These “strong” form factors can

also be evaluated by applying Lorentz invariance at the vertex.

The distinction can be clarified by the derivation of the form factor  $F_1$  by Brodsky and Lepage.<sup>77</sup> They break up the electromagnetic form factor into 3 parts: a) an amplitude  $\bullet$  for finding the three-quark valence state in the incoming proton, b) an amplitude  $T_H$  for this state to scatter with the photon producing 3 quarks with roughly collinear momenta, and c) an amplitude  $\bullet^*$  for this final quark state to form into a hadron:

(5.26)

$$F_1(Q^2) = \int_0^1 [dx] \int_0^1 [dy] \bullet^*(y_i, \tilde{Q}_y) T_H(x_i, y_i, Q) \bullet(x_i, \tilde{Q}_x),$$

where

$$[dx] = dx_1 dx_2 dx_3 \bullet(1 - x_1 - x_2 - x_3) \quad (5.27)$$

and

$$\tilde{Q}_x = \min(x_i Q), \quad (5.28)$$

and  $x$  represents the fraction of the longitudinal momentum taken up by each valence quark.

The formation of charmonium from proton-antiproton annihilation really involves two distinctly different processes<sup>78</sup>: An interaction between the

various quarks and gluons that is primarily perturbative in nature, and a recombination of the quarks into a proton (or breaking up thereof) that is basically non-perturbative.

$T_H$ , the “hard scattering amplitude”, includes diagrams like those in Figure 5.1 with the exchange of gluons. In the electromagnetic case such diagrams refer only to the exchange of the virtual photon. So for any process,  $T_H$  addresses the hard scattering among the gluons and three quarks of the hadron, which can be treated perturbatively.

The “quark distribution amplitude”  $\phi$ , a function of  $Q^2$ , involves soft processes that recombine the produced quarks into hadrons. At charmonium energies, such soft processes are not treatable by perturbative methods in QCD. The distribution amplitude can be thought of as a probability of finding a valence quark in the proton carrying a fraction  $X_i$  of the proton’s momentum and carrying a transverse momentum less than some scale  $Q$ . As a result, these valence quarks may be treated as moving collinearly up to this scale  $Q$ .<sup>79</sup> Furthermore, these amplitudes are independent of the exclusive decay and are related to the total hadronic wave function.

The soft processes responsible for the recombination phase are typically studied via QCD sum rules or lattice calculations. QCD sum rules

allow one to calculate different moments of the distribution amplitudes. For instance the  $(n_1, n_2, n_3)$ -th moment of the proton's distribution amplitude is

$$\int_{x_1, x_2, x_3} \phi(x_1, x_2, x_3, Q^2) x_1^{n_1} x_2^{n_2} x_3^{n_3} dx_1 dx_2 dx_3. \quad (5.29)$$

Perturbative QCD yields a general expression for the distribution amplitude at a very high energy that is an infinite sum of terms with an unknown non-perturbative parameter which is related to these  $(n_1, n_2, n_3)$ -th moments. The different theoretical models for the distribution amplitudes all evaluate as many moments as possible at a given energy, truncate the general perturbative expression, and find the unknown coefficients using QCD sum rules.<sup>80</sup> However, it is not completely determined at this time whether one can apply the general QCD expression or apply such a truncation to  $N$  terms at lower energies.

### 5.3 Comparison of Theoretical Predictions

Brodsky and Lepage<sup>81</sup> predicted that if one neglects the mass of the constituent quarks, then the total hadronic helicity of all the constituent valence quarks is conserved. Furthermore, the angular distribution of  $\phi$  decays into  $p \bar{p}$

must have the same form,  $1 + \cos^2(\theta)$ , that the direct decay of  $e^+e^-$  into  $p\bar{p}$  via a photon has because the  $J/\psi$  is a vector particle like the virtual photon.

One can still favor a spin-one gluon and have a  $\alpha$  that is less than one if one considers various mass effects on the decay. Claudson, Glashow, and Wise took into account the effect of the total baryon mass as a whole and neglected the contribution of the form factor  $F_2$ ,<sup>82</sup>

(5.30)

$$\frac{d\alpha(J/\psi \rightarrow B\bar{B})}{d(\cos\theta)} \propto 1 + \frac{M_{\psi}^2 - 4m_B^2}{M_{\psi}^2 + 4m_B^2} \cos^2\theta,$$

which predicts  $\alpha = 0.463$  for the  $J/\psi$  and  $\alpha = 0.589$  for the  $\psi'$ . Effectively, this derivation neglects the flipping of the constituent quarks' spins in the proton.

Carimalo considered mass effects on the quark level by (a) assigning each constituent quark to have an effective mass of 1/3 the mass of the proton and (b) assuming a nonrelativistic static quark model, in which all quarks share the momentum equally.<sup>83</sup> He derives the angular distribution coefficient as

$$\alpha = \frac{(1 + u)^2 - u(1 + 6u)^2}{(1 + u)^2 + u(1 + 6u)^2}, \quad (5.31)$$

where

$$u = \frac{m_p^2}{M_{\rho}^2}. \quad (5.32)$$

Disregarding the small electromagnetic correction, this results in  $\alpha = .688$  for the  $J/\psi$  and  $\alpha = .802$  for the  $\psi'$ .

At very high energies, the angular distribution parameter should be one, regardless of what kind of exclusive decay occurs, since the energy of the resonance will be much larger than the mass of the proton. At these energies, perturbative QCD reigns. At lower energies, distances between the valence quarks of the proton may become larger. Hence the confinement QCD potential, which is not well modelled perturbatively, comes into play. Furthermore, the masses of the quarks and hadrons, and perhaps an effective mass for the gluon, have an impact as well. Since the mass of the  $\psi$  is lower than the mass of the  $\psi'$ , the angular distribution parameter  $\alpha$  at the  $\psi$  should be lower than  $\alpha$  at the  $\psi'$  for our exclusive decays into  $e^+e^-$ .

The world experimental average<sup>84</sup> of the angular distribution parameter for the  $J/\psi$  prior to 1989 was  $0.63 \pm .08$ . The derivation of Claudson, Glashow, and Wise was able to demonstrate that corrections due to mass effects can be substantial, but it also shows that one cannot neglect the impact of the individual quarks. So of the first three predictions presented so far, a non-relativistic treatment, whereby each of the valence quarks of the proton share the momentum equally, appears to predict the angular distribution parameter at the  $J/\psi$  very well.

More involved calculations of the angular distribution parameter call upon different models for the quark distribution amplitudes, different applications of QCD sum rules discussed in Section 5.2, and various forms of the coupling constant  $\alpha_s$  used in the calculation. The predictions shown in Tables 5.1 and 5.2 reveal that the width from charmonium to  $p\bar{p}$  is also significant. The non-relativistic treatment of Carimalo<sup>83</sup> does not hold up as well under this additional constraint, and it appears that the “heterotic” solution of Stefanis and Bergmann<sup>85</sup> matches both (a) the world average for the angular distribution parameter and (b) the Particle Data Group value for the width  $\Gamma(J/\psi \rightarrow p\bar{p})$  of 188 eV.

Also presented in Table 5.2 are the respective theoretical expectations<sup>86</sup>

for the angular distribution parameter at the  $\sqrt{s}$  and the respective decay widths to  $p\bar{p}$ . The same models which predict this parameter and the  $p\bar{p}$  decay width<sup>87</sup> at the  $\sqrt{s}$  are used to predict it at the  $\sqrt{s}$ . According to the Particle Data Group the value of the decay width to  $p\bar{p}$  is 53 eV at the  $\sqrt{s}$ .

DA Model	$\alpha$	$\Gamma(J/\psi \rightarrow \bar{p} p)$ (eV)
Brodsky and Lepage <sup>81</sup>	1	-
Claudson, Glashow, and Wise <sup>82</sup>	0.46	-
Carimalo(Non-relativistic) <sup>83</sup>	0.688	0.2
Asymptotic <sup>78</sup>	0.667	2.6
Chernyak and Zhitnitsky <sup>88</sup>	0.561	58.7
Chernyak, Oglobin, and Zhitnitsky <sup>89</sup>	0.565	82.6
King and Sachrajda <sup>90</sup>	0.591	125.5
Gari and Stefanis <sup>91</sup>	0.963	16.8
Stefanis and Bergmann (heterotic) <sup>85</sup>	0.689	167.1

Table 5.1 : Theoretical Predictions of the angular distribution parameter and partial width to  $\bar{p} p$  at the  $J/\psi$ .

DA Model	$\alpha$	$\sqrt{s} \rightarrow p \bar{p}$ (eV)
Brodsky and Lepage <sup>81</sup>	1	-
Claudson, Glashow, and Wise <sup>82</sup>	0.59	-
Carimalo(Non-relativistic) <sup>83</sup>	0.802	0.02
Asymptotic <sup>78</sup>	0.782	0.21
Chernyak and Zhitnitsky <sup>88</sup>	0.683	5.47
Chernyak, Oglobin, and Zhitnitsky <sup>89</sup>	0.687	6.66
King and Sachrajda <sup>90</sup>	0.712	10.31
Gari and Stefanis <sup>91</sup>	0.986	1.07
Stefanis and Bergmann <sup>85</sup> (heterotic)	0.790	14.00

Table 5.2 : Theoretical Predictions of the angular distribution parameter and  $\sqrt{s}$  at the  $\alpha$ .

## 6. Analysis

### 6.1. Electron-Positron Pair Selection.

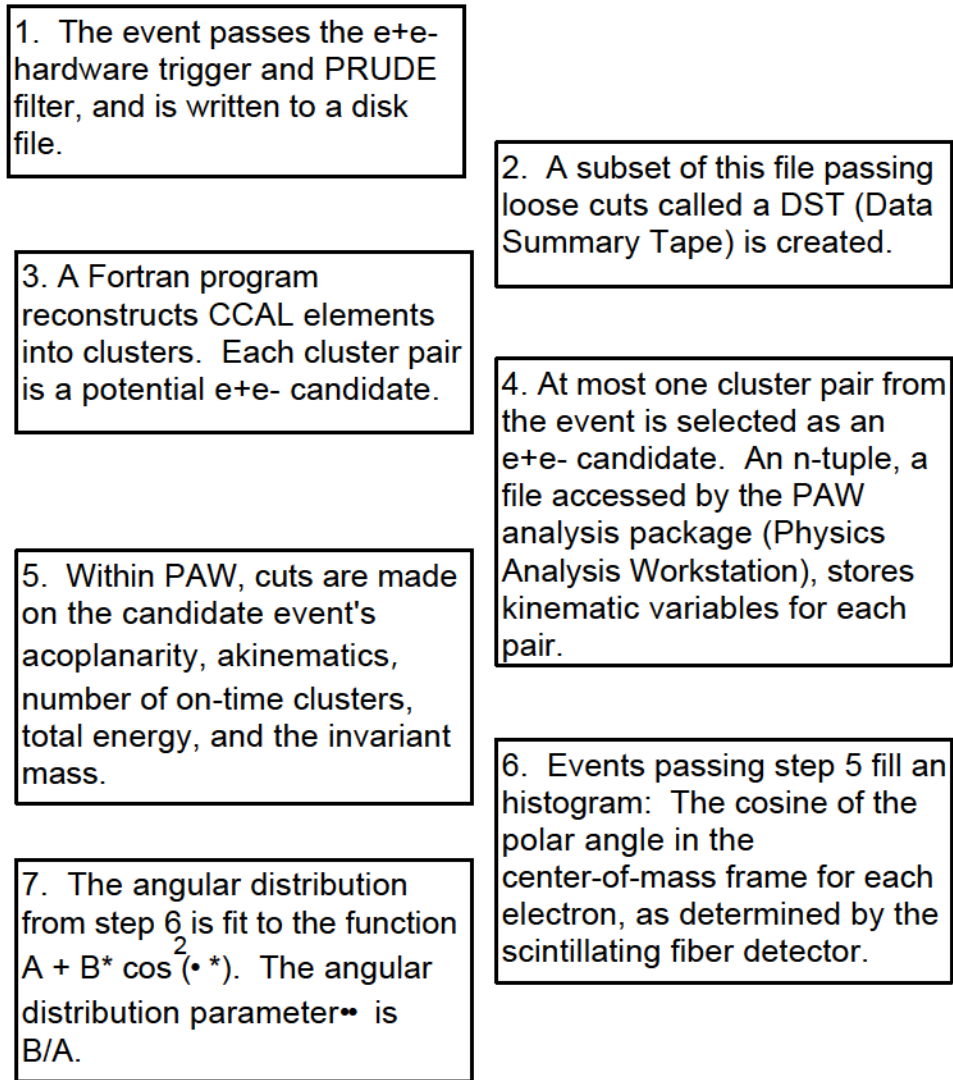


Figure 6.1 : Data Analysis Flow Chart.

The sequence of selections on electron-positron candidate events is shown schematically in Figure 6.1. Initially (Step 1, Figure 6.1), events that pass the hardware  $e^+e^-$  trigger are reconstructed by the PRUDE filter and written

to disk. From these resident disk files, loose cuts are applied (Step 2, Figure 6.1) in order to produce a DST file (Data Summary Tape), also residing on disk. A DST contains a subset of all the events in the disk file that do not include the large hadronic background present below 2.7 GeV. The event is rejected if (a) the event did not fire Gatemaster bit 1 (the  $e^+e^-$  trigger), (b) the number of clusters seen by the central calorimeter is greater than 20, or (c) the largest possible invariant pair mass (on-time or out-of-time) constructed from a cluster pair is less than 2.7 GeV, as determined from the energy deposits and angles given by the central calorimeter. All possible combinations of cluster pairs are considered, except when one of the clusters (a) is not on-time with respect to the  $e^+e^-$  trigger, or (b) does not exceed a minimum cluster energy of 200 MeV .

When a particle such as an electron enters the CCAL, it creates an electromagnetic shower which produces Cerenkov light in several neighboring lead glass blocks. The amount of Cerenkov light is proportional to the amount of energy deposited in each block. A software program called the clusterizer searches for possible "seed" blocks, around which the energy deposits are grouped into clusters (Step 3, Figure 6.1). A cluster is the CCAL's representation of the particle that entered it. For this analysis, cluster thresholds were set at 5 MeV for the seed block of the cluster, and 20 MeV for the surrounding 3-by-3 grid. A cluster pair is defined to be "on-time" if the TDC values (which flag the cluster creation with respect to the time the interaction occurred) of its largest energy deposits are on-time.

From the smaller DST file, further cuts are applied to the data to establish the thesis sample (Step 4, Figure 6.1) and event information is written to an n-tuple, a file that stores processed information for future use within PAW (the Physics Analysis Workstation analysis package). A typical n-tuple may hold the values of 35 to 50 kinematic variables per event. If an on-time cluster pair generates an invariant mass closest to the resonance in question, and said invariant mass is greater than 2.7 GeV, then that cluster pair is chosen to be the  $e^+e^-$  candidate from the event. There is no way to tell in this experiment which cluster is the positron and which is the electron.

At this juncture the thesis sample is refined using the PAW analysis package (Step 5, Figure 6.1). Many different analysis cuts, like those discussed later in Section 6.3 to determine the thesis sample, can be made. For example, suppose one wants to plot the invariant mass of all the events in the n-tuple with only 2 on-time clusters. Kumac files may include a large list of commands like those below, and allow Fortran programs to be called from within PAW to analyze the data. The general procedure is as follows:

```
> pawX11                                ! Launch the PAW software
                                           ! package.
>hi/file 1 /scratchj/mctaggar/jpsi.ntp    ! Load the desired n-tuple.
```

>ntuple/plot 20.s12 ontime.eq.2

! Display an histogram of the  
! invariant mass (s12) of all  
! events whose value  
! of "ontime" is 2.

After the final thesis sample has been ascertained, one may plot the angular distribution in an histogram (Step 6, Figure 6.1), and fit this histogram to obtain the angular distribution parameter\*\* (Step 7, Figure 6.1). The details of the fit will be presented in Chapter 7: The remainder of Chapter 6 focuses on the selection of the thesis sample. Section 6.2 determines which polar angle information is included in the angular distribution histogram. In Section 6.3 the analysis cuts are fully detailed, and finally in Sections 6.4 and 6.5 any background contamination remaining in the sample and possible bias with the hardware trigger are discussed respectively.

## 6.2. Polar Angle from Fibers and CCAL.

In the experiment there are several ways to define the polar angles of the  $e^+e^-$  pair. Primarily one may use either the information given by the scintillating fiber tracker,<sup>92</sup> that given by the central calorimeter, or some combination of the two. The CCAL has the advantage of yielding the particle's energy, azimuth and polar angle in the lab. In fact the  $e^+e^-$  pair is chosen with these 3 variables

and whether the CCAL clusters are on-time. However, due to the finer resolution of the fibers and the behavior of the CCAL clusterizer, the angle that is included in the final angular distribution comes from the scintillating fibers associated with the CCAL cluster and not directly from the CCAL cluster itself. Furthermore, no combination of the two angles are attempted either.

In reconstructing final  $e^+e^-$  states, the present offline clusterizer has a preference for centering clusters across the face of a calorimeter block: Away from block centers and toward the block edges. This does not result in a smooth angular distribution of the  $e^+e^-$  in  $\cos(\theta^*)$ . The primary reason for this behavior is that the resolution of the calorimeter is better near the edges of the blocks (where 2 photomultiplier tubes can see the event) than at the center (where only one will receive the energy deposit).

The clusterizer is also better equipped to handle the 2 photon decays of resonances like the  $\rho_2$  or the  $\rho_c$  than the  $e^+e^-$  decays studied here. Its algorithms search for energy deposits to group into clusters, and along with the  $e^+e^-$  in the event may come delta rays from the interaction of the electrons with the detectors. The position of the cluster can be affected by these delta rays that get absorbed in the clusterizing process.

The result is an unnaturally high chi-square per degree of freedom for the

angular distribution, which is not related to whether both electrons are contained within the geometrical acceptance of the CCAL. This oscillation of CCAL angular distributions about the fit curve, which repeats after every CCAL block, is easily seen in Figure 6.2. Using only the CCAL information, the chi-square per degree of freedom for the final angular distribution of this thesis would be over 2.0 (the nominal value is 1.0 per degree of freedom).

The CCAL shower Monte Carlo<sup>93</sup> for e835 attempts to describe the general behavior of the lead-glass calorimeter blocks in response to photons and electrons passing through it by integrating over the shower shape instead of producing secondary showering particles as the GEANT version does, but once fully tuned it will deliver a very fast estimation of the response of the calorimeter with many thousands of events. In principle a fully-tuned Monte Carlo (either kind) will correct angular distributions like those found in Figure 6.2 when it can replicate qualities such as acoplanarity, akinematics, where the electron hits a CCAL block across the block face, and bring the chi-square of the final fit to near 1.0 per degree of freedom. However, it was decided for this thesis that the present form of the CCAL shower Monte Carlo and the current set of tuning parameters did not satisfy all of these requirements.

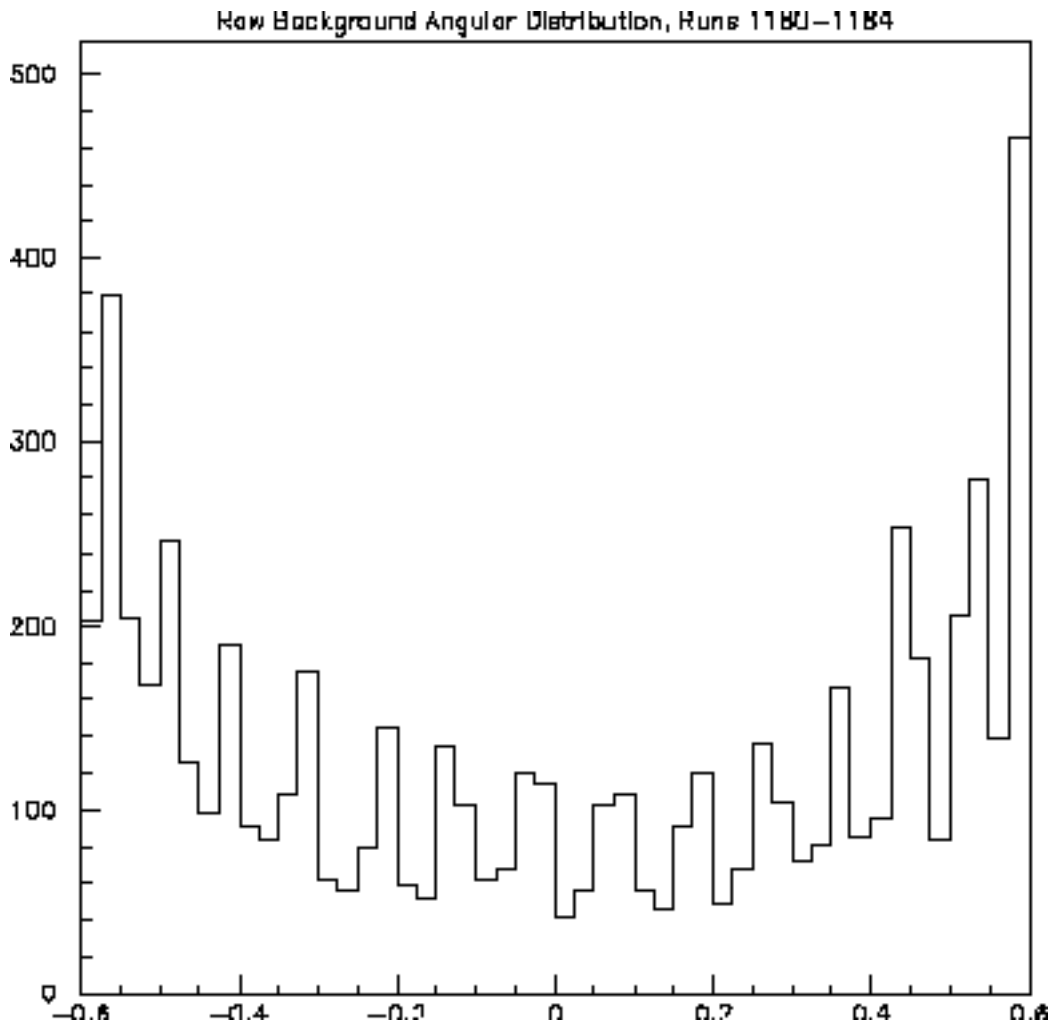


Figure 6.2: Behavior of the CCAL Clusterizer: Raw Angular Distribution of Background Runs 1180-1184.

Angular distributions using the scintillating fibers do not suffer from this repetitive behavior seen in the CCAL distributions because the fibers are physically finer than the face of a CCAL block (~1 mrad<sup>92</sup> vs. ~10 mrad<sup>44</sup>). However, the fiber angular distribution is not completely independent of the corresponding CCAL distribution. Fiber hits are associated with particular

CCAL clusters in the process of fitting all the detector elements for charged and neutral tracks. Basically the fiber hits that have the minimum opening angle with respect to a particular CCAL cluster share the same track as that CCAL cluster, but other statistical aspects of the fitting procedure also come into play.

One way to make an independent fiber angular distribution is to choose events that have the minimum acinematics. However, this does not make any demands on the acoplanarity, invariant mass, nor total energy of the event. These are not available from the fibers. Furthermore, the fibers are not 100% efficient: For each  $e^+e^-$  pair that passes the analysis cuts (discussed in the next section), there may be 0, 1, or 2 associated fiber tracks. Acinematics from fiber information for a valid  $e^+e^-$  pair can only be determined if there are 2 fiber hits per pair.

In this analysis the polar angle is determined from the Z-coordinates of the inner and outer fiber layers. Given the radius of the fiber layer is known, the polar angle in the lab frame can be calculated. If both layers register a hit, the polar angle is taken as the average of the two. Assuming the associated CCAL clusters pass all the analysis cuts, then 0, 1, or 2 entries are made into the histogram for the final angular distribution. This depends upon whether (a) the fiber tracking detector registers and (b) the track is within the fitting region. For the  $J/\psi$ , the fit is applied to the region  $-.45 < \cos(\theta^*) < .45$ , which

corresponds in the lab frame to  $23.5^\circ < \theta < 57.5^\circ$ . For the  $\pi^+$ , the fitting region is  $0.525 < \cos(\theta) < .525$ , which corresponds in the lab frame to  $17.3^\circ < \theta < 52.3^\circ$ . One result of these choices is that the forward calorimeter is not used in this analysis, since it lies below 15 degrees. This also removes background candidates, since the multi-pion channel is forward-peaked.

The efficiency of the scintillating fiber detector for seeing a track is shown in Figure 6.3. This also includes the geometrical factors shown in Figure 6.4, and effects like dead channels. Although the efficiency of the fibers affects the  $J/\psi$  angular distribution more, this efficiency is always over 92% for the  $J/\psi$  fit, and over 96% for the  $\pi^+$  fit.

The effect of selecting the polar angle from the scintillating fiber tracker instead of the CCAL on the size of the thesis sample is apparent in Table 6.1. The differences in the event counts (near 1% for both channels) are either due to migration across the fit boundaries when one chooses the fiber polar angle over the CCAL polar angle (or vice-versa), a failure to associate a fiber hit to the correct cluster, or the inefficiency of the fibers. Since both members of the  $e^+e^-$  pair are always contained within the geometry of the detector, and the efficiency of the scintillating fibers is close to one, no correction by Monte Carlo is made to the angular distribution of either decay channel.

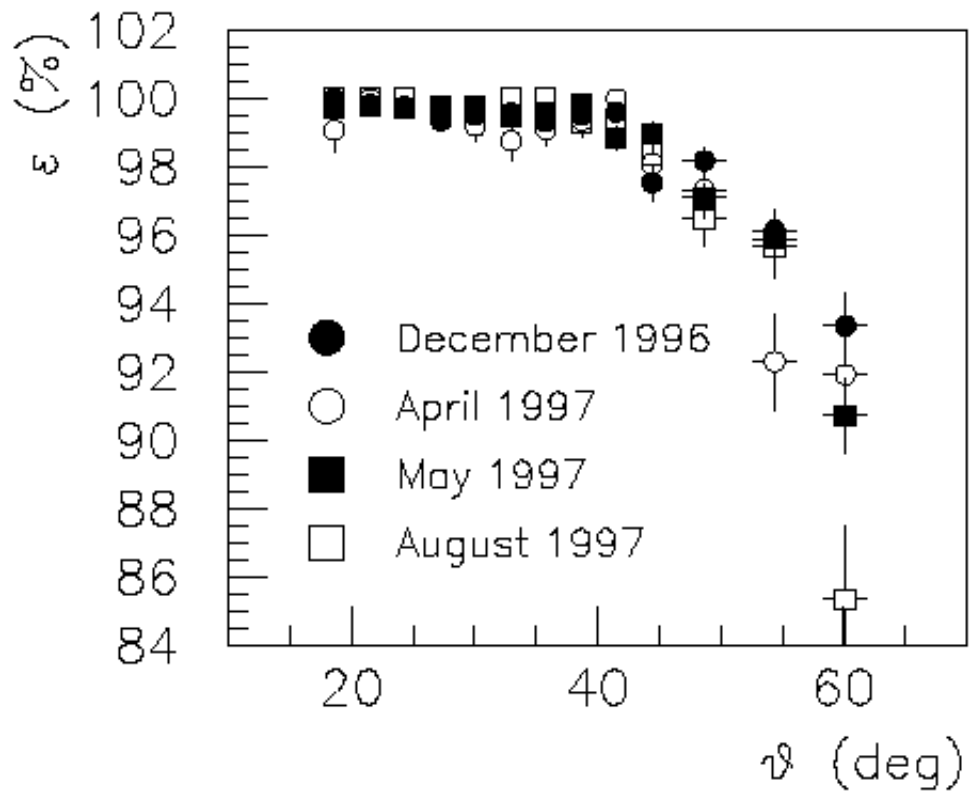


Figure 6.3: Detection efficiency of the scintillating fiber tracker.<sup>92</sup>

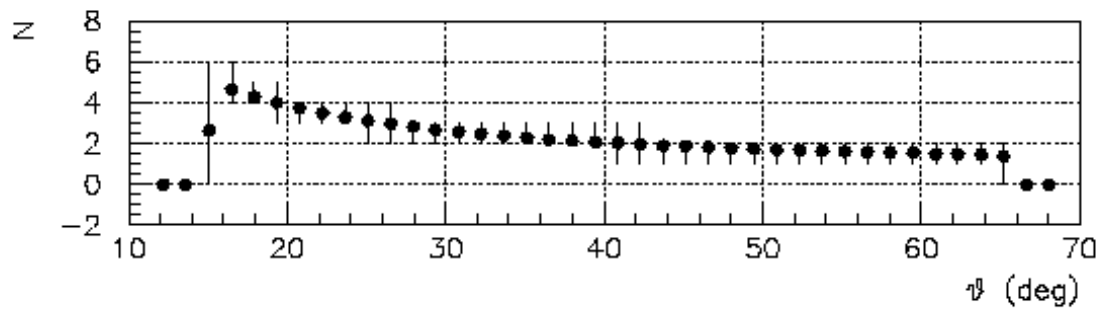


Figure 6.4: Number of fibers hit as a function of polar lab angle.<sup>92</sup>

Run Number	Number of Entries, CCAL	Number of Entries, Scintillating Fiber
908-909	8,244	8,199
3078-3079	2,447	2,419
J/ψ Total	10,691	10,618
877-882	205	207
1006-1018	202	200
1276-1281	532	508
2003-2018	523	524
2218-2253	794	790
3210-3233	461	457
ψ Total	2,717	2,686

Table 6.1: Number of entries in the final angular distribution when the polar angle is determined from either the CCAL or the scintillating fiber tracker.

Deciding which events contribute to the angular distribution, and therefore to Table 6.1, is the subject of the following section.

### 6.3. Thesis Sample Selection.

To obtain the angular distribution of the final  $e^+e^-$  state, several cuts are applied to the data. The purpose of each cut is to remove events that may simulate an  $e^+e^-$  pair decaying from charmonium, but instead arise from the background continuum or multi-pion decays. If the candidate pair from the event passes the following cuts in Table 6.2, and the scintillating fiber tracker

yields a polar angle that falls within the fitting region mentioned in Section 6.2, the event may contribute 0, 1, or 2 entries to the final angular distribution.

Otherwise the event is not considered.

1.	2 on-time clusters.
2.	Invariant mass > 2.7 GeV, ( $J/\psi$ ) Invariant mass > 3.4 GeV, ( $\psi'$ )
3.	Acoplanarity between -25 milliradians and +25 milliradians.
4.	Akinematics between -25 milliradians and +25 milliradians
5.	4.71 GeV < ETOT < 5.31 GeV ( $J/\psi$ ) 6.72 GeV < ETOT < 7.62 GeV ( $\psi'$ )

Table 6.2: Summary of analysis cuts based on CCAL information.

The purpose of this section is to evaluate how the distribution of each of the five variables above is affected by the other cuts, and justify why these cuts were made. However, one should not count the number of events in the following distributions in this section to achieve a final event count, since the fiducial lab angle cuts of Section 6.2 made prior to fitting are not applied to the following plots. As a result the data passing all these cuts will provide at most 2 entries to the angular distribution, but only 1 entry in the following plots. Events

that provide 0 or 1 entries to the angular distribution are still plotted here, and are present when the width of the total energy distribution is determined. Events that fail any of these cuts always contribute zero entries to the angular distribution.

In Appendices A and B the efficiencies of all possible combinations of cuts in Table 6.2 above are listed for each subset of the  $J/\psi$  and the  $\psi'$  data. In this case, fiducial lab angle cuts are performed before calculating the efficiencies of the analysis cuts. The efficiency is defined here as the number of electrons passing all cuts (and included in the fit) divided by the number of electrons achieved by that combination of cuts (and included in the fit). Therefore a set of cuts is 100% efficient if it produces the final data sample. For the  $\psi'$  the efficiencies are generally lower for one or two of the above cuts than similar cuts on the  $J/\psi$ , due to the  $J/\psi \rightarrow e^+e^-$  decay of the  $\psi'$ . Combinations of cuts that include an invariant mass cut of 3.4 GeV have higher efficiencies, since they remove  $e^+e^-$  pairs that originate from the  $J/\psi$ .

The first of the analysis cuts is that the event must have only 2 on-time clusters. However, this cut by itself does not prohibit the event from having several out-of-time clusters in addition to these two. Figure 6.5 for the  $J/\psi$  and Figure 6.6 for the  $\psi'$  show how the number of on-time clusters in the sample

changes before any cuts are applied and after all other cuts are made. The extra clusters in the  $\psi'$  distribution at the top of Figure 6.6 are due to the (a) the inclusive decay of the  $\psi'$  to the  $J/\psi$ , (b) multi-pion decays that accompany charmonium production, and to a lesser extent (c) the  $e^+e^-$  continuum (i.e.  $p\bar{p} \rightarrow e^+e^-$ ). Their influence on the study of these exclusive decays of charmonium are better understood by studying the invariant mass of the sample. Nevertheless, this particular cut is critical in removing these unwanted events.

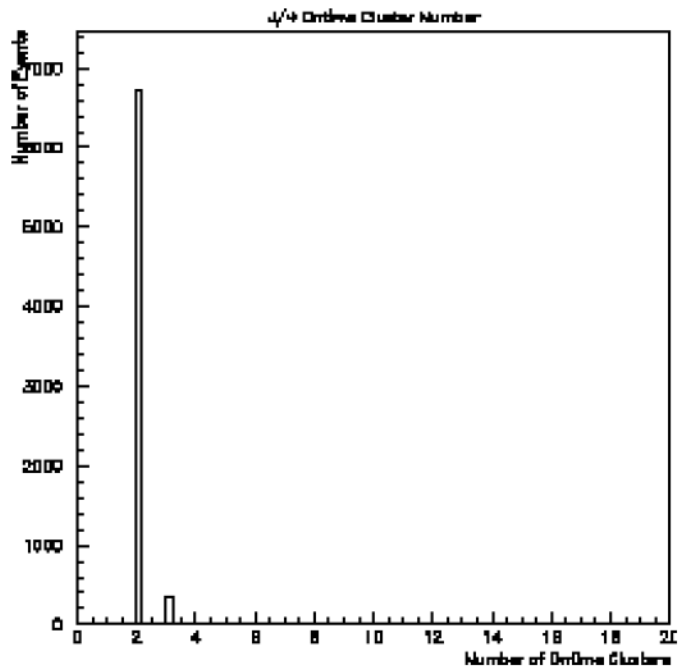
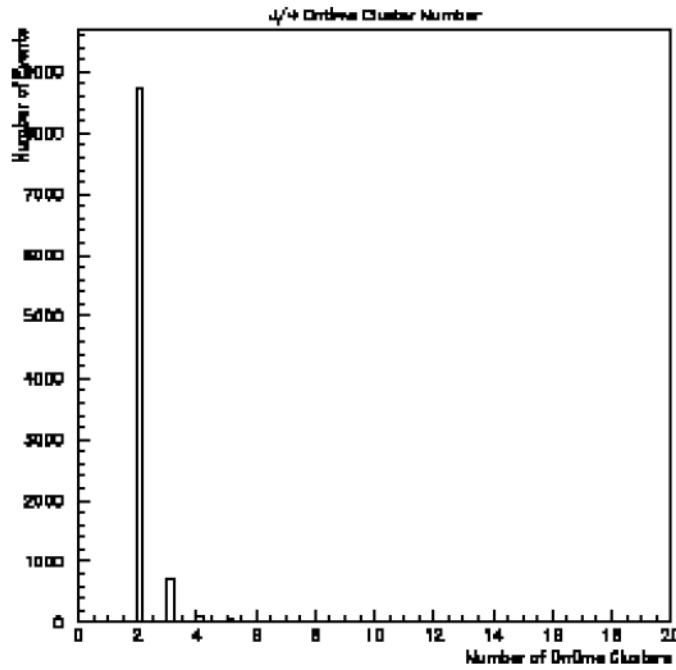


Figure 6.5:  $J/\psi$  On-time Cluster Number before any cuts are made (top) and after all other cuts are applied (bottom). Only events with 2 on-time clusters remain in the thesis sample.

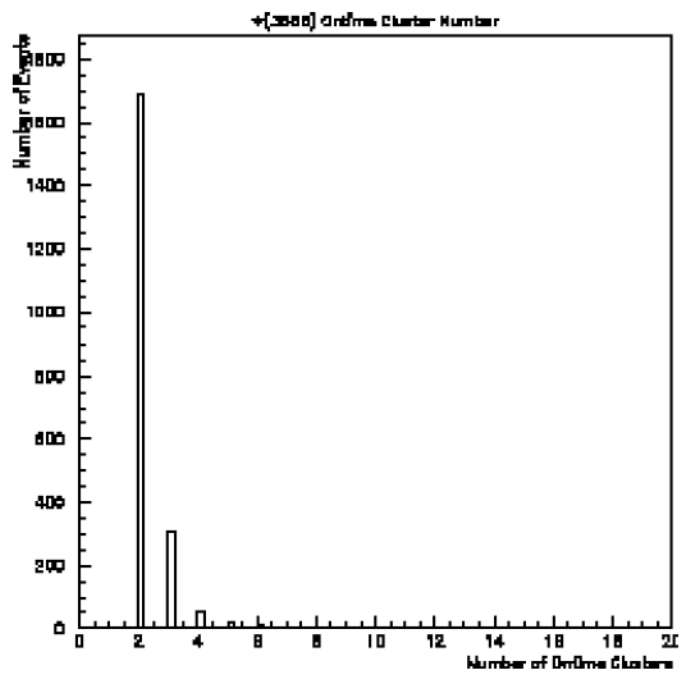
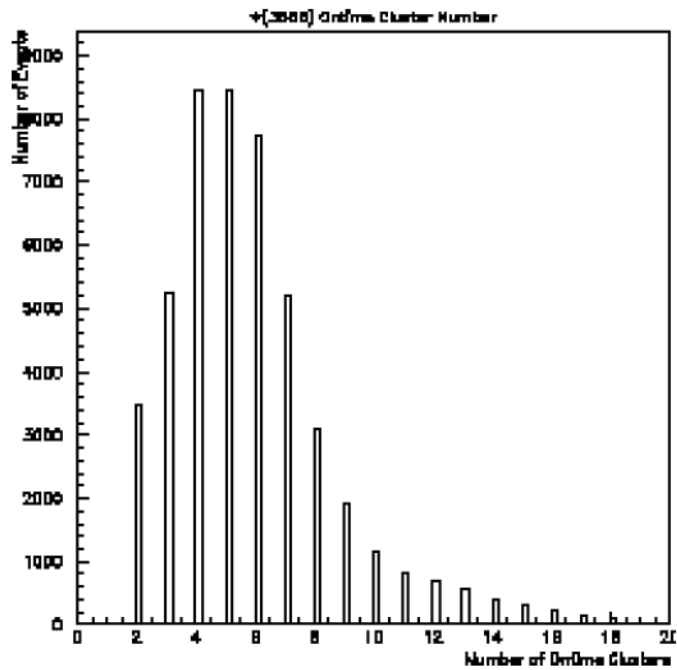


Figure 6.6: • (3686) On-time Cluster Number distributions before any cuts (top) and after all other cuts (bottom) are applied. Only events with 2 on-time clusters remain in the thesis sample.

The invariant mass distributions of the  $J/\psi$  are shown in Figure 6.7 before any cuts are made and after all of the other cuts have been applied. Cluster pairs included in the final  $J/\psi$  sample must have an invariant mass greater than 2.7 GeV. Recall that to be written to the n-tuple, the event must have two clusters with an invariant mass greater than 2.7 GeV (i.e. neither cluster has to be on-time). The  $e^+e^-$  pair is chosen as the on-time cluster closest to the resonance in question with respect to the invariant mass, so there are some  $e^+e^-$  pairs with invariant masses less than 2.7 GeV in the n-tuple.

Primarily there are two reasons why the  $J/\psi$  exclusive decay is easier to study than the  $\psi'$ . First, the cross-section for producing exclusive decays falls as  $\frac{1}{Q^2}$ , so this channel is more prominent at the  $J/\psi$ . Also, the resonance below the  $J/\psi$ , the  $\psi_c$ , is not allowed to decay to  $e^+e^-$  by parity, so this additional inclusive channel is not seen in Figure 6.7 as it is in Figure 6.8.

Clearly evident in the top of Figure 6.8 are the two background sources for the  $\psi'$  exclusive decay to an  $e^+e^-$  pair before any cuts are made: Contamination from the multi-pion decays (the large exponential curve), and the decays of the  $\psi'$  to  $J/\psi + X$ , where X may be either  $2\pi$  or simply an  $\pi$ . In the

latter case an  $e^+e^-$  pair arises from the cascading decay of the  $J/\psi$  instead of the exclusive decay of the  $\psi'$ , which results in the enhancement around 3.1 GeV. The exclusive channel remains under the Gaussian centered near 3.6 GeV. At the bottom of Figure 6.8 an invariant mass cut of 3.4 GeV assures that these two sources have little impact on the exclusive decay channel. The distributions shown at the bottom of Figures 6.7 and 6.8 demonstrate the mass resolution of the central calorimeter.

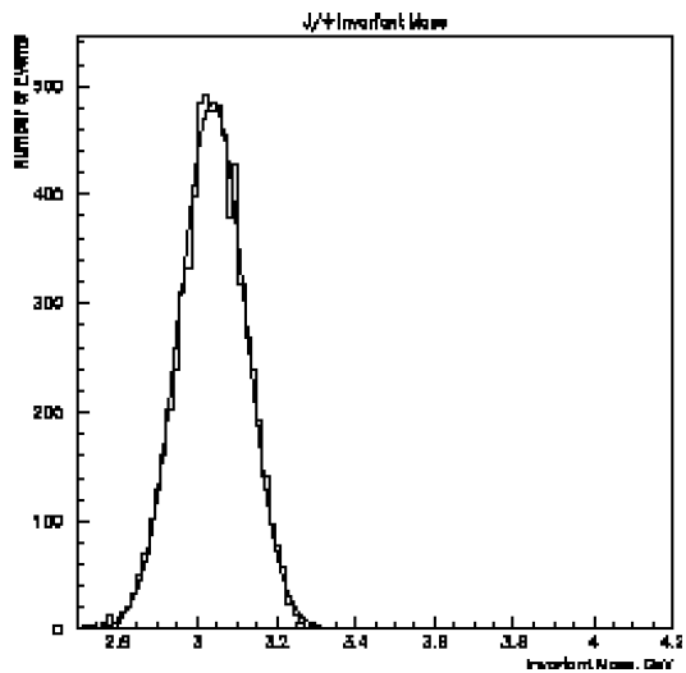
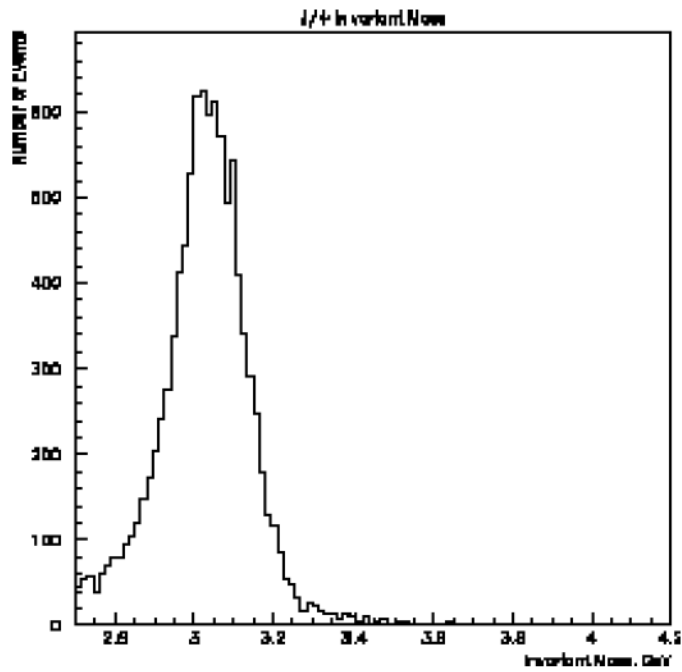


Figure 6.7:  $J/\psi$  Invariant Mass distributions before any analysis cuts (top) and after all other analysis cuts (bottom).

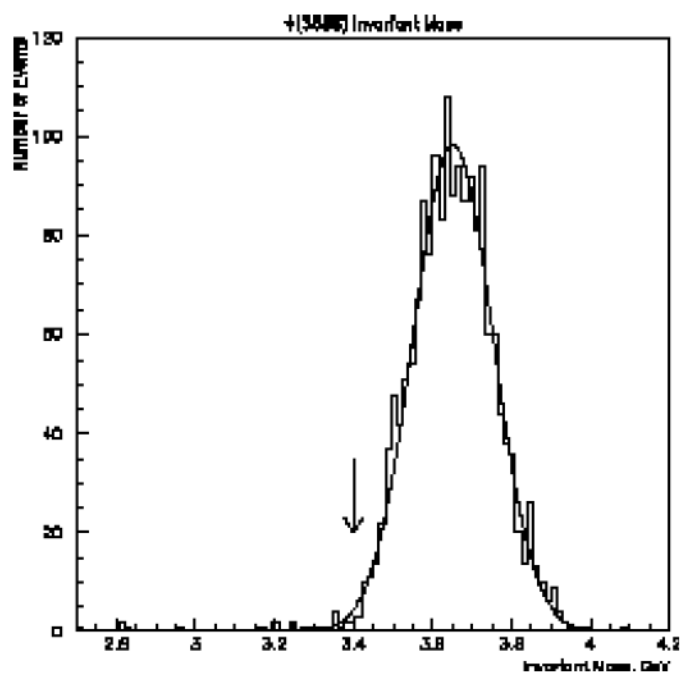
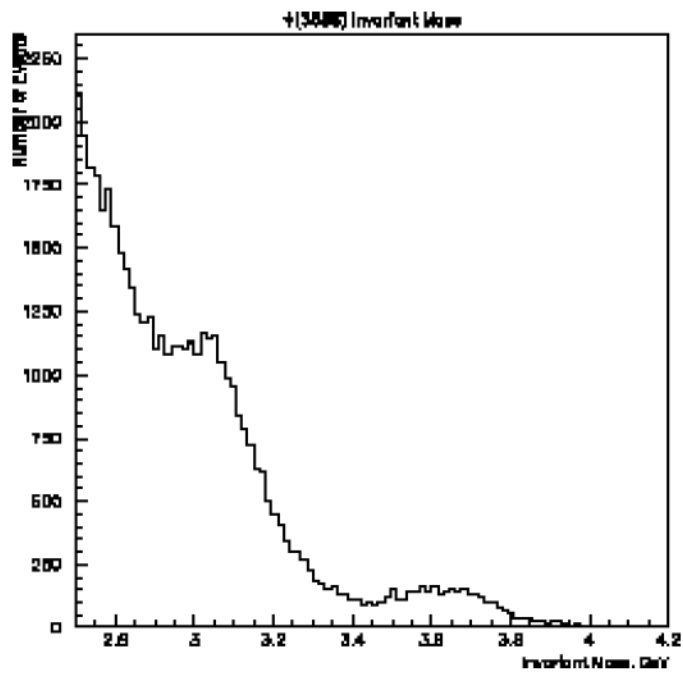


Figure 6.8: • (3686) Invariant Mass distributions before any cuts (top) and after all other cuts are applied (bottom).

Next, events are removed if their acoplanarity and akinematics are too large. These two quantities are evaluated using the CCAL polar angles instead of those given by the scintillating fibers, since CCAL cluster formation is the primary factor in selecting tracks. In the center-of-mass frame, the electrons from an exclusive charmonium decay should come out back-to-back. Zero acoplanarity means the event is exactly back-to-back in terms of the azimuthal angle. Zero akinematics means the event is perfectly back-to-back in terms of the center-of-mass polar angle. In practice, both quantities have a distribution centered on zero for pure  $e^+e^-$  events due to the resolution of the central calorimeter. If the acoplanarity or akinematics is greater than 25 milliradians, the event does not contribute to the angular distribution of either resonance's exclusive decay.

In Figures 6.9 and 6.10 are shown the acoplanarity and akinematics distributions for the  $J/\psi$  respectively (before any cuts and after all other cuts). The corresponding distributions are presented in Figure 6.11 and Figure 6.12 for the  $\psi'$ . As seen previously in the invariant mass plots, the  $J/\psi$  sample is much cleaner than the  $\psi'$  sample to begin with, and the other cuts do a good job in cleaning up both decay channels.

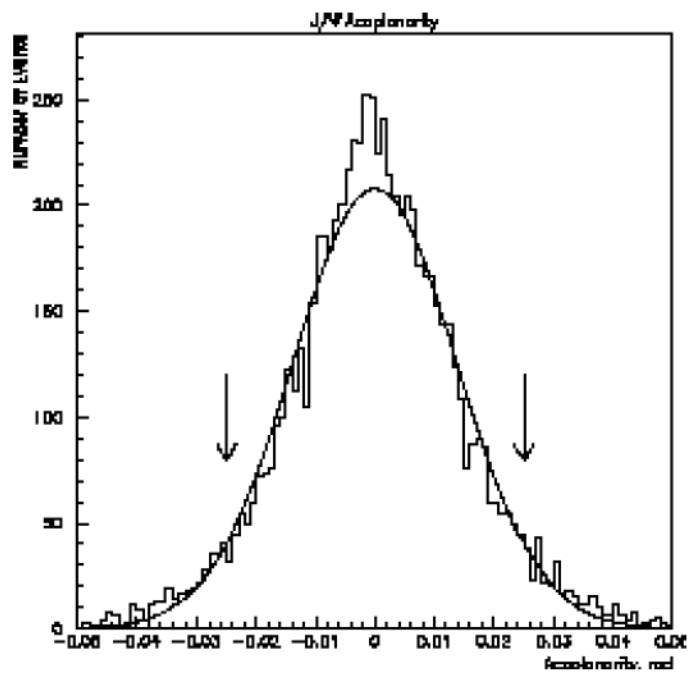
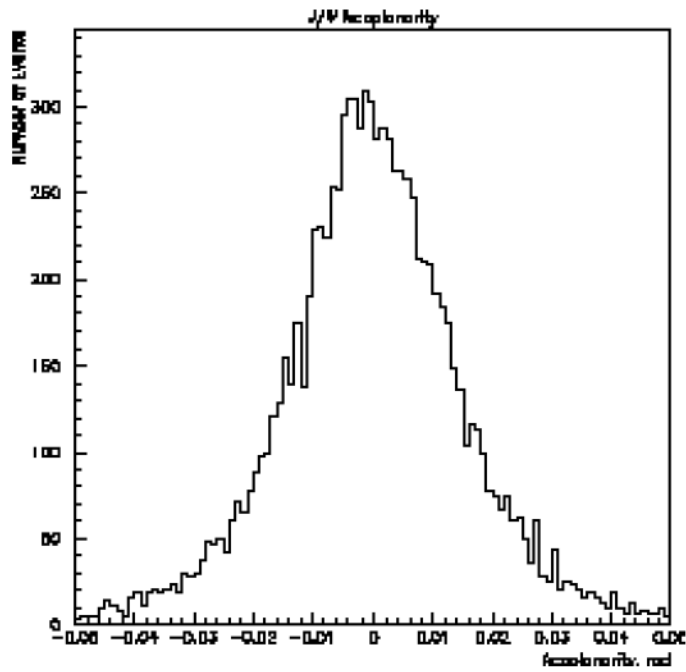


Figure 6.9:  $J/\psi$  Acoplanarity distributions before any cuts (top) and after all other cuts (bottom) are applied. Arrows represent the cut made on Acoplanarity.

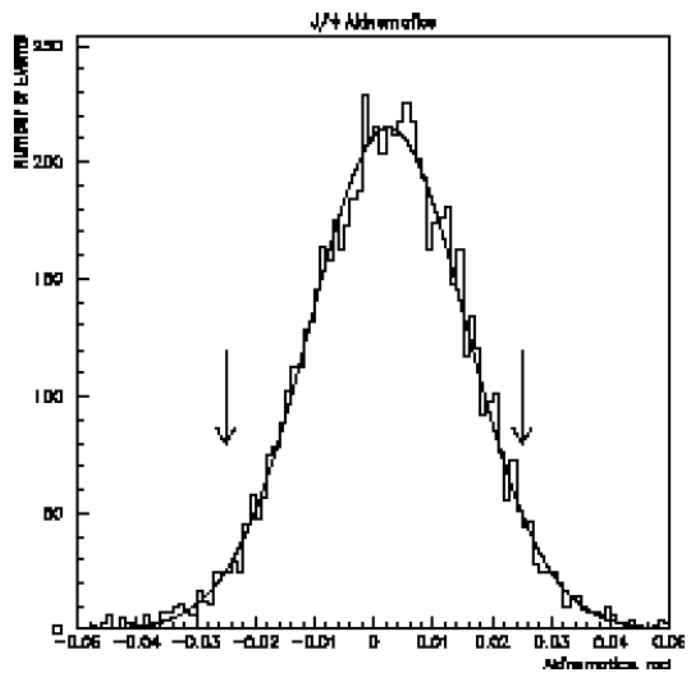
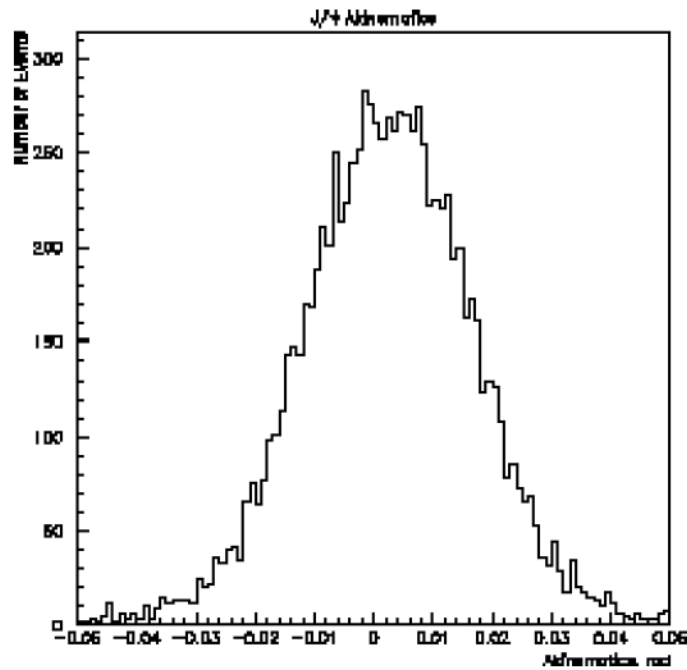


Figure 6.10:  $J/\psi$  Akinematics distributions before any cuts (top) and after all other cuts (bottom) are applied. Arrows represent the cut made on Akinematics.

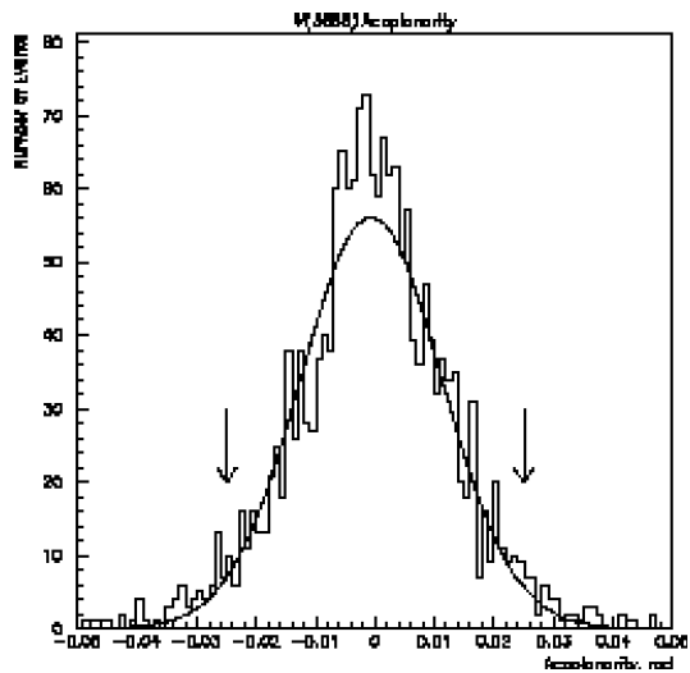
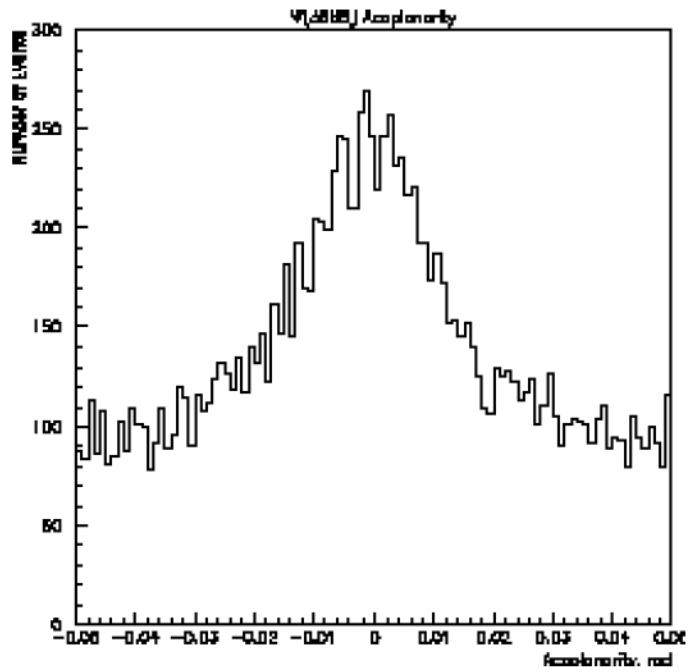


Figure 6.11: • (3686) Acoplanarity distributions before any cuts (top), and after all other cuts (bottom) are applied. Arrows represent the cut made on Acoplanarity.

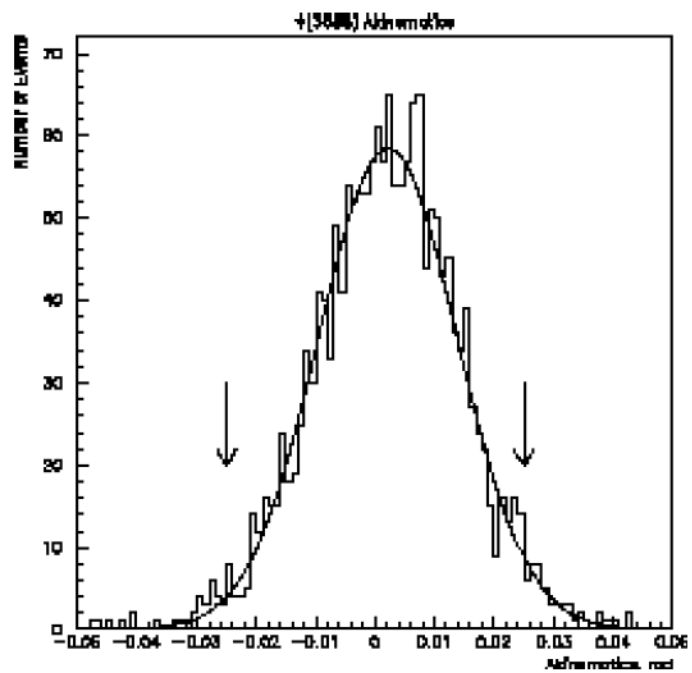
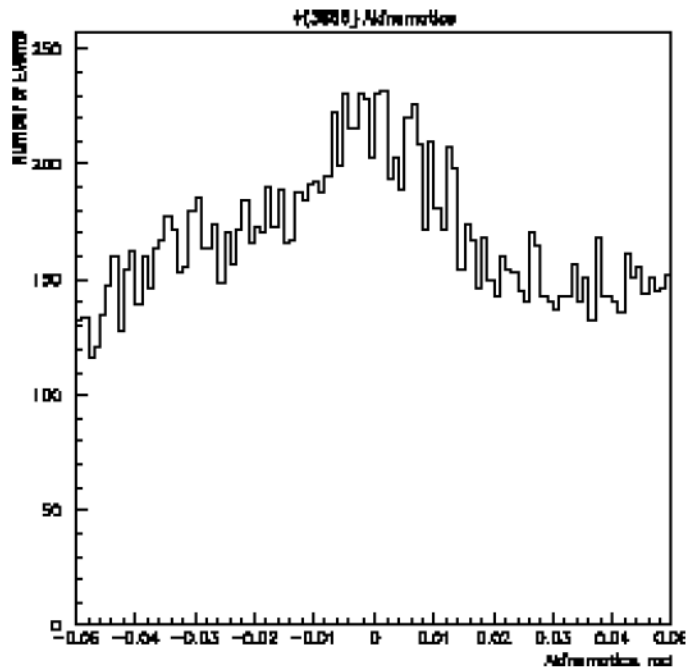


Figure 6.12: • (3686) Akinematics distributions before any cuts (top) and after all other cuts (bottom). Arrows represent the cut made on Akinematics.

Finally, a cut is made on the total energy of the  $e^+e^-$  pair. After all other cuts in Table 6.2 have been applied, a Gaussian is fit to the bottom of Figures 6.13 for the  $J/\psi$  and 6.14 for the  $\psi'$ . Events that lie outside the mean total energy  $\pm 2\sigma$  are cut, which results in  $4.71 \text{ GeV} < ETOT < 5.31 \text{ GeV}$  for Figure 6.13, and  $6.72 \text{ GeV} < ETOT < 7.62 \text{ GeV}$  for Figure 6.14.

The end results of all these cuts are two very clean samples from which to study exclusive decays of charmonium to  $e^+e^-$  pairs. Furthermore, to underscore this point, the efficiencies of the various cuts in Appendices A and B are consistent among the various data sets included. But before presenting the final angular distributions, we must first estimate how much of the background was not excluded by the analysis cuts, and address the possibility of any bias in the electron trigger (which is used to flag and write the data to tape).

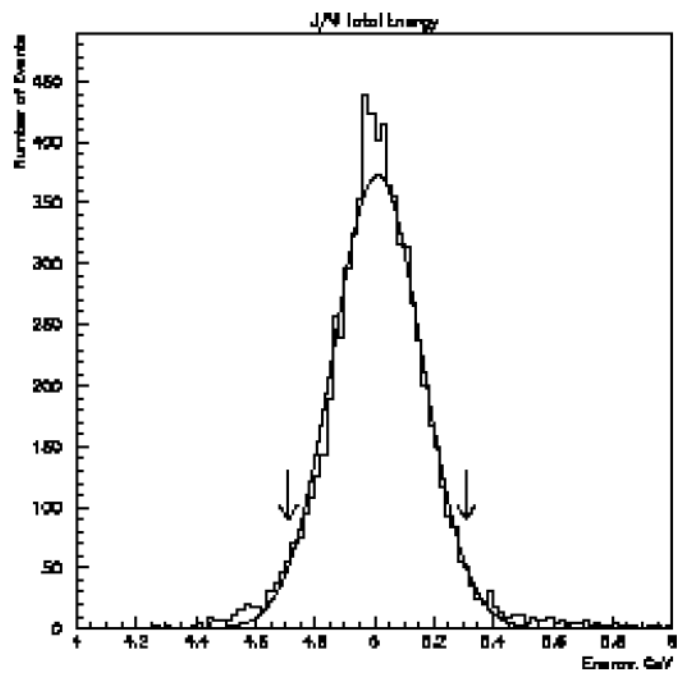
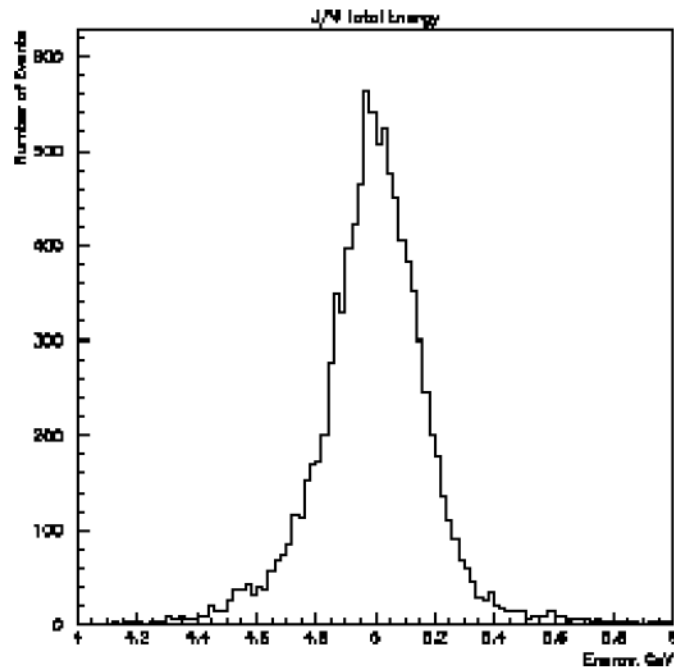


Figure 6.13:  $J/\psi$  Total Energy distributions before any cuts (above), and after all other cuts (bottom) are applied. Arrows show where the Total Energy cut is made to the sample.

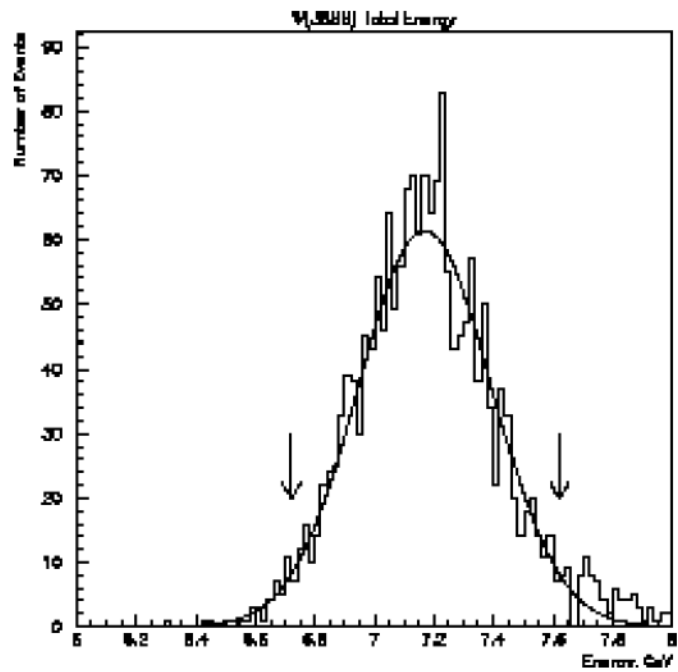
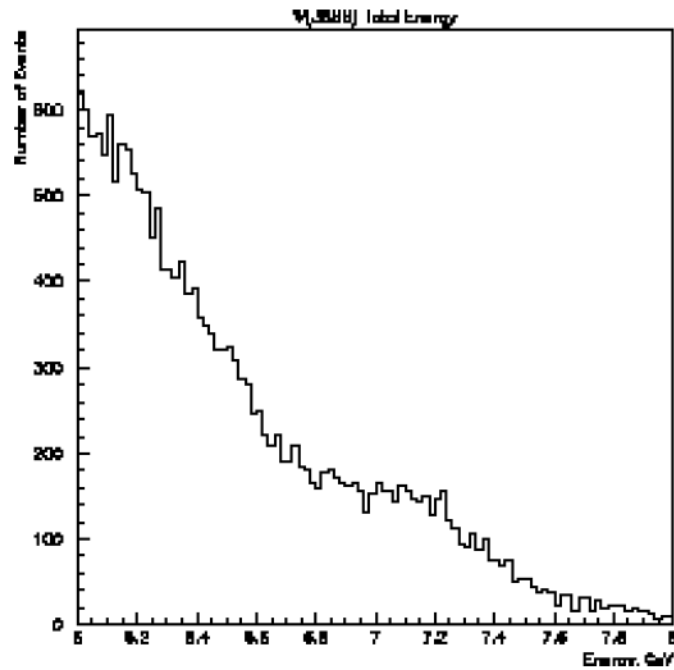


Figure 6.14: • (3686) Total Energy distribution before any cuts (top) and after all other cuts (bottom) are applied. Arrows show where the Total Energy cut is made to the sample.

## 6.4. Background to the Thesis Sample.

Despite having removed most of the background to these two exclusive decays, there is still a possibility that some contamination remains underneath the invariant mass distributions in Figures 6.7 and 6.8. The effect of this particular contribution is evaluated below.

Two different sets of runs used in the search of the  $\psi_c'(2^1S_0)$  are utilized here to determine the amount of background present in the data from the  $e^+e^-$  continuum or any remnant of the multi-pion decays: Runs 1283-1289 were taken at 3576 MeV, and runs 1180-1184 were taken at 3660 MeV. The quantum numbers of the  $\psi_c'$  do not permit it to decay directly to  $e^+e^-$ , and below the threshold for OZI-allowed decays only the  $J/\psi$  and the  $\psi'$  are allowed to do so.

Both sets of data went through the same analysis flow chart shown in Figure 6.1, with the centers-of-mass given as 3576 MeV and 3660 MeV respectively. Likewise the same cuts in Table 6.2 are applied; however the total energy cuts are a bit closer to the  $\psi'$  ( $6.5 \text{ GeV} < \text{ETOT} < 7.6 \text{ GeV}$ ) and the invariant mass cut is 2.7 GeV for both background runs. The clusters representing the background candidates were a) on-time and b) had the

invariant mass closest to the center-of-mass. The results are compared to both the  $J/\psi$  and the  $\psi'$ .

The invariant mass distributions of the background candidates are presented in Figure 6.15 for the set at 3576 MeV and in Figure 6.16 for the set at 3660 MeV. The rationale for cutting events with an invariant mass of less than 2.7 GeV can clearly be seen in both of these figures: The background without any cuts increases rapidly below this threshold. After applying all the analysis cuts, very few electron candidates remain, as one can see in Table 6.3, and the bottom of Figures 6.15 and 6.16.

In order to evaluate the number of background candidates that may contribute to the fit, the number of electrons actually falling within the fitting region needs to be found. Figure 6.17 shows the angular distribution of background candidates falling within the  $\psi'$  fitting region (which is larger in the center-of-mass). These distributions are created with respect to the CCAL polar angle.

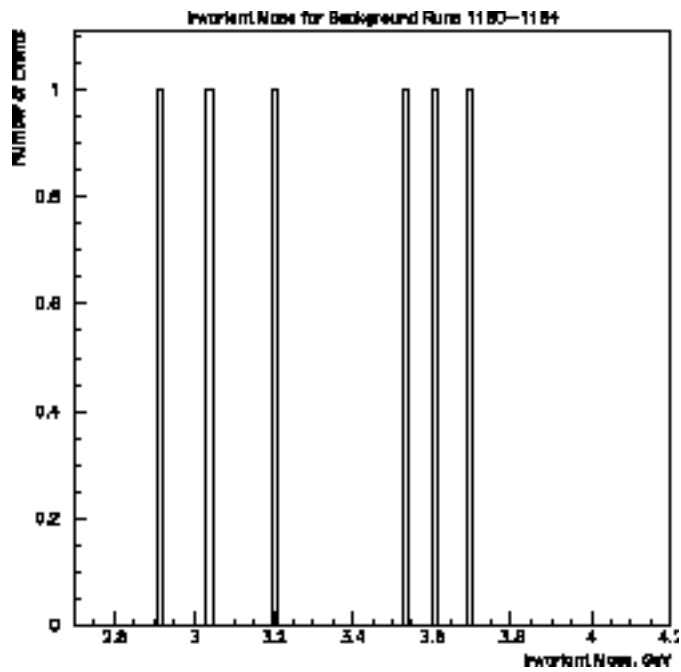
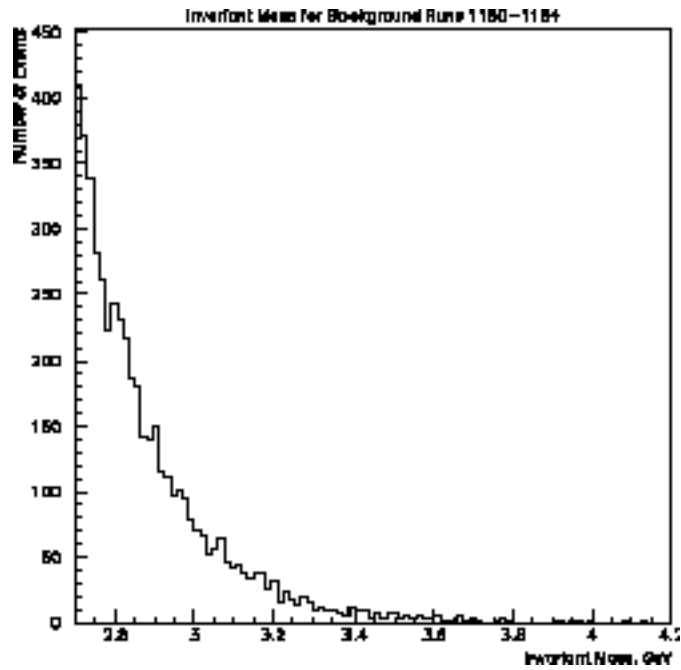


Figure 6.15: Invariant mass distributions for Runs 1180-1184 before any cuts are made (top) and after all cuts (bottom) are made.

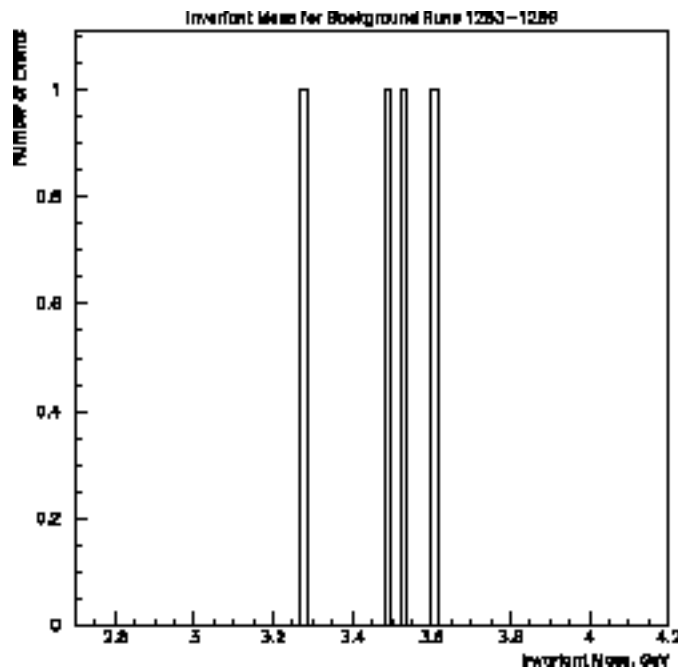
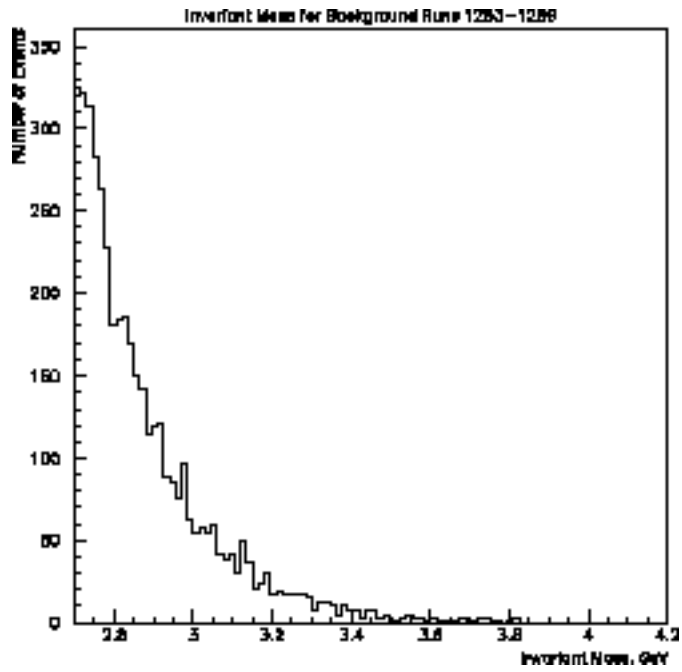


Figure 6.16: Invariant mass distributions for Runs 1283-1289 before any cuts (top) and after all cuts (bottom) are made.

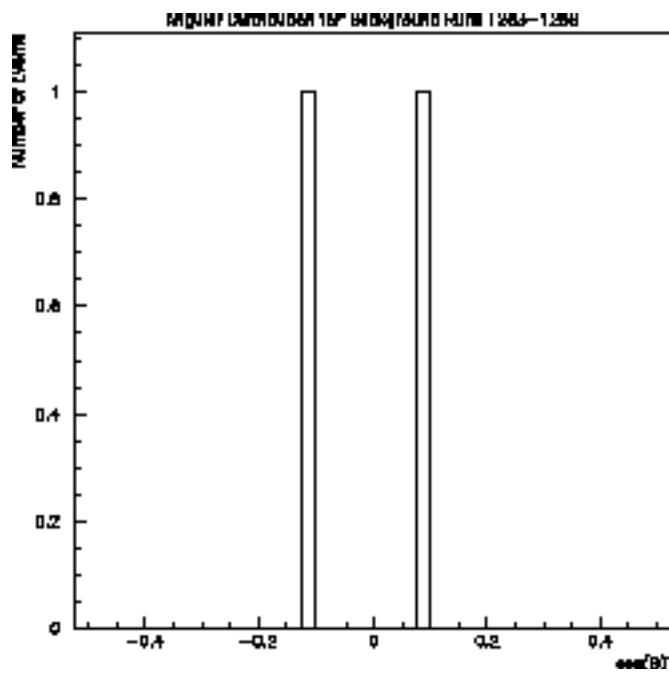
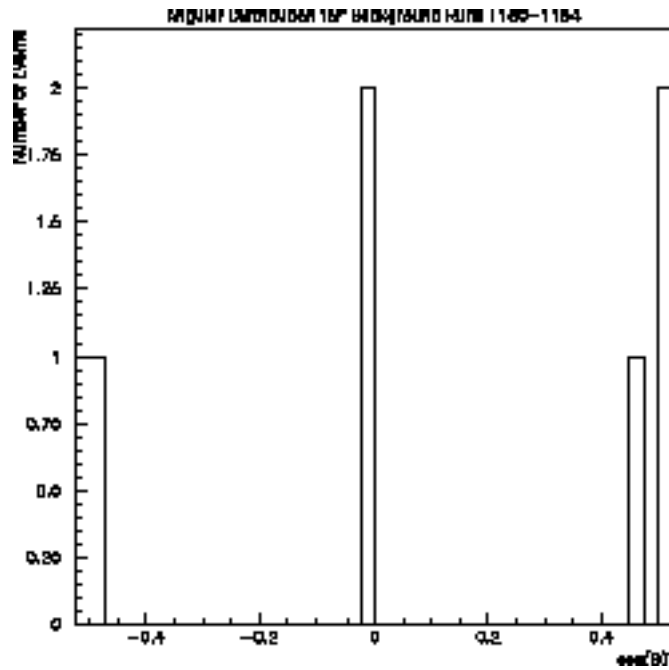


Figure 6.17: Angular Distributions for Background Candidates passing all cuts for Runs 1180-1184 (top) and Runs 1283-1289 (bottom).

Table 6.3 estimates the maximum amount of background contamination left underneath the invariant mass distributions assuming that the same percentage of background occurs for both resonances. An invariant mass cut of 3.4 GeV, the inefficiency of the fibers at large polar angles, and a smaller window in the center-of-mass will reduce these estimates. Taking the average of these two estimates predicts approximately 10 background events for the  $J/\psi$  ( $\sim 0.1\%$ ), and about 50 background events for the  $\psi'$  ( $\sim 1.85\%$ ).

Background Sample	Invariant Mass	Number of electrons in n-tuple	Background electron candidates	Background candidates at $J/\psi$ (19,540 in n-tuple)	Background candidates at $\psi'$ (108,422 in n-tuple)
Runs 1283-1289	3576 MeV	8612	2	4.5	25.2
Runs 1180-1184	3660 MeV	9784	7	14.0	77.6

Table 6.3 : Background estimate from off-resonance data.

## 6.5. Dependence of the Electron Trigger on the Polar Angle.

One further source of inefficiency which could effect the shape of the angular distribution may come from a polar angle dependence of the electron trigger. The electron trigger (see Table 6.4) is made up of the following trigger requests:  $CMLU(1)*PBG3 + CMLU(2)$ , where  $CMLU(1)$  is  $2e*(H2<6) + 1e*2h(H2=2)*COPL$ , and  $CMLU(2)$  is  $2e*(H2=2)*COPL*(Veto\ on\ FCH)$ , and

PBG3 is the 1 to 3 back-to-back super-cluster requirement.

The efficiency of the charged trigger (CMLU(1)) was examined during a special trigger run in April of 1997,<sup>94</sup> in which data were taken by replacing the 2-electron trigger (2e) with a 1-electron trigger (1e) in order to determine the efficiency of detecting an electron. However, the statistics were too limited to conclude that there was any polar angle dependence. Such a dependence might arise if there were a degradation of the hodoscopes along the z-axis (perhaps a result of radiation damage near the interaction point), but this was not visible. Above and beyond the azimuthal inefficiency brought about by cracks between the elements of the H1 hodoscope, the data taken during this trigger run was consistent with having no azimuthal dependence either. Since the efficiency of the electron trigger is considered to be flat in the center of mass frame, it should not affect the shape of the angular distribution. As a result, the data is not corrected for any polar angle dependence of the electron trigger.

CMLU(1)	Output 1 of the Charged Memory Lookup Unit
CMLU(2)	Output 2 of the Charged Memory Lookup Unit
PBG1	Super-clusters of “electrons” are directly opposite each other.
PBG3	The other “electron” is in one of the 3 opposing super-clusters
1e	At least one Cerenkov cell has a charged track through it.
2e	At least two Cerenkov cells have charged tracks through them.
H2=2	Only 2 of the 32 H2 elements are hit.
H2<6	Less than 6 of the 32 H2 elements are hit.
COPL	2 H2 elements are coplanar.
FCH	More than one forward hodoscope is hit.

Table 6.4 : Definitions for the E835 e<sup>+</sup>e<sup>-</sup> trigger.

## 7. Results

In Table 7.1 the final fit parameters to the angular distributions presented in Figures 7.1 and 7.2 are shown. For the process  $J/\psi \rightarrow e^+e^-$  in Figure 7.1, the bin size is 0.025 and the range  $-0.45 < \cos(\theta) < 0.45$  is fitted. For the process  $\psi' \rightarrow e^+e^-$  displayed in Figure 7.2, the bin size of the abscissa is 0.025 and the range  $-0.525 < \cos(\theta) < 0.525$  is fitted.

Both angular distributions are fit to a function  $A + B \cos^2(\theta)$ , yielding the final fit parameters presented in Table 7.1. Significantly, both distributions have a chi-square of 1.0 per degree of freedom.

From this function, the angular distribution parameter is defined as  $\alpha = B/A$ . With the help of the parameters quoted in Table 7.1, one can derive the statistical error in the angular distribution parameter,  $\delta\alpha$ . A systematic error is calculated based upon the efficiency of the scintillating fibers (see Figure 6.3), since no correction is made in this regard. For the  $J/\psi$ , the efficiency is always larger than 92% throughout the range being fit. Hence the systematic error for this analysis is estimated as 8% of the angular distribution parameter, 0.05. Likewise for the  $\psi'$ , the efficiency is always greater than 96%. The

corresponding systematic error is estimated as 4% of the angular distribution parameter, 0.03. The angular distribution parameters and their associated errors for this analysis are summarized in Table 7.2.

Resonance	A	$\sigma_A$	B	$\sigma_B$	$\chi^2$ per d.o.f.
J/ $\sigma$ (3097)	282.03	4.2318	177.36	47.828	1.005
$\sigma$ (3686)	59.42	1.7991	38.903	15.040	1.008

Table 7.1: Final Fit Parameters.

Resonance	$\sigma = B/A$	$\sigma_{stat}$ (statistical)	$\sigma_{sys}$ (systematic)
J/ $\sigma$ (3097)	0.629	0.177	0.05
$\sigma$ (3686)	0.655	0.268	0.03

Table 7.2: Angular Distribution Parameters.

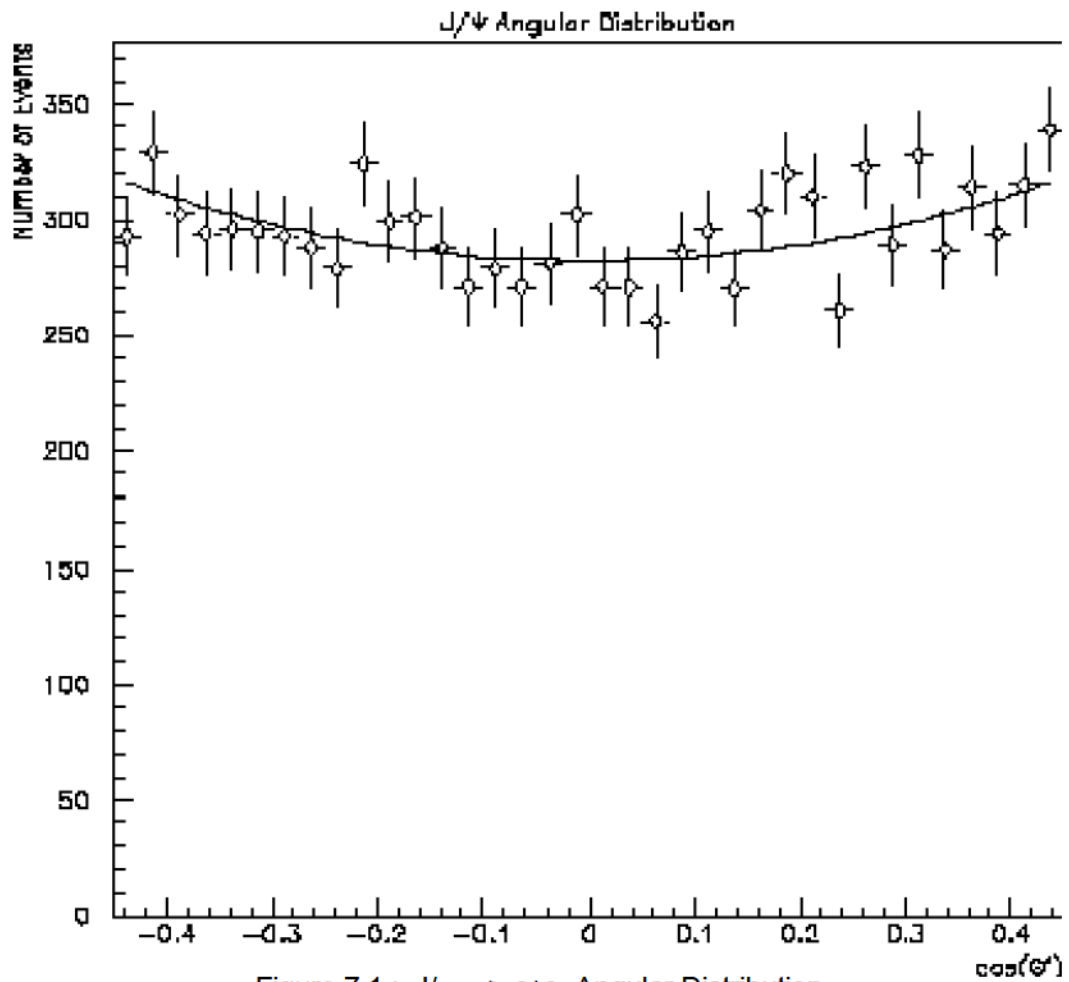


Figure 7.1 :  $J/\psi \rightarrow e^+e^-$  Angular Distribution

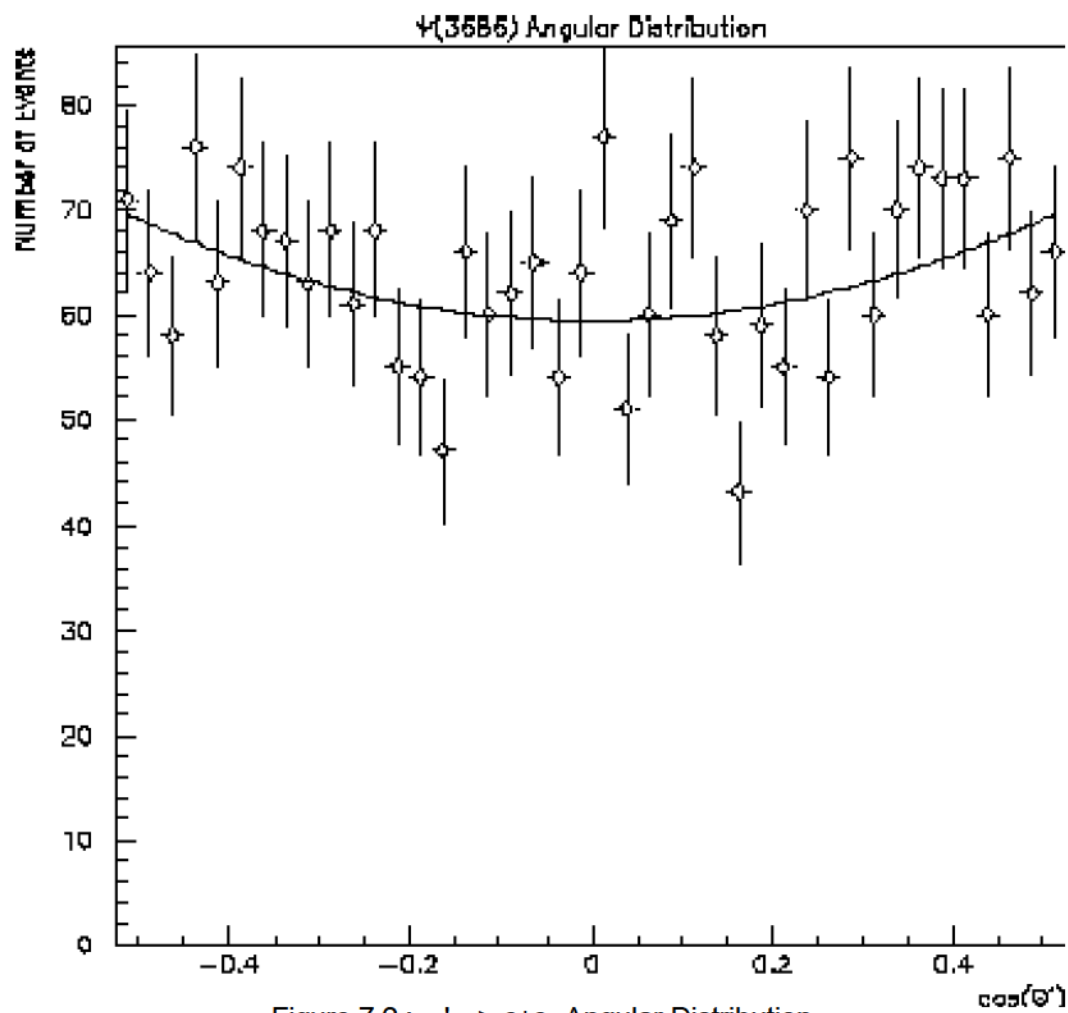


Figure 7.2 :  $e^+e^-$  Angular Distribution

Using these results for the angular distribution parameter, the value for the ratio of the Sachs form factors<sup>76</sup>  $G_E$  and  $G_M$  dictated by Lorentz invariance at both resonances can be deduced from equation (5.20):

$$\left| \frac{G_E}{G_M} \right|^2 = \left( \frac{E_{CM}^2}{4m_p^2} \right) \left( \frac{1 \cdot \dots \cdot}{1 \cdot \dots \cdot} \right). \quad (7.1)$$

The ratio of these strong form factors is zero when  $\dots$  is 1. Setting this ratio to one yields  $\dots$  derived by Claudson, Glashow, and Wise,<sup>82</sup> where the spin-flip amplitude was set to zero.

Furthermore, from equation (5.16), one can determine the probability that the charmonium atom is produced in a helicity one or helicity zero configuration in the helicity formalism:

$$\frac{2 C_0^2}{C_1^2} = \frac{1 \cdot \dots}{1 + \dots}. \quad (7.2)$$

Here  $C_1^2$  is the probability for the charmonium atom to be produced in a

helicity one configuration, and  $2C_0^2$  is the probability for helicity zero production.

We can then solve for  $C_1^2$  from the normalization condition  $C_1^2 + 2C_0^2 = 1$ .

Resonance	$\alpha$	$ G_E/G_M ^2$	$C_1^2$
$J/\psi$ (3097)	$0.63 \pm 0.18 \pm 0.05$	0.619	0.815
$\psi(3686)$	$0.66 \pm 0.27 \pm 0.03$	0.791	0.830

Table 7.3 : Sachs form factor ratio and helicity one production probability derived from the angular distribution parameter.

As seen in table 7.3, the charmonium  $1^{--}$  resonances are predominately created via the helicity one channel. As the energy scale increases, or more significantly as the ratio of the proton mass to the charmonium mass decreases, helicity one production should increase as well. We note that in  $e^+e^-$  annihilation the ratio of the electron mass to the charmonium mass is zero, and the angular distribution parameter for charmonium production by  $e^+e^-$  annihilation is 1. Although the angular distribution parameter for the  $\psi'$  is statistically consistent with a value close to one and larger than the same for the  $J/\psi$ , it also appears likely that both resonances share a similar angular distribution parameter. If it is a function of energy, it does not seem to vary much in the charmonium family given the current data.

Historically, only the  $J/\psi$  angular distribution parameter has been measured by experiments. In Table 7.4 a comparison is made with the other experimental values. The thesis value is consistent with the world average for the  $J/\psi$ . Attempts to generate the  $\psi'$  angular distribution parameter have been hindered because the exclusive cross section falls off as  $Q^{-2}$ .

Experiment	$\alpha$ at $J/\psi$
Mark I <sup>95</sup>	$1.45 \pm 0.56$
DASP <sup>96</sup>	$1.70 \pm 1.70$
Mark II <sup>97</sup>	$0.61 \pm 0.23$
DM2 <sup>98</sup>	$0.62 \pm 0.11$
Mark III <sup>99</sup>	$0.58 \pm 0.14$
Fermilab E760 <sup>22</sup>	$0.69 \pm 0.26$
World Average	$0.63 \pm .08$
Fermilab E835(this thesis)	$0.63 \pm 0.18 \pm 0.05$

Table 7.4 : Previous experimental results for the angular distribution parameter  $\alpha$ .

## 8. Conclusions

The angular distribution parameter  $\alpha$  measures how well a perturbative treatment of charmonium and the constituent antiproton and proton works. If charmonium could be completely treated perturbatively and the energy scale is high enough, then this parameter should be one. We have determined the angular distribution parameter to be in accordance with the world average for the  $J/\psi$ , and both the  $J/\psi$  and  $\psi'$  are produced via the helicity one channel over 80% of the time.

There are a few reasons why the angular distribution parameter is not one in the charmonium system, especially for the  $J/\psi$ . Principally this is due to the energy at which charmonium is produced. The production process indeed probes distances in the confinement region of the interquark potential between the valence quarks of the proton and between the charm and anti-charm quarks. When the interquark distance is smaller, a pure perturbative treatment is more appropriate.

The theoretical derivation of the angular distribution parameter is far from complete. Higher-order Feynman diagrams can still be included, and it is unclear whether one may model the distribution amplitudes in the same way at

charmonium energies than at top quark energies. One may also argue about the charmonium potential used in the derivation and the appearance of multi-quark Fock states in the proton. Nevertheless, recent theoretical predictions are quite consistent with experimental results.

Figure 8.1 compares the angular distribution parameter derived in this thesis respectively with previous theoretical expectations for the  $J/\psi$  shown in Chapter 5. The value of  $0.63 \pm 0.18 \pm 0.05$  is consistent with most of the theoretical predictions to within  $1\sigma$ , although the predictions of Brodsky-Lepage and Gari-Stefanis lie outside the  $1\sigma$  window.

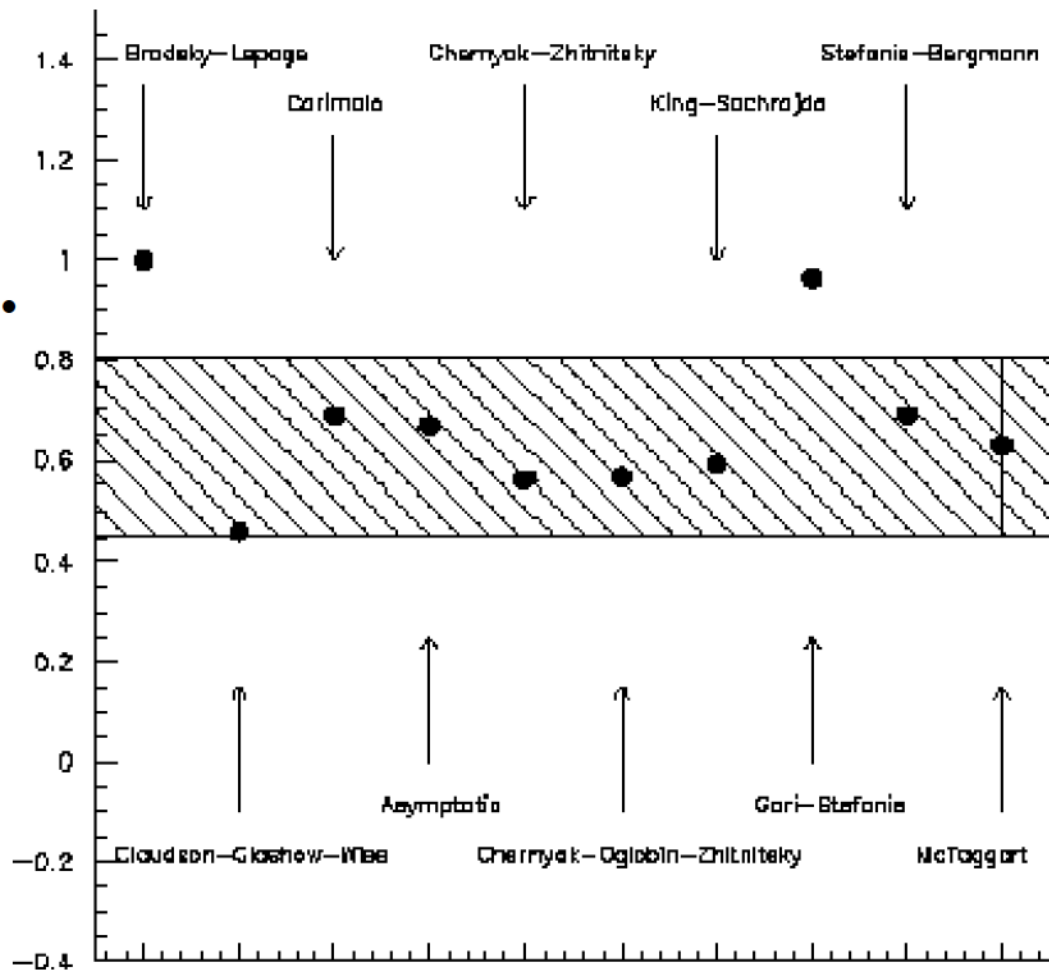


Figure 8.1: Comparison of thesis value with the theoretical predictions for the angular distribution parameter  $\alpha^*$  at the  $J/\psi$ .

Figure 8.2 likewise compares the thesis value for the  $\alpha^*$  with the various theoretical models. In this case, the thesis value again agrees with all the predictions for the  $\alpha^*$  to within  $1\sigma$ . Again, the values of Brodsky-Lepage, and Gari-Stefanis lie outside the  $1\sigma$  window.

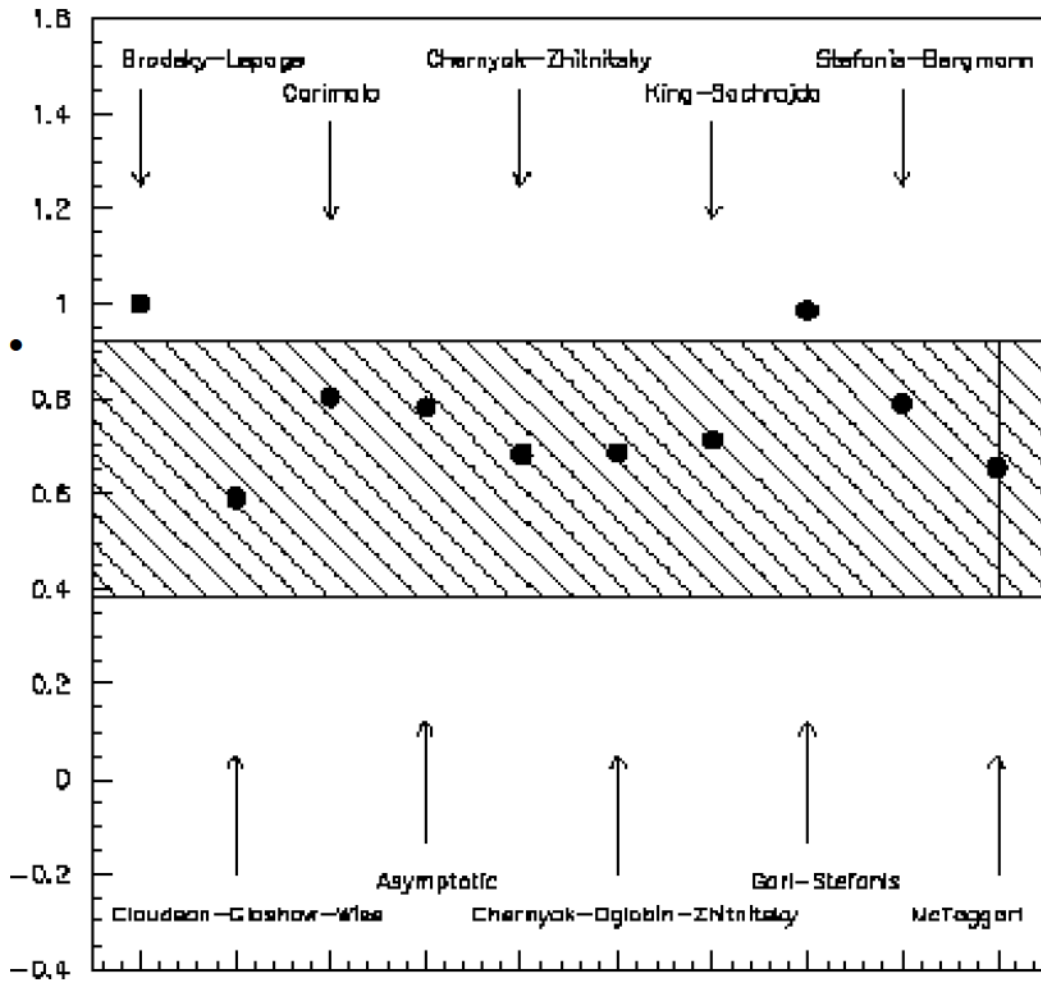


Figure 8.2 : Comparison of thesis value with the theoretical predictions for the angular distribution parameter  $\alpha$  at the  $J/\psi$ .

In Figure 8.3 one may contrast the thesis value for the  $J/\psi$  with previous experiments (see Table 7.3). The thesis value of  $0.63 \pm 0.18 \pm 0.05$  agrees with both the world average of  $0.63 \pm 0.08$  and lies within the errors of all the previous experiments except Mark I. Moreover, the proton-antiproton annihilation method (from e760 and e835) is consistent with the electron-

positron method of charmonium production at the  $J/\psi$ , where  $\alpha$  is derived from the decay of charmonium into  $p\bar{p}$ .

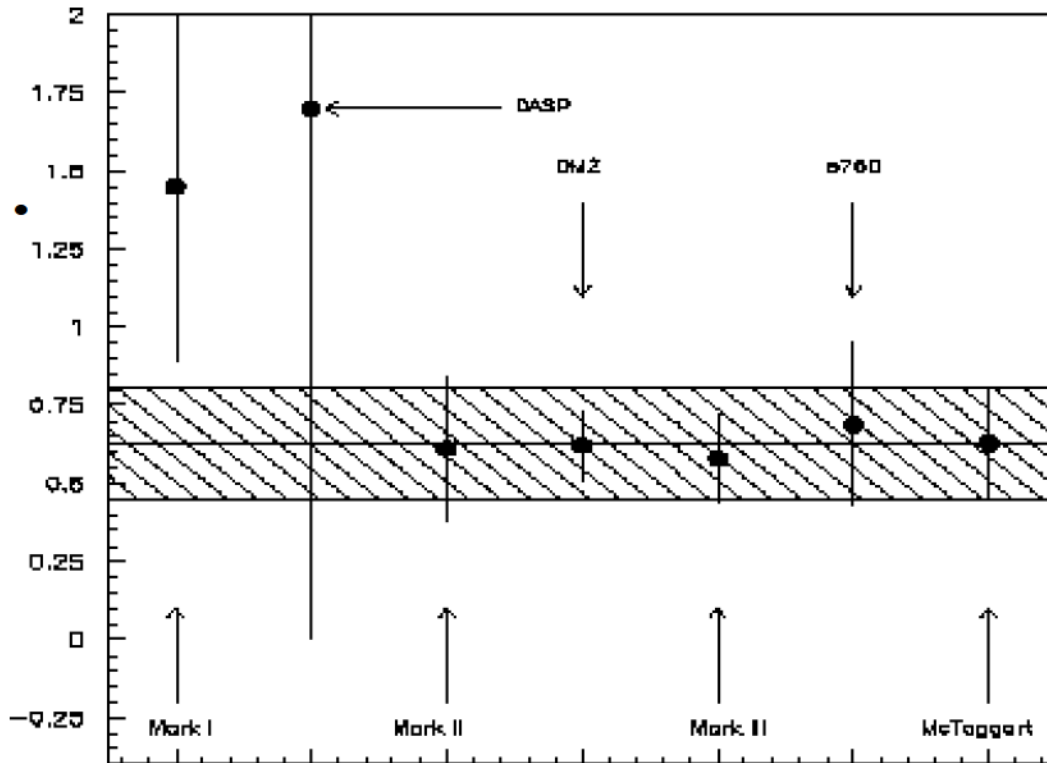


Figure 8.3 : Comparison of thesis value with previous experimental data for the angular distribution parameter  $\alpha$  at the  $J/\psi$ .

In conclusion, the experimental values presented in this thesis for the angular distribution parameter are consistent within errors with most of the theoretical models and with the current world experimental average. However, the theoretical extremes of either a pure perturbative system or of a system where spin-flip amplitudes are negligible are mildly inconsistent with the results at both the  $J/\psi$  and the  $\psi'$ . Hence spin dynamics and the confinement term in

the QCD potential have an effect.

Increased statistics and a value for the width to  $p\bar{p}$  would help to favor one particular theory, since the thesis values match several predictions equally well. However it appears that the heterotic treatment of Stefanis-Bergmann<sup>85</sup> agree better with both the thesis values for the angular distribution parameter and the quoted widths to  $p\bar{p}$  (see Tables 5.1 and 5.2), which are not determined from the thesis sample. In this instance, non-perturbative effects in the formation of the proton (or dissolution thereof) represented by the quark distribution amplitudes become important.

The hypothesis that the angular distribution parameter, which links  $p\bar{p}$  annihilation to charmonium production, increases as the formation energy increases (which is predicted by QCD) cannot be excluded by the data presented in this thesis. However, this behavior must be resolved by more data at the  $\psi'$ , since the thesis values of the angular distribution are also consistent with the angular distribution parameter remaining constant, or nearly constant, over the course of the charmonium system.

The final values of the angular distribution parameter derived in this thesis for the exclusive decays of  $J/\psi$  and  $\psi'$  into  $e^+e^-$  from proton-antiproton annihilation are:

$$\begin{aligned} \langle \cos^2\theta \rangle_{J/\psi} &= 0.63 \pm .18 \text{ (statistical)} \pm .05 \text{ (systematic)} \\ \langle \cos^2\theta \rangle_{\psi'} &= 0.66 \pm .27 \text{ (statistical)} \pm .03 \text{ (systematic)} \end{aligned}$$

## Bibliography

1. Gary J. Feldman. *Weak Interactions at High Energy and the Production of New Particles:  $\psi$ -Spectroscopy*. Proceedings of Summer Institute on Particle Physics, ed. by Martha C. Zipf, August 2-13, 1976.
2. F. Halzen and A. D. Martin. *Quarks and Leptons: An Introductory Course in Modern Particle Physics*. John Wiley & Sons, Inc., 1984.
3. S. L. Glashow, J. Iliopoulos, L. Maiani, *Weak Interactions with lepton-hadron symmetry*, Phys Rev D, 2 (7): 1285-1292, 1970.
4. T. Appelquist and D. Politzer, *Heavy Quarks and  $e^+e^-$  Annihilation*, Phys Rev Letters, 34 (1): 43-45 (1975).
5. J. J. Aubert et al, *Experimental Observation of a Heavy Particle J*, Phys Rev Letters, 33(23):1404-1406, 1974.
6. J.E. Augustin et al, *Discovery of a Narrow Resonance in  $e^+e^-$  Annihilation*, Phys Rev Letters, 33 (23): 1406-1408 ,1974.
7. G. S. Abrams et al, *The Discovery of a Second Narrow Resonance in  $e^+e^-$  Annihilation*, Phys. Rev. Lett. 33: 1453-1455, 1974.
8. J. L. Marques. *Study of the  $\psi_1$  and  $\psi_2$  States produced in  $\bar{p}p$  Annihilations in Fermilab Experiment 760*. Ph.D. Dissertation, University of California at Irvine (1992).
9. Novikov et al, *Charmonium and Gluons*, Phys Reports 41C (1):1-133, 1978.
10. A. Boyarski et al, *Quantum Numbers and Decay Widths of the  $\psi$  (3095)*, Phys Rev Letters 34 (23):1357 (1975).
11. V. Luth et al, *Quantum Numbers and Decay Widths of the  $\psi$  (3684)*, Phys Rev Letters 35 (17):1124 (1975).

12. R. H. Schindler et al, *Measurement of the parameters of the  $\psi(3770)$  resonance*, Phys Rev D 21, 1980.
13. [http://www-e835.fnal.gov/images/charm\\_spectrum.ps](http://www-e835.fnal.gov/images/charm_spectrum.ps)
14. W. Kwong and J. L. Rosner, *Heavy-Quark Systems*, Ann. Rev. Nucl. Part. Sci. 37: 325-382 (1987).
15. W. Lucha, F. Schoberl, and D. Gromes, *Bound States of Quarks*, Physics Reports 200, 127-240 (1991).
16. E. Eichten et al, *Charmonium: Comparison with experiment.*, Phys Rev D 21 (1), 203-226 (1980).
17. Y. Zhu. *The Decay Properties of the  $\psi(3770)$* . Ph. D. Thesis, California Institute of Technology, 1989.
18. Ding, Qin and Chao, *Electric dipole transitions of  $\psi(3770)$  and S-D mixing between  $\psi(3686)$  and  $\psi(3770)$* , Phys Rev D 44 (11), 3562-3566 (1990).
19. R. Cahn. *Charmonium Spectroscopy: 1987*. Talk given at Mark III Pow-Wow, May 9, 1987, Hillsborough, CA.
20. R.W. Robinett and L. Weinkauff, *Exclusive QCD predictions for proton-antiproton decay rates of  $^3D_1$  charmonium states*, Phys Letters B 271 (1991) 231-236.
21. Kuang and Yan, *Hadronic transitions of D-wave quarkonium and  $\psi(3770) \Rightarrow J/\psi + \psi'$* , Phys Rev D 41 (1), 155-160 (1990).
22. T.A. Armstrong et al, *Measurement of the  $J/\psi$  and  $\psi'$  resonance parameters in  $\bar{p}p$  annihilation*, Phys Rev D 47 (3): 772-783 (1993).
23. M. Oreglia et al, Phys Rev D25: 2259, 1982.
24. Baglin et al, Phys Letters B172:455, 1986.
25. C. Baglin et al,  *$J/\psi$  Resonance Formation and Mass Measurement in Antiproton-Proton Annihilations*, CERN-EP/87-30, 16 February 1987.

26. T. A. Armstrong et al, *Observation of the  $1P_1$  State of Charmonium.*, Phys Rev Letters 69, 1992.
27. T. A. Armstrong et al, *Study of the  $\psi_c(1^1S_0)$  state of charmonium formed in  $\bar{p}p$  annihilations and a search for the  $\psi_c'(2^1S_0)$* , Phys Rev D 52, 1995.
28. <http://www-e835.fnal.gov/images/pbarsource.ps>.
29. K.E. Gollwitzer. *The Charmonium  $1P_1$  State  $h_c$  Produced in Antiproton-Proton Collisions*. Ph.D. Thesis. University of California at Irvine, 1992.
30. *Design Report: Tevatron I Project*. Fermilab report, 1984 (unpublished).
31. C. Ginsburg. *Spectroscopy of  $J/\psi$  and  $\psi'$  Charmonium Resonances*. Ph. D. thesis, Northwestern University, 1995.
32. Particle Data Group, K. Hikasa et al., Phys. Rev. D 45, S1 (1992).
33. D.H. Allspach et al, *The variable density gas jet internal target for Experiment 835 at Fermilab*, Nuclear Instruments and Methods in Physics Research A410 (1998), 195-205.
34. <http://www-e835.fnal.gov/images/det.ps>.
35. S. Trokenheim et al, *A  $\bar{p}p$  luminosity monitor for Fermilab experiment E760*, Nuclear Instruments and Methods in Physics Research A355 (1995), 308-319.
36. <http://www-e835.fnal.gov/images/e835inner811.ps>
37. C. Biino et al, *Charge division in a small proportional chamber constructed with aluminized mylar tubes*, Nuclear Instruments and Methods in Physics Research A271 (1988) 417-422.
38. A. Buzzo et al, *A Silicon Pad Detector for E-835 experiment at Fermilab*, Nuclear Instruments and Methods in Physics Research A391 (1997), 443-451.
39. R. Mussa et al, *Development of a cylindrical scintillating fiber tracker for experiment E835 at FNAL*, Nuclear Instruments and Methods in Physics Research A 360 (1995) 13-16.
40. <http://www-e835.fnal.gov/images/cerenkov.ps>.

41. C. Biino et al, *A large acceptance threshold Cherenkov counter for Experiment 760 at Fermilab.*, Nuclear Instruments and Methods in Physics Research A317 (1992) 135-142.
42. <http://www-e835.fnal.gov/images/ccal-side-view.ps>.
43. <http://www-e835.fnal.gov/images/ccal-cross-section.ps>.
44. L. Bartozek et al, *The e760 lead-glass calorimeter*, Nuclear Instruments and Methods A301, 47-60 (1991).
45. Sheng Jin, Northwestern University. Private Communication. September 6, 1997.
46. Armstrong et al, *The Fermilab E760 forward electromagnetic calorimeter*, Nuclear Instruments and Methods A295: 73-80 (1990).
47. R. Ray et al, *A trigger for the E760 calorimeter*, Nuclear Instruments and Methods A307, 254-264 (1991).
48. G. Oleynik et al. *DART Data Acquisition System Architecture*. Fermilab memo, 1994.
49. K. Gollwitzer. *E835 Online and Offline UNIX Computing*. E835 internal memo. November 22, 1994.
50. <http://www.lecroy.com/lrs/dsheets/3377.htm>
51. <http://www.lecroy.com/lrs/dsheets/4300b.htm>
52. <http://www.lecroy.com/lrs/dsheets/2731a.htm>
53. <http://fnphyx-www.fnal.gov/elec/dyc3/dyc3nov.html>
54. [http://www-dart.fnal.gov:8000/usr/products/cluster\\_disk/product\\_info/html/ddd.html](http://www-dart.fnal.gov:8000/usr/products/cluster_disk/product_info/html/ddd.html)
55. G. Zioulas. *E835 Data Acquisition* . e835 internal memo. November 27, 1996.
56. <http://www-e835.fnal.gov/~giorgos/daq/E835DAQorg.ps>.
57. K. Gollwitzer and G. Zioulas. *E835 Event Header and Unpacking*. E835 internal memo. February 29, 1996.

58. R. McTaggart. *The PRUDE Interface, Version 2*. e835 internal memo. September 29, 1996.
59. DART presentation to BaBar. February 13, 1996.
60. <http://www-e835.fnal.gov/~giorgos/daq/e835daqproc.ps>
61. G. Zioulas. Private Communication. September 8, 1997.
62. R. McTaggart and J. Streets. *Terminal Communication under UNIX*. e835 internal memo. August 16, 1995.
63. R. McTaggart and J. Streets. *Terminal Communication under UNIX: The e835 High Voltage Control Program*. e835 internal memo. December 8, 1995.
64. R. McTaggart. *The e835 High Voltage Monitor*. e835 internal memo. February 12, 1996.
65. R. McTaggart. *The e835 Pedestal Program*. e835 internal memo. September 11, 1996.
66. M. Thompson. *Database Structure for E835*. e835 internal memo. August 16, 1996.
67. M. Jacob and G. C. Wick, *On the General Theory of Collisions for Particles with Spin*, *Annals of Physics* 7:404-428 (1959).
68. A.D. Martin and T.D. Spearman. *Elementary Particle Theory*. North-Holland Publishing Co., Amsterdam, 1970.
69. L. Ballentine. *Quantum Mechanics*. Prentice Hall, Inc. 1990.
70. A.J. Smith. *A Study of Select Decays of  $J/\psi$  and  $\psi'$  States Produced in Antiproton-proton Annihilations*. Ph. D. Dissertation, University of California at Irvine (1996).
71. G. S. Abrams et al, *Quantum Numbers and Decay Widths of the  $\psi$  (3095)*, *Phys Rev D* 34 (21) 1357-1360, 1975.
72. G. S. Abrams et al, *Quantum Numbers and Decay Widths of the  $\psi$  (3684)*, *Phys Rev D* 35 (17), 1124-1126 (1975).

73. T. A. Armstrong et al, *Proton Electromagnetic Form Factors in the Timelike Region from 8.9 to 13.0 GeV<sup>2</sup>*, Phys Rev Lett 70 (9): 1212-1215, 1993.
74. S. Brodsky and D. Robertson, *Light-Cone Quantization and QCD Phenomenology*, hep-ph/9511374, 20 Nov. 1995.
75. P. Kroll, *Exclusive charmonium decays*, Hep-ph/9709393, 18 Sep 1997.
76. Zichichi, Berman, Cabibbo, and Gatto, *Proton-Antiproton Annihilation into Electrons, Muons, and Vector Bosons*, Nuovo Cimento (24) 170, 1962.
77. G. Lepage and S. Brodsky, *Exclusive processes in perturbative quantum chromodynamics*, Phys Rev D 22, 2157, 1980.
78. F. Murgia and M. Melis, *Mass Corrections in  $J/\psi \rightarrow BB$  decay and the role of distribution amplitudes.*, Phys Rev D 51 (7), 3487-3500 (1995).
79. Jonas Schultz. Private Communication. September 22, 1997.
80. Francesco Murgia. Private Communication. October 1, 1997.
81. S. Brodsky and G. Lepage, *Helicity selection rules and test of gluon spin in exclusive quantum-chromodynamic processes*, Phys Rev D 24 (11), 2848-2855 (1981).
82. M. Claudson, S. Glashow, and M. Wise, *Isospin violation in  $J/\psi \rightarrow baryon + antibaryon$* , Phys Rev D 25 (5), 1345-1347 (1982).
83. C. Carimalo, *Quark Mass Effects in  $J/\psi \rightarrow \bar{B} B$  Decays*, Int J Mod Phys A2:249, 1987.
84. L. Köepke and N. Wermes,  *$J/\psi$  Decays*, CERN-EP/88-93, August 5, 1988.
85. N. G. Stefanis and M. Bergmann, Phys Rev D 47, 3685 (1993).
86. Francesco Murgia. Private Communication. October 3, 1997.
87. Francesco Murgia. Private communication. October 17, 1997.
88. V. L. Chernyak and I. R. Zhitnitsky, Physics Reports 112, 174 (1984).
89. V.L. Chernyak, A.A. Oglobin, and I.R. Zhitnitsky, Z. Phys. C 42, 569 (1989);

- 42, 583 (1989).
90. I. D. King, and C. T. Sachrajda, Nucl. Phys. B279, 785 (1987).
91. M. Gari and N. G. Stefanis, Phys. Lett. B 175, 462 (1986).
92. M. Ambrogiani et al. *Results from the E835 Cylindrical Scintillating-Fiber Tracker*. SCIFI97: Workshop on Scintillating Fiber Detectors. AIP Conference Proceedings Volume #450. November 1998.
93. Keith Gollwitzer. *The CCAL Shower Monte Carlo*. E760 Memo 312. March 3, 1994.
94. W. Baldini and F. Marchetto. *Charged trigger efficiency for inclusive  $J/\psi$* . E835 Memo. April 25, 1997.
95. I. Peruzzi et al, Phys Rev D 29, 804 (1984).
96. R. Brandelik et al, Z. Phys. C1, 233 (1979).
97. M. W. Eaton et al, Phys Rev. D 29, 804 (1984).
98. D. Pallin et al, Nucl. Phys. B292, 653 (1987).
99. J.S. Brown, PhD Thesis, University of Washington UMI 84-19117-mc(unpublished).

## Appendix A: Efficiencies of Cuts, $J/\psi$ .

1.	2 on-time clusters.
2.	Invariant mass greater than 2.7 GeV .
3.	Acoplanarity between -25 milliradians and +25 milliradians.
4.	Akinematics between -25 milliradians and +25 milliradians.
5.	4.71 GeV < ETOT < 5.31 GeV.

Cuts Applied	908-909	3078-3079
1	0.78235	0.78184
2	0.72066	0.67683
3	0.80596	0.76599
4	0.79749	0.75594
5	0.79563	0.74614
Electrons in sample	8199	2419

Table A.1: Efficiency of one cut on the  $J/\psi$  n-tuple.

Cuts Applied	908-909	3078-3079
1,2	0.78235	0.78184
1,3	0.85486	0.86270
1,4	0.84430	0.85176
1,5	0.85176	0.83847
2,3	0.80596	0.76599
2,4	0.79749	0.75594
2,5	0.79563	0.74614
3,4	0.87559	0.83702
3,5	0.88256	0.83673
4,5	0.87140	0.82223
Electrons in Sample	8199	2419

Table A.2: Efficiency of two cuts on the  $J/\psi$  n-tuple.

Cuts Applied	908-909	3078-3079
1,2,3	0.85486	0.86270
1,2,4	0.84430	0.85176
1,2,5	0.85176	0.83847
1,3,4	0.91804	0.93362
1,3,5	0.93192	0.92540
1,4,5	0.91783	0.91317
2,3,4	0.87559	0.83702
2,3,5	0.88256	0.83673
2,4,5	0.87140	0.82223
3,4,5	0.95515	0.90803
Electrons in sample	8199	2419

Table A.3: Efficiency of three cuts on the  $J/\psi$  n-tuple.

Cuts Applied	908-909	3078-3079
1,2,3,4	0.91804	0.93362
1,2,3,5	0.93192	0.92540
1,2,4,5	0.91783	0.91317
1,3,4,5	1.00000	1.00000
2,3,4,5	0.95515	0.90803
Electrons in sample	8199	2419

Table A.4: Efficiency of four cuts on the  $J/\psi$  n-tuple.

## Appendix B: Efficiencies of Cuts, • ’

1.	2 on-time clusters.
2.	Invariant mass greater than 3.4 GeV.
3.	Acoplanarity between -25 milliradians and +25 milliradians.
4.	Akinematics between -25 milliradians and +25 milliradians.
5.	$6.72 \text{ GeV} < \text{ETOT} < 7.62 \text{ GeV}$ .

Cuts Applied	877-882	1006-1018	1276-1281	2003-2018	2218-2253	3210-3233
1	0.40430	0.49751	0.55157	0.62233	0.56108	0.54083
2	0.52141	0.43764	0.57401	0.68318	0.57791	0.58515
3	0.28240	0.26882	0.29246	0.34656	0.26689	0.23388
4	0.25972	0.26110	0.32050	0.38220	0.29281	0.27154
5	0.39579	0.34843	0.45075	0.56771	0.45533	0.42951
Electrons in sample	207	200	508	524	790	457

Table B.1: Efficiency of one cut on the • ’ n-tuple.

Cuts Applied	877-882	1006-1018	1276-1281	2003-2018	2218-2253	3210-3233
1,2	0.73404	0.72464	0.84950	0.88964	0.83953	0.85261
1,3	0.70408	0.70175	0.78760	0.79394	0.77224	0.76040
1,4	0.66559	0.68259	0.79874	0.87333	0.78529	0.79756
1,5	0.76667	0.82305	0.84950	0.89116	0.84764	0.86226
2,3	0.72887	0.63091	0.72884	0.80000	0.71107	0.71184
2,4	0.67647	0.61162	0.71248	0.80122	0.70662	0.72196
2,5	0.63692	0.56180	0.66146	0.73492	0.63864	0.65850
3,4	0.57660	0.55556	0.62331	0.72077	0.59939	0.57629
3,5	0.78113	0.68027	0.72884	0.79756	0.69177	0.68209
4,5	0.76384	0.71685	0.75595	0.82390	0.72477	0.73237
Electrons in sample	207	200	508	524	790	457

Table B.2: Efficiency of two cuts on the  $n$ -tuple.

Cuts Applied	877-882	1006-1018	1276-1281	2003-2018	2218-2253	3210-3233
1,2,3	0.84490	0.80000	0.90553	0.92091	0.90286	0.90316
1,2,4	0.77528	0.76046	0.88656	0.93571	0.90183	0.91400
1,2,5	0.83806	0.87719	0.90533	0.91769	0.87583	0.89432
1,3,4	0.81818	0.80321	0.90231	0.93238	0.88367	0.89084
1,3,5	0.94521	0.93897	0.95131	0.93739	0.92832	0.93648
1,4,5	0.86250	0.90909	0.93554	0.96324	0.92832	0.95010
2,3,4	0.79615	0.70671	0.78760	0.87043	0.78607	0.78929
2,3,5	0.84836	0.77220	0.79624	0.83439	0.75598	0.76167
2,4,5	0.78707	0.73529	0.77439	0.83840	0.74248	0.76040
3,4,5	0.92411	0.83682	0.84106	0.90034	0.81026	0.81462
Electrons in sample	207	200	508	524	790	457

Table B.3: Efficiency of three cuts on the  $\bullet$  ' n-tuple.

Cuts Applied	877-882	1006-1018	1276-1281	2003-2018	2218-2253	3210-3233
1,2,3,4	0.87712	0.83682	0.94074	0.96679	0.95990	0.96211
1,2,3,5	0.95833	0.95694	0.96395	0.95100	0.94048	0.94421
1,2,4,5	0.87712	0.91743	0.94249	0.96679	0.93713	0.95010
1,3,4,5	1.00000	0.99010	0.99219	0.99620	0.98897	1.00000
2,3,4,5	0.92411	0.85106	0.84950	0.90345	0.82206	0.82491
Electrons in sample	207	200	508	524	790	457

Table B.4: Efficiency of four cuts on the  $\bullet$  ' n-tuple.

## Vita, Robert J. McTaggart II

May 1999 Ph.D. in Physics, Pennsylvania State University.  
1998-1999 Lecturer of Physics, West Virginia University.  
Spring 1998 Visiting Assistant Professor, Shippensburg University.  
1997 Teaching Assistant, Pennsylvania State University.  
1994-1996 Research Assistant, Pennsylvania State University.  
1991-1993 Teaching Assistant, Pennsylvania State University.  
May 1991 B.S. in Physics with honors, West Virginia University.  
May 1991 B.A. in Mathematics, West Virginia University.  
Graduate of West Virginia University Honors Program.  
1989 Barry Goldwater Scholar.  
WVU Presidential Scholar.

On experiment E835 at Fermilab I was responsible for the maintenance and operation of the LeCroy 1440 High Voltage System. I modified the program that operated the High Voltage System in E760 for the needs of E835, and in addition wrote the program that monitored said system during data taking. I also wrote the program that took pedestals for E835, and developed a GUI interface to change variables in the experiment's database accessed by the on-line filter program. I assisted in the cabling of the data acquisition of the experiment, and the installation, debugging, and calibration with cosmic rays of the forward calorimeter of E835.

Prior to the running of E835, I participated in the light quark analysis of E760 data, specifically the  $\pi^+\pi^-\pi^0$  channel. This involved a likelihood method analysis of Dalitz plots. I was also involved in the development of a preliminary 3-D event display for Experiment 835. While at Penn State in 1993 I assisted in the wiring of straw chambers used in Experiment 864 at Brookhaven National Laboratory. At West Virginia University I studied the behavior of the bipolar magnet in the context of strange attractors and the bifurcation route to chaos.